JOURNAL OF PETROLOGY | VOLUME 47 | NUMBER 7 | PAGES 1261–1315 | 2006 | doi:10.1093/petrology/egl008

Genesis of Ultramafic Lamprophyres and Carbonatites at Aillik Bay, Labrador: a Consequence of Incipient Lithospheric Thinning beneath the North Atlantic Craton

SEBASTIAN TAPPE[1,2]*, STEPHEN F. FOLEY[2], GEORGE A. JENNER[3], LARRY M. HEAMAN[4], BRUCE A. KJARSGAARD[5], ROLF L. ROMER[6], ANDREAS STRACKE[1], NANCY JOYCE[5] AND JOCHEN HOEFS[7]

[1]MAX-PLANCK-INSTITUT FÜR CHEMIE, POSTFACH 3060, 55020 MAINZ, GERMANY

[2]INSTITUT FÜR GEOWISSENSCHAFTEN, UNIVERSITÄT MAINZ, BECHERWEG 21, 55099 MAINZ, GERMANY

[3]DEPARTMENT OF EARTH SCIENCES, MEMORIAL UNIVERSITY, ST. JOHN'S, NEWFOUNDLAND, CANADA A1B 3X5

[4]DEPARTMENT OF EARTH AND ATMOSPHERIC SCIENCES, UNIVERSITY OF ALBERTA, EDMONTON, ALBERTA, CANADA T6G 2E3

[5]GEOLOGICAL SURVEY OF CANADA, OTTAWA, ONTARIO, CANADA K1A 0E8

[6]GEOFORSCHUNGSZENTRUM POTSDAM, TELEGRAFENBERG, 14473 POTSDAM, GERMANY

[7]GEOCHEMISCHES INSTITUT, UNIVERSITÄT GÖTTINGEN, GOLDSCHMIDTSTRASSE 1, 37077 GÖTTINGEN, GERMANY

RECEIVED JULY 16, 2004; ACCEPTED FEBRUARY 3, 2006; ADVANCE ACCESS PUBLICATION MARCH 14, 2006

Numerous dykes of ultramafic lamprophyre (aillikite, mela-aillikite, damtjernite) and subordinate dolomite-bearing carbonatite with U–Pb perovskite emplacement ages of ~590–555 Ma occur in the vicinity of Aillik Bay, coastal Labrador. The ultramafic lamprophyres principally consist of olivine and phlogopite phenocrysts in a carbonate- or clinopyroxene-dominated groundmass. Ti-rich primary garnet (kimzeyite and Ti-andradite) typically occurs at the aillikite type locality and is considered diagnostic for ultramafic lamprophyre–carbonatite suites. Titanian aluminous phlogopite and clinopyroxene, as well as comparatively Al-enriched but Cr–Mg-poor spinel (Cr-number < 0.85), are compositionally distinct from analogous minerals in kimberlites, orangeites and olivine lamproites, indicating different magma geneses. The Aillik Bay ultramafic lamprophyres and carbonatites have variable but overlapping $^{87}Sr/^{86}Sr_i$ ratios (0·70369–0·70662) and show a narrow range in initial ε_{Nd} (+0·1 to +1·9) implying that they are related to a common type of parental magma with variable isotopic characteristics. Aillikite is closest to this primary magma composition in terms of MgO (~15–20 wt %) and Ni (~200–574 ppm) content; the abundant groundmass carbonate has $\delta^{13}C_{PDB}$ between −5·7 and −5‰, similar to primary mantle-derived carbonates, and $\delta^{18}O_{SMOW}$ from 9·4 to 11·6‰. Extensive melting of a garnet peridotite source region containing carbonate- and phlogopite-rich veins at ~4–7 GPa triggered by enhanced lithospheric extension can account for the volatile-bearing, potassic, incompatible element enriched and MgO-rich nature of the proto-aillikite magma. It is argued that low-degree potassic silicate to carbonatitic melts from upwelling asthenosphere infiltrated the cold base of the stretched lithosphere and solidified as veins, thereby crystallizing calcite and phlogopite that were not in equilibrium with peridotite. Continued Late Neoproterozoic lithospheric thinning, with progressive upwelling of the asthenosphere beneath a developing rift branch in this part of the North Atlantic craton, caused further veining and successive remelting of veins plus volatile-fluxed melting of the host fertile garnet peridotite, giving rise to long-lasting hybrid ultramafic lamprophyre magma production in conjunction with the break-up of the Rodinia supercontinent. Proto-aillikite magma reached the surface only after coating the uppermost mantle conduits with glimmeritic material, which caused minor alkali loss. At intrusion level, carbonate separation from this aillikite magma resulted in

*Corresponding author. Present address: Department of Earth and Atmospheric Sciences, University of Alberta, Edmonton, Alberta, Canada T6G 2E3. Telephone: +49-06131-39-24759. Fax: +49-06131-39-23070. E-mail: stappe@ualberta.ca

fractionated dolomite-bearing carbonatites ($\delta^{13}C_{PDB}$ −3·7 to −2·7‰) and carbonate-poor mela-aillikite residues. Damtjernites may be explained by liquid exsolution from alkali-rich proto-aillikite magma batches that moved through previously reaction-lined conduits at uppermost mantle depths.

KEY WORDS: *liquid immiscibility; mantle-derived magmas; metasomatism, Sr–Nd isotopes; U–Pb geochronology*

INTRODUCTION

The ultramafic lamprophyres (UML; Rock, 1986) are a widely recognized group of alkaline igneous rocks associated with continental extension; however, their origin is poorly understood. Although they are volumetrically minor components of continental magmatism, they are of fundamental significance for our understanding of deep melting events during the initial stages in the development of continental rifts. UML typically occur as dyke swarms and in central complexes (Rock, 1991), but their genesis has commonly been discussed as though they are varieties of kimberlite (Dawson, 1971; Griffin & Taylor, 1975; Raeside & Helmstaedt, 1982; Alibert & Albarède, 1988; Dalton & Presnall, 1998) mainly as a result of a similar macroscopic appearance and often problematic identification within existing classification schemes (Tappe *et al.*, 2005*a*). However, compositional differences and the lack of spatial coexistence between contemporaneous UML and kimberlites (Rock, 1991; Mitchell, 1995) suggest that they are derived from distinct magma types. The occurrence of UML is largely confined to regions of lithospheric extension and they are commonly associated with carbonatite magmatism. Additionally, UML magmatism forms the earliest igneous activity in some flood basalt provinces (Queen *et al.*, 1996; Leat *et al.*, 2000; Riley *et al.*, 2003) and also occurs on oceanic plateaux (Nixon *et al.*, 1980; Neal & Davidson, 1989). In contrast, kimberlites occur exclusively within areas of stable Archean cratons or in the surrounding Proterozoic mobile belts (Mitchell, 1986; Janse & Sheahan, 1995). As for kimberlites, UML magmas may contain diamonds (Hamilton, 1992; Mitchell *et al.*, 1999; Digonnet *et al.*, 2000; Birkett *et al.*, 2004), indicating that the depth of melting can be in excess of 150 km (>5 GPa), and, thus, may not be the crucial petrogenetic difference.

Large areas of Labrador, adjacent northeastern Quebec and western Greenland consist of Archean blocks surrounded by Paleoproterozoic mobile belts (Fig. 1) stabilized at ~1900–1700 Ma (Wardle & Hall, 2002). Continental extension affected this cratonic area repeatedly during Mesoproterozoic (~1350–1140 Ma; Romer *et al.*, 1995; Upton *et al.*, 2003), Neoproterozoic (~620–550 Ma; Gower *et al.*, 1986; Kamo *et al.*, 1989; Larsen & Rex, 1992; Murthy *et al.*, 1992) and Mesozoic times (Hansen, 1980; Keen *et al.*, 1994; Chian *et al.*, 1995; Larsen *et al.*, 1999; Srivastava & Roest, 1999), eventually causing the break-up of the North Atlantic craton and opening of the Labrador Sea at ~60 Ma (Chalmers & Laursen, 1995; Chalmers & Pulvertaft, 2001).

All of these extensional episodes were accompanied by volatile-rich alkaline igneous activity (Larsen & Rex, 1992), but the most productive, in terms of UML magma generation, was the Late Neoproterozoic episode, which was distally associated with initiation of the Iapetus Ocean (Tappe *et al.*, 2004). Neoproterozoic UML dykes related to this lithospheric stretching occur in the Sisimiut–Sarfartoq–Maniitsoq areas of western Greenland (Scott, 1981; Thy *et al.*, 1987; Larsen & Rex, 1992; Mitchell *et al.*, 1999; Heaman, 2005), the Torngat Mountains in northern Quebec and Labrador (Digonnet *et al.*, 2000; Tappe *et al.*, 2004), the Otish Mountains region in central–north Quebec (Heaman *et al.*, 2004), single occurrences along the northern Labrador coast at Hebron, Saglek, Eclipse Harbour, Iselin Harbour and Killinek Island (Tappe *et al.*, 2005*b*), and Aillik Bay in central-east Labrador (Malpas *et al.*, 1986; Foley, 1989*a*).

Here, we report the results of a petrological and geochemical study, combined with U–Pb perovskite and $^{40}Ar/^{39}Ar$ phlogopite age determinations, on a diverse suite of Neoproterozoic UML and associated carbonatites from the Aillik Bay area on the Labrador Sea coast. We discuss whether the large compositional diversity reflects mantle source heterogeneity or variability in the melting process, or relates to modification of a common parental UML magma by low-pressure processes, such as liquid immiscibility and devolatilization. Additionally, we specify and emphasize fundamental differences in the characteristics and genesis of UML and other ultramafic magma types, such as kimberlites. Late Neoproterozoic UML magma production occurred throughout the North Atlantic region attendant with widespread lithospheric stretching, thinning and the eventual break-up of the supercontinent Rodinia.

GEOLOGY OF THE AILLIK BAY AREA

The southern North Atlantic craton margin

The Aillik Bay area is situated within the Paleoproterozoic Makkovik orogen at the southern edge of the Archean North Atlantic craton (NAC; Fig. 1). Reworked Archean orthogneisses (protolith ages 3260–2800 Ma) equivalent to the adjacent NAC are exposed along the western margin of the Makkovik Province (Fig. 2), whereas a juvenile high-grade magmatic arc crust dominates the central (Aillik Group) and eastern part close to the Grenville deformation front (Culshaw *et al.*, 2000*a*,

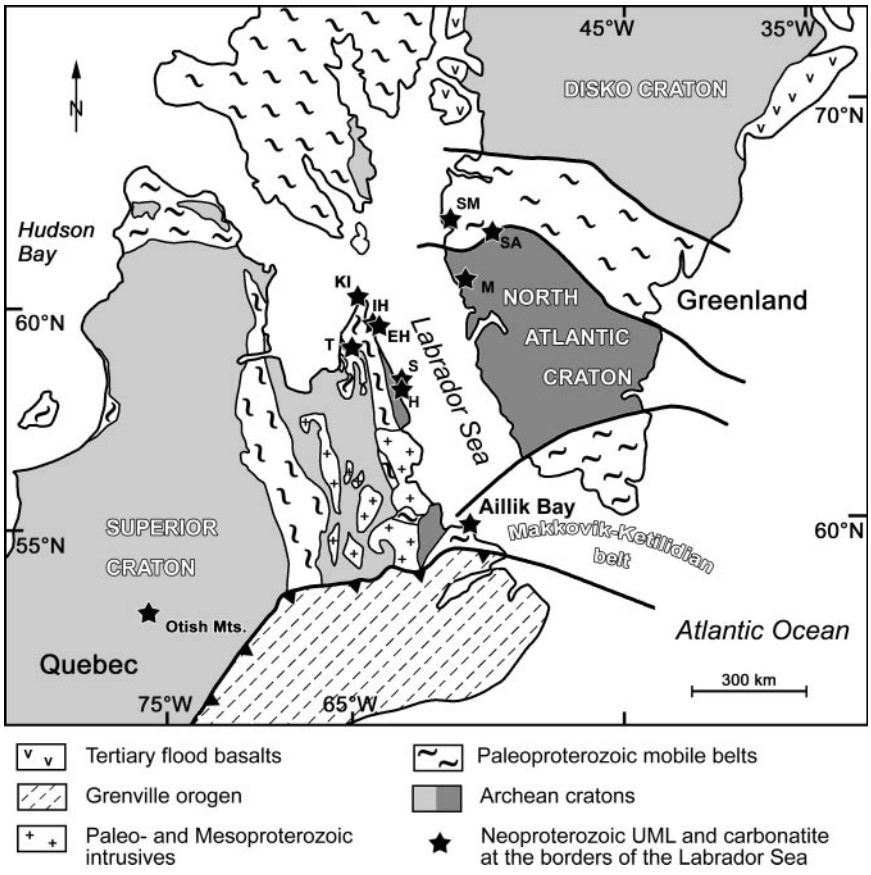

Fig. 1. Simplified geology of the northeastern Canadian–Greenland Shield restored for the Cenozoic drift of Greenland as apparent from the misfit of the present-day geographical coordinates (modified from Connelly *et al.*, 2000). Abbreviations for Neoproterozoic ultramafic lamprophyre (UML) and carbonatite occurrences are: EH, Eclipse Harbour; H, Hebron; IH, Iselin Harbour; KI, Killinek Island; M, Maniitsoq; S, Saglek; SA, Sarfartoq; SM, Sisimiut; T, Torngat/Abloviak.

2000*b*; Sinclair *et al.*, 2002). These supracrustal units formed during a sequence of subduction and accretion events between ~1900 and 1700 Ma (Makkovikian Orogeny) and were later detached from the basement and thrust onto the edge of the NAC (Ketchum *et al.*, 2002; Wardle & Hall, 2002). Seismic data and the unradiogenic initial Nd isotope composition of widespread post-orogenic granites (~1720–1650 Ma; e.g. Strawberry granite in Fig. 2) clearly indicate that the western part of the Makkovik orogen, including the Aillik Bay area (Fig. 2), is underlain by the Archean crust of the NAC (Kerr & Fryer, 1994; Hall *et al.*, 1995; Kerr & Wardle, 1997; Kerr *et al.*, 1997).

Widespread lithospheric thinning occurred throughout eastern North America along the former Laurentian margin during the Late Neoproterozoic (Bond *et al.*, 1984; Kamo *et al.*, 1995; Torsvik *et al.*, 1996; Cawood *et al.*, 2001; Puffer, 2002), resulting in continental break-up and subsequent opening of the Iapetus Ocean at ~600 Ma. In central Labrador, this episode of continental stretching is recorded by remnant graben structures forming the eastward continuation of the prominent St. Lawrence valley rift system (Gower *et al.*, 1986; Murthy *et al.*, 1992).

Alkaline magmatism and previous age constraints

Late Neoproterozoic UML and carbonatite dykes occur in an area at least 30 km by 30 km around Aillik Bay (Fig. 2; Appendix A). These dykes are narrow (up to 3 m wide) and dominantly steeply dipping; subordinate flat-lying sheets also occur. Recognized UML types are aillikite, mela-aillikite and damtjernite, following the scheme devised by Tappe *et al.* (2005*a*). The subvertical dykes are roughly north–south-oriented and appear to converge towards a focus in the Labrador Sea (Fig. 2). Flow banding, back-veining and internal chill-bands are often seen, whereas fluidized globular 'autolithic' segregations are rare. Individual members of this dyke swarm cross-cut each other in a rather arbitrary manner. Some aillikite sheets or dykes grade laterally into carbonatite and/or mela-aillikite (Fig. 3). A weighted K–Ar mica age of 570 Ma, obtained for a poorly described ultramafic

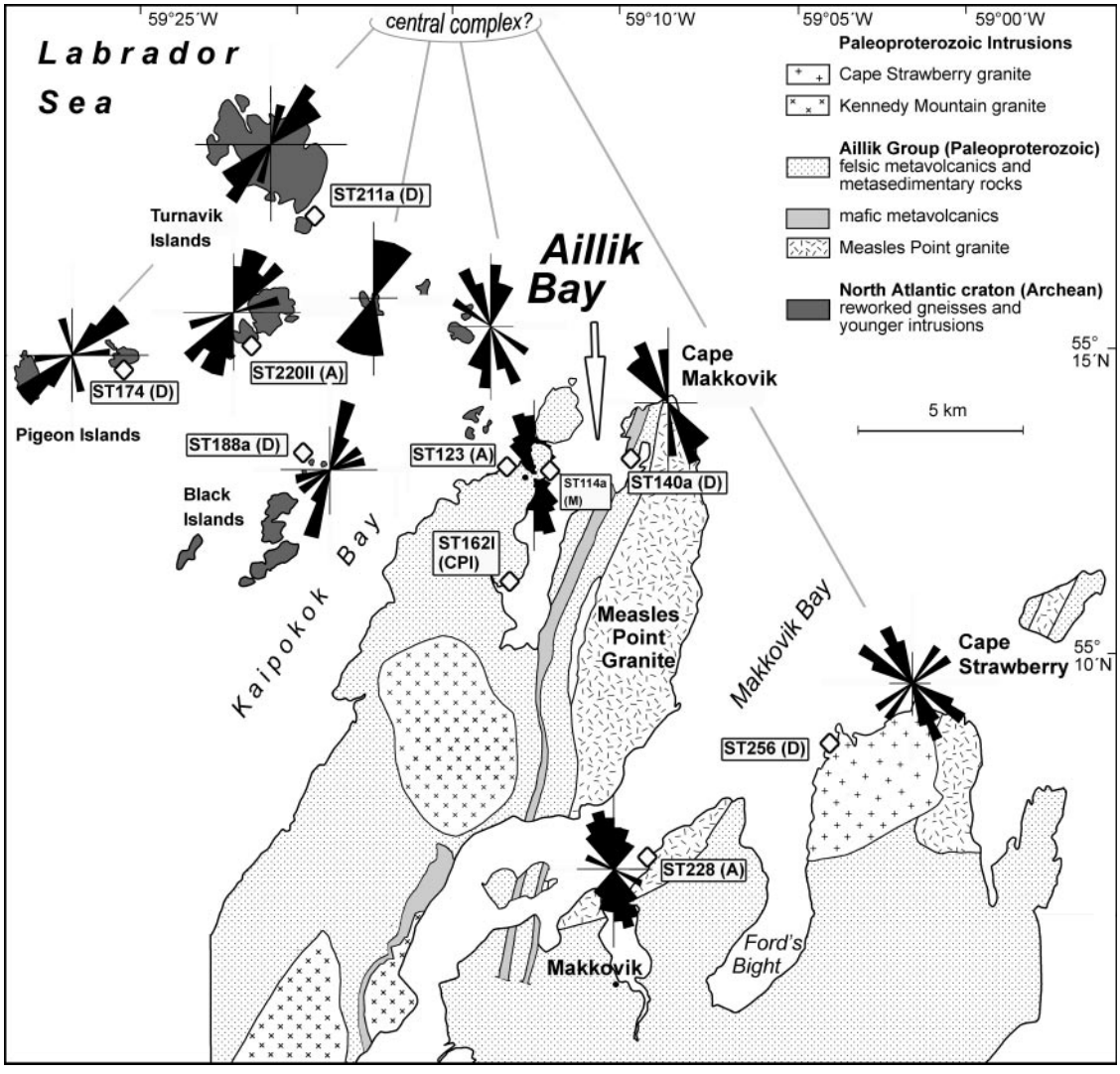

Fig. 2. Simplified geological map of the Aillik Bay area based on Sinclair *et al.* (2002). Rose diagrams illustrate the orientation of steeply dipping (>45°) ultramafic lamprophyre and carbonatite dykes of the Late Neoproterozoic Aillik Bay intrusive suite. Single diagrams are compiled either from longer coastal sections or groups of neighbouring islands and suggest dyke convergence to a focus in the Labrador Sea. Open diamonds indicate sample locations for U–Pb perovskite dated aillikites (A), mela-aillikite (M) and damtjernites (D), as well as the $^{40}Ar/^{39}Ar$ phlogopite dated clinopyroxene–phlogopite cognate inclusion (CPI).

dyke rock from Aillik Bay (Leech *et al.*, 1962), provided the only age constraint for the carbonate-rich magmatism when this study was initiated.

UML magmatism was preceded by Mesoproterozoic ultrapotassic magma production (~1374 Ma; Tappe *et al.*, in preparation), represented by subvertical, 0·2–2 m wide, fine- to medium-grained olivine lamproite dykes within the same area. The youngest record of alkaline igneous activity around Aillik Bay is a Mesozoic suite of melilitite, nephelinite and basanite dykes (~142 Ma; Tappe *et al.*, in preparation), which appears to be related to the poorly exposed Ford's Bight alkaline intrusion (King & McMillan, 1975).

GEOCHRONOLOGY

U–Pb dating of ultramafic lamprophyres

Aillikite, mela-aillikite and damtjernite dykes were selected from all parts of the Aillik Bay area for U–Pb perovskite dating (Fig. 2). Analytical details can be found in Appendix B. Results are reported in Table 1 and displayed in concordia diagrams in Fig. 4. Two perovskite fractions of aillikite dyke ST123 from the east shore of Kaipokok Bay yielded similar $^{206}Pb/^{238}U$ dates of 560·7 ± 2·4 and 564·5 ± 3·0 Ma, respectively. Hence, a weighted average $^{206}Pb/^{238}U$ date of 562·2 ± 1·9 Ma is considered the best age estimate for emplacement of

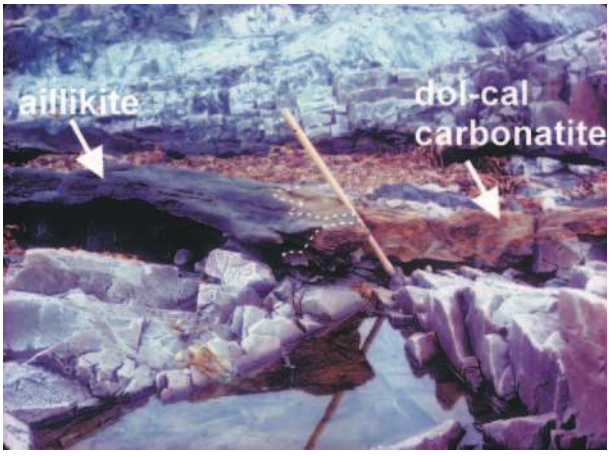

Fig. 3. Flat-lying aillikite sheet from Cape Makkovik. The dark-coloured aillikite at the left grades into yellowish dolomite–calcite carbonatite at the right with the hammer being close to the interface (~1 m long).

dyke ST123. A similar $^{206}Pb/^{238}U$ age of 569·2 ± 1·8 Ma was obtained from mela-aillikite dyke ST114A exposed on the west shore of Aillik Bay. The emplacement age of aillikite dyke ST228 from the southern shore of Makkovik Bay was determined to be 576·4 ± 6·5 Ma (weighted average $^{206}Pb/^{238}U$ date of two perovskite fractions 574·4 ± 1·8 Ma and 578·6 ± 2·0 Ma). The emplacement age of aillikite dyke ST220II from West Turnavik Island is 589·6 ± 1·3 Ma (weighted average of 589·4 ± 1·4 and 590·5 ± 2·8 Ma).

The youngest perovskite ages obtained from damtjernite dykes are 555·0 ± 1·8 Ma (ST211A; Main Turnavik Island) and 563·9 ± 2·5 Ma (ST256; east shore of Makkovik Bay). Perovskites from damtjernite dyke ST174 (Pigeon Island) yielded a $^{206}Pb/^{238}U$ date of 574·6 ± 1·6 Ma. Strikingly similar weighted average ages of 581·9 ± 2·3 Ma (582·5 ± 4·8 and 581·9 ± 2·6 Ma) and 582·5 ± 2·1 Ma (582·8 ± 3 and 582·1 ± 2·2 Ma) were obtained from the damtjernites ST140A (east shore of Aillik Bay) and ST188A (Red Island), respectively.

Taken together, the high-precision $^{206}Pb/^{238}U$ perovskite dates for four individual aillikite/mela-aillikite dykes and five damtjernite dykes cover a similar age range between 562–590 Ma and 555–583 Ma, respectively (Fig. 4). Hence, aillikite and damtjernite magmatism can be considered coeval over 30–35 Myr during Late Neoproterozoic extension at a craton margin. Although no carbonatites have been dated, their close association with the various dated UML types implies contemporaneous emplacement.

$^{40}Ar/^{39}Ar$ dating of cognate inclusion ST162I

A clinopyroxene–phlogopite inclusion recovered from aillikite dyke ST162 on the west shore of Aillik Bay (Fig. 2) yielded a phlogopite $^{40}Ar/^{39}Ar$ plateau age of 573·3 ± 3·3 Ma (Table 2), which falls within the U–Pb perovskite age range of the four dated aillikite dykes.

The plateau was calculated over 10 consecutive steps, which contained 98% of the total released ^{39}Ar. The gas release spectrum is shown in Fig. B1 (Appendix B). The 3·5%, 3·9% and 4·2% laser power steps significantly overlap the plateau but have slightly older apparent ages, indicating a potential presence of excess argon. However, on an inverse isochron diagram, a regression through these three data points and the seven others included in the plateau age calculation passes through a $^{40}Ar/^{36}Ar$ value of 433·1 ± 257·7, which is within error of the atmospheric value (295·5). As the three apparently older steps have no significant effect on the overall age, they have been included in the plateau age calculation.

PETROGRAPHY

Rock types of the Neoproterozoic Aillik Bay UML suite include carbonatite, aillikite, mela-aillikite and damtjernite, listed in order of decreasing carbonate content. Additionally, aillikite dykes host a wide variety of micaceous cognate inclusions (Fig. 5). Modal mineral abundances are listed in Table 3 and mineral compositional data are given in Tables 4–11 (extended tables can be downloaded from the *Journal of Petrology* website at http://www.petrology.oupjournals.org as Electronic Appendix 1). It should be noted that descriptions of the following accessory minerals are solely provided as Electronic Appendix 2: ilmenite, rutile, perovskite, titanite, apatite, alkali feldspar, feldspathoids, pectolite.

Carbonatite dykes

Two distinct types of carbonatite can be distinguished: (1) a dolomite carbonatite devoid of any mafic silicates; (2) a mixed dolomite–calcite carbonatite containing minor amounts of clinopyroxene, phlogopite and olivine crystals. The dolomite carbonatite mainly consists of a mosaic of equigranular Fe-rich dolomite crystals (100–300 μm). Hydroxy-fluorapatite forms abundant euhedral microphenocrysts (50–150 μm). Interstices may be filled by barite, quartz, alkali feldspar (orthoclase and albite) and/or tiny rare earth element (REE)-carbonate crystals. Large rutile grains commonly occur (50–100 μm), whereas opaque phases including magnetite are comparatively rare.

The dolomite–calcite carbonatites exhibit a granular to interlocking texture dominated by calcite grains and laths (150–300 μm). Calcite coexists with subordinate laths of Fe-rich dolomite (Fig. 6a). Zoned phlogopite plates (up to 0·5 mm) and olivine grains (up to 1·0 mm; replaced by carbonates) are observed, suggesting gradation into aillikites. However, the presence of diopside-rich

Table 1: U–Pb perovskite results for ultramafic lamprophyres from the Aillik Bay area

Description*	Wt (μg)	U (ppm)	Th (ppm)	Pb (ppm)	Th/U	TCPb (pg)	$^{206}Pb/^{204}Pb$	$^{238}U/^{204}Pb$	$^{206}Pb/^{238}U$†	$^{207}Pb/^{235}U$†	$^{207}Pb/^{206}Pb$†	Apparent ages (Ma)			
												$^{206}Pb/^{238}U$	$^{207}Pb/^{235}U$	$^{207}Pb/^{206}Pb$	Discordance (%)
ST123 (aillikite)															
1. dk brn subhed cubes/ octahedrons M@0·3A (70)	60	109	746	31	6·82	179	227·4 ± 0·6	2306·1 ± 8·3	0·09087 ± 20	0·7410 ± 49	0·05914 ± 38	560·7 ± 1·2	562·9 ± 2·9	572·4 ± 13·9	2·13
2. dk brn subhed cubes/ octahedrons M@0·3A (230)	169	138	892	37	6·45	575	251·7 ± 1·2	2555·6 ± 14·7	0·09152 ± 25	0·7406 ± 51	0·05869 ± 37	564·5 ± 1·5	562·8 ± 3·0	555·7 ± 13·8	−1·67
ST114A (mela-aillikite)															
1. brn/black irregular frags M@0·5A (80)	132	347	1660	77	4·79	742	373·2 ± 1·7	3849·7 ± 18·3	0·09232 ± 15	0·7536 ± 39	0·05921 ± 29	569·2 ± 0·9	570·3 ± 2·3	574·8 ± 10·6	1·01
ST228 (aillikite)															
1. black/brn frags MI@H (150)	52	86	349	18	4·08	113	249·0 ± 1·6	2481·5 ± 17·1	0·09319 ± 16	0·7561 ± 62	0·05884 ± 47	574·4 ± 0·9	571·7 ± 3·6	561·3 ± 17·2	−2·43
2. black/brn euhed cubes/ octahedrons MI@H (100)	55	101	389	22	3·86	209	178·2 ± 2·0	1708·2 ± 21·5	0·09391 ± 17	0·7560 ± 73	0·05839 ± 55	578·6 ± 1·0	571·7 ± 4·2	544·3 ± 20·6	−6·59
ST220II (aillikite)															
1. black/brn irregular frags M@0·4A (95)	51	253	2002	79	7·90	188	428·1 ± 2·6	4285·7 ± 26·9	0·09575 ± 13	0·7924 ± 38	0·06002 ± 28	589·4 ± 0·7	592·5 ± 2·2	604·4 ± 9·9	2·57
2. brn flakes and frags M@0·4A	102	238	2027	78	8·54	356	425·8 ± 1·7	4253·2 ± 19·9	0·09592 ± 24	0·7902 ± 37	0·05974 ± 24	590·5 ± 1·4	591·3 ± 2·1	594·3 ± 8·5	0·67
ST211A (damtjernite)															
1. brn octahedrons M@0·5A (50)	17	85	2077	60	24·4	45	197·6 ± 2·1	2000·1 ± 23·4	0·08991 ± 14	0·7241 ± 58	0·05841 ± 46	555·0 ± 0·9	553·1 ± 3·4	545·0 ± 17·2	−1·91
ST256 (damtjernite)															
1. brn clear irregular frags M@0·5A (60)	91	79	486	24	6·15	522	96·59 ± 0·17	861·7 ± 2·0	0·09143 ± 42	0·7384 ± 125	0·05857 ± 103	563·9 ± 2·5	561·5 ± 7·3	551·3 ± 37·9	−2·40
ST174 (damtjernite)															
1. brn frags 0·3AM/NM	40	102	412	21	4·06	70	360·5 ± 5·7	3675·3 ± 58·6	0·09323 ± 14	0·7520 ± 89	0·05850 ± 65	574·6 ± 0·8	569·4 ± 5·2	548·5 ± 24·1	−4·99
ST140A (damtjernite)															
1. light brn frags M@0·5A (160)	117	45	161	10	3·57	210	167·4 ± 0·8	1581·7 ± 9·8	0·09458 ± 40	0·7661 ± 76	0·05875 ± 56	582·5 ± 2·4	577·5 ± 4·4	557·7 ± 20·6	−4·65
2. light brn frags M@0·5A (230)	184	76	279	16	3·66	471	195·4 ± 1·1	1880·0 ± 11·9	0·09447 ± 21	0·7630 ± 66	0·05858 ± 49	581·9 ± 1·3	575·7 ± 3·8	551·4 ± 18·3	−5·78
ST188A (damtjernite)															
1. brn octahedrons M@0·5A (200)	101	116	323	23	2·79	447	173·6 ± 0·4	1646·3 ± 4·5	0·09463 ± 25	0·7699 ± 67	0·05901 ± 53	582·8 ± 1·5	579·7 ± 3·9	567·6 ± 19·3	−2·81
2. dk brn euhed cubes/ octahedrons M@0·5A (240)	175	131	386	25	2·95	774	193·6 ± 0·6	1861·0 ± 7·2	0·09450 ± 19	0·7639 ± 60	0·05863 ± 46	582·1 ± 1·1	576·3 ± 3·5	553·4 ± 16·9	−5·42

*dk brn, dark brown; frags, fragments; M@0·3A, non-magnetic fraction at 0·3 A (Frantz); numbers in parentheses are numbers of grains analysed.
†Atomic ratios corrected for fractionation, blank (5 pg Pb; 1 pg U), isotopic tracer and initial common Pb (Stacey & Kramers, 1975). Th concentrations calculated based on amount of ^{208}Pb present and $^{207}Pb/^{206}Pb$ date. TCPb is total common Pb (initial Pb). All errors reported in this table are quoted at 1σ.

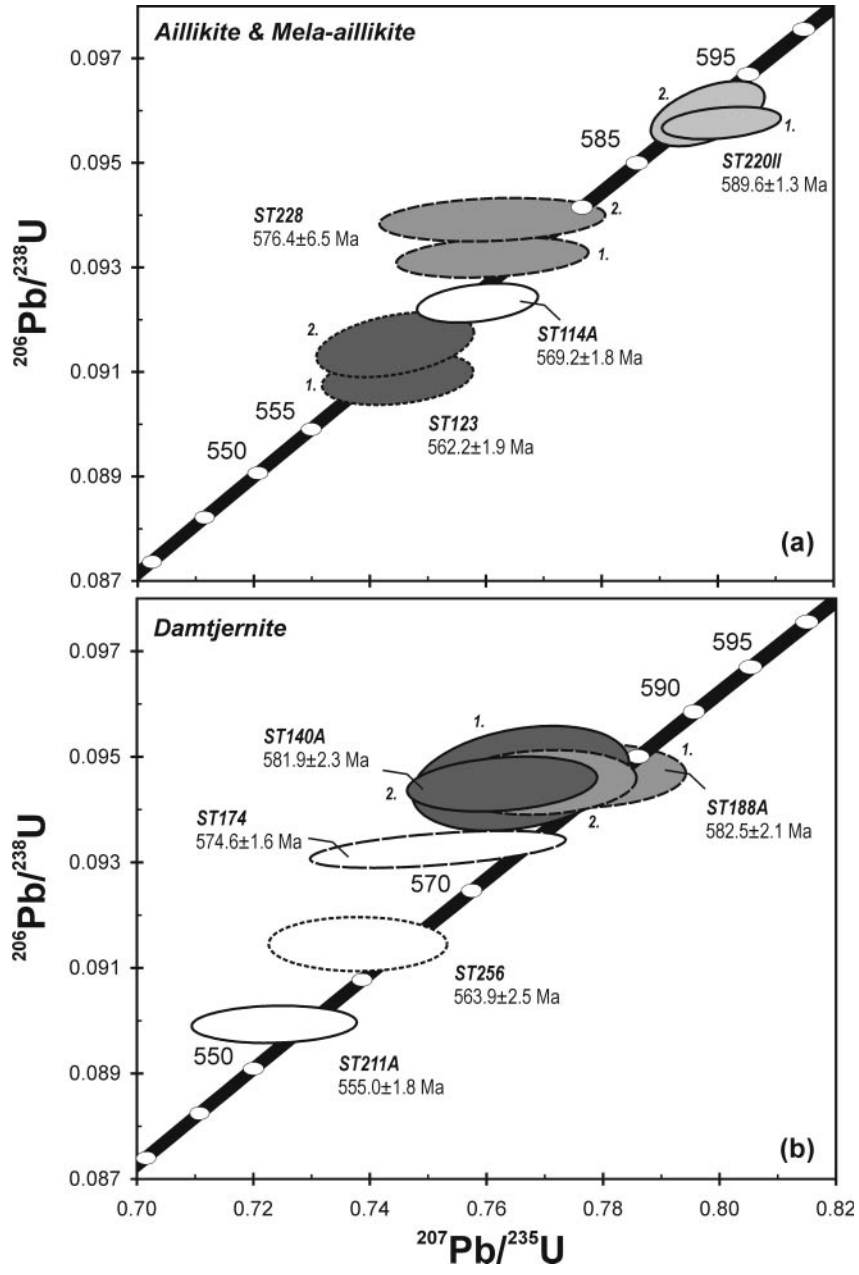

Fig. 4. U–Pb perovskite results for (a) aillikites/mela-aillikite and (b) damtjernites from the Aillik Bay area displayed in concordia diagrams. Reported ages are $^{206}Pb/^{238}U$ dates (quoted errors and error envelopes at 2σ), and in cases where two perovskite fractions were analyzed (1. and 2.) the weighted average $^{206}Pb/^{238}U$ date is given (see text and Table 1 for details).

clinopyroxene phenocrysts (up to 1·2 mm) contrasts with the aillikites. Fresh rutile grains and apatite prisms (up to 0·4 and 1·0 mm, respectively) are abundant, as are opaque oxides. Secondary interstitial barite and/or fluorite may occur.

Aillikite dykes

Aillikites are texturally heterogeneous (e.g. Fig. 5a and b); some exhibit an inequigranular texture with olivine and phlogopite macrocrysts up to 7 mm in diameter, whereas the majority are weakly inequigranular and have a porphyritic texture (Fig. 5b). Porphyritic aillikites are characterized by phenocrysts of euhedral to subhedral olivine (0·6–1·3 mm), phlogopite (0·25–0·5 mm), apatite and magnetite (0·2–0·4 mm) in a carbonate matrix. Mela-aillikites are distinguished from aillikites in containing more mafic silicate phases (>70 vol. %) and less carbonate (<10 vol. %). The change in the modal

Table 2: $^{40}Ar/^{39}Ar$ phlogopite results for clinopyroxene–phlogopite inclusion ST162I in aillikite dyke ST162 from Aillik Bay

Power[a] (%)	Volume ^{39}Ar (10^{-11} cm^{-3})	$^{36}Ar/^{39}Ar$	$^{37}Ar/^{39}Ar$	$^{38}Ar/^{39}Ar$	$^{40}Ar/^{39}Ar$	^{40}Ar (%)	$*^{40}Ar/^{39}Ar$	f_{39}[b] (%)	apparent age[c] (Ma)
2·4	0·1977	0·0083 ± 0·0108	0·266 ± 0·044	0·117 ± 0·013	8·4 ± 3·6	29·4	5·9 ± 4·7	0·3	258·8 ± 190·3
2·8	0·3061	0·0075 ± 0·0066	1·481 ± 0·053	0·109 ± 0·012	13·1 ± 2·2	16·9	10·9 ± 2·9	0·5	450·3 ± 107·8
3·0	0·6339	0·0028 ± 0·0034	0·108 ± 0·013	0·075 ± 0·012	13·2 ± 1·1	6·3	12·3 ± 1·5	1·1	504·0 ± 52·3
3·5*	1·5591	0·0013 ± 0·0014	0·025 ± 0·006	0·030 ± 0·011	14·9 ± 0·4	2·6	14·5 ± 0·6	2·7	**579·2 ± 20·9**
3·9*	2·0935	0·0004 ± 0·0009	0·001 ± 0·006	0·017 ± 0·011	14·5 ± 0·3	0·9	14·4 ± 0·4	3·6	**575·0 ± 14·7**
4·2*	4·4797	0·0010 ± 0·0006	0·001 ± 0·004	0·020 ± 0·011	14·8 ± 0·2	2·1	14·5 ± 0·2	7·7	**577·5 ± 7·8**
4·6*	4·7271	0·0002 ± 0·0003	0·002 ± 0·001	0·019 ± 0·011	14·4 ± 0·2	0·4	14·4 ± 0·2	8·1	**574·6 ± 6·7**
5·0*	5·0276	0·0000 ± 0·0005	0·001 ± 0·005	0·019 ± 0·011	14·3 ± 0·1	0·0	14·3 ± 0·2	8·6	**573·5 ± 7·0**
5·5*	5·8664	0·0001 ± 0·0003	0·003 ± 0·002	0·020 ± 0·011	14·4 ± 0·1	0·2	14·4 ± 0·2	10·0	**574·2 ± 5·5**
6·0*	8·5068	0·0002 ± 0·0002	0·013 ± 0·002	0·019 ± 0·011	14·3 ± 0·1	0·3	14·4 ± 0·1	14·5	**572·3 ± 4·3**
6·5*	7·5095	0·0002 ± 0·0002	0·010 ± 0·002	0·020 ± 0·011	14·4 ± 0·1	0·3	14·3 ± 0·1	12·8	**573·3 ± 4·1**
7·5*	12·3507	0·0001 ± 0·0001	0·003 ± 0·001	0·021 ± 0·011	14·3 ± 0·1	0·2	14·3 ± 0·1	21·1	**572·7 ± 2·5**
13·0*	5·2965	0·0004 ± 0·0004	0·005 ± 0·001	0·020 ± 0·011	14·4 ± 0·2	0·9	14·3 ± 0·2	9·1	**572·7 ± 6·6**
									***plateau* = 573·3 ± 3·3**

*Denotes steps used in the calculation of the plateau age (573.3 ± 3.3 Ma).
[a]As measured by laser in % of full nominal power (10W).
[b]Fraction ^{39}Ar as percent of total run.
[c]Errors are analytical only and do not reflect error in irradiation parameter J.
nominal J = 0·02610; referenced to PP-20 Hornblende (Hb3gr equivalent) = 1072 Ma (Roddick, 1983). All errors reported in this table are quoted at 2σ.

mineral proportions is gradational from aillikite to mela-aillikite. End-member mela-aillikite contains abundant clinopyroxene prisms in the groundmass (100–300 μm; Fig. 5c), which are rare in aillikite. Both rock types carry microphenocrysts of olivine (0·25–0·5 mm), phlogopite (<0·25 mm), apatite, opaque oxides (dominantly titanomagnetite and Mg-rich ilmenite) and perovskite or rutile (50–200 μm). Primary kimzeyitic garnet typically occurs (<100 μm).

A rare textural variety occurs locally in otherwise uniformly textured aillikite dykes and consists of globular aillikite segregations 'cemented' by primary calcite laths. The globular segregations are made up of olivine and/or glimmerite kernels surrounded by concentrically arranged fine-grained aillikite matrix (Fig. 5a). Their strong resemblance to nucleated autoliths suggests an origin by fluidization of partly solidified early magma fractions as a result of local near-surface devolatilization.

Damtjernite dykes

Damtjernites are medium- to fine-grained, porphyritic to intergranular rocks (Fig. 5d) containing rare macrocrysts (up to 2·0 cm) of virtually Cr-free diopside-rich clinopyroxene and/or Cr-free titanian aluminous phlogopite. Modal layering, internal chill zones, bounded felsic segregations, flow-alignment and rotation structures are common macroscopic features of these rocks, which were called 'sannaites' by Foley (1984) and Malpas *et al.* (1986), but have been renamed here following Tappe *et al.* (2005*a*).

The phenocryst assemblage of the damtjernites consists of olivine (up to 1 mm), phlogopite (up to 5 mm), rare clinopyroxene (250–800 μm) and apatite (up to 1 mm). The modal abundance of euhedral to subhedral olivine phenocrysts may vary even within dykes from 20 vol. % to only a few crystals. Phlogopite forms large plates typically enclosing clinopyroxene and apatite needles. The groundmass mainly consists of a mesh made up of clinopyroxene and apatite needles (up to 200 μm) and biotite flakes resembling the late rims on phlogopite. Sr-calcite, alkali feldspar (almost pure orthoclase and albite) and nepheline occur in variable but small modal proportions interstitial to the mica and clinopyroxene of the groundmass (Fig. 5d). Additional rare felsic phases are analcime and sodalite. Pectolite is observed as a fibrous replacement product of groundmass clinopyroxene or as primary crystals in interstices. Olivine is absent in the groundmass. Abundant titanomagnetite grains, ilmenite laths, and rutile or perovskite crystals are the principal groundmass oxide phases. Perovskite relicts may be enclosed by Zr-rich titanite crystals recording fluctuations

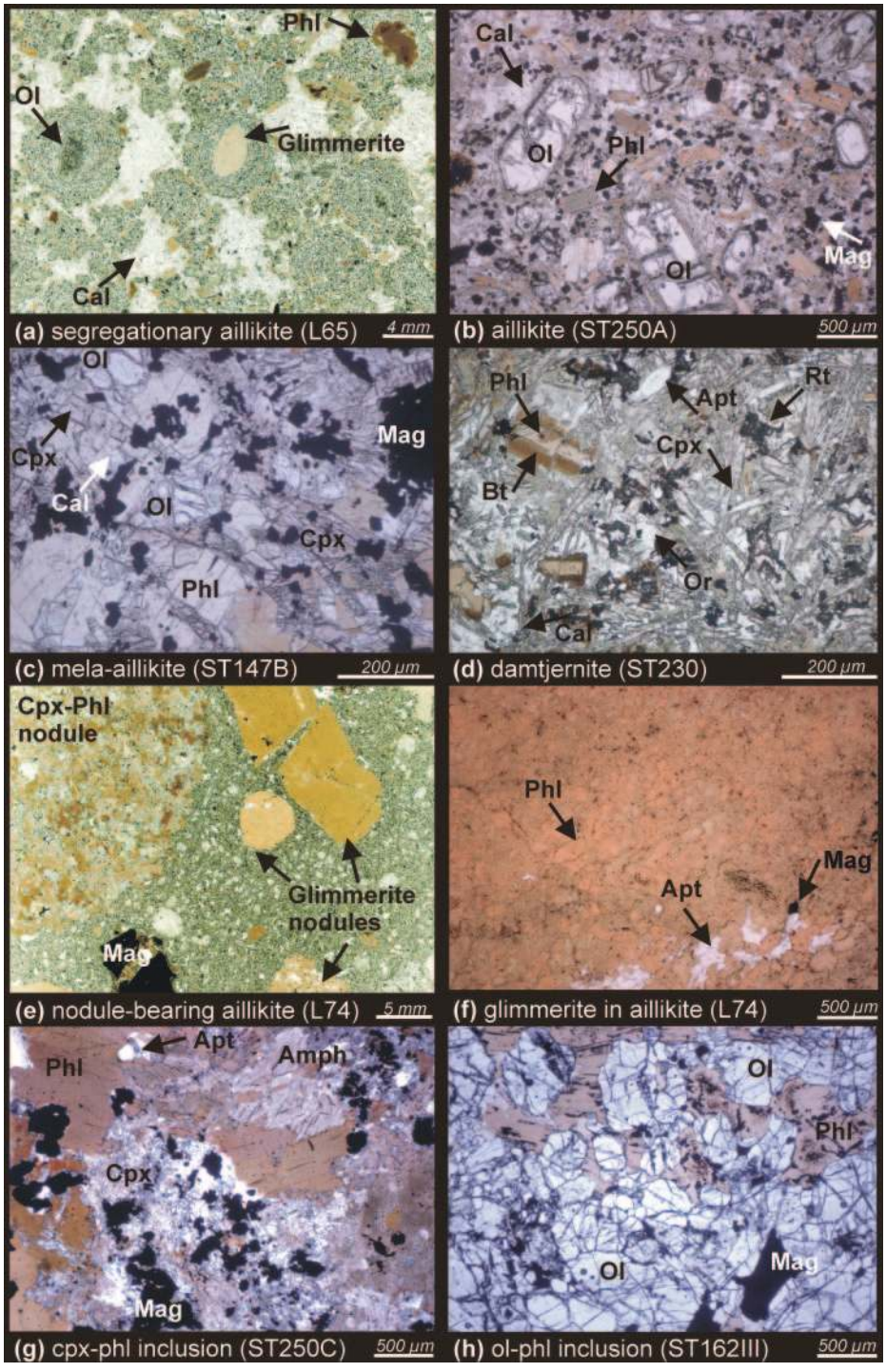

Fig. 5. Photomicrographs of the Aillik Bay area UML and associated cognate inclusions. (a) Globular aillikite segregations cemented by calcite laths. The segregations resemble nucleated autoliths, which contain kernels of early olivine and fragments from cognate inclusions surrounded by concentrically oriented aillikite matrix. (b) Porphyritic aillikite containing abundant olivine, phlogopite and spinel phenocrysts in a carbonate groundmass. (c) Intergranular mela-aillikite with abundant olivine, phlogopite, clinopyroxene and spinel. Carbonate is restricted to the interstices between the mafic silicates. (d) Damtjernite with phlogopite phenocrysts. These are rimed by dark biotite. Acicular groundmass clinopyroxene and apatite form a mesh with alkali feldspar, nepheline and carbonate as intercumulus phase. (e) Porphyritic aillikite with rounded cognate micaceous inclusions. (f) Glimmerite inclusion in aillikite consisting of interlocking phlogopite flakes, tiny opaque oxide grains and interstitial apatite. (g) Clinopyroxene–phlogopite nodule in aillikite consisting of large phlogopite plates with opaque oxide and apatite inclusions and clinopyroxene prisms, which are partly replaced by pargasitic amphibole. Calcic amphibole also occurs as larger intercumulus phase. (h) Cumulate-textured olivine–phlogopite cognate inclusion in aillikite. Symbols for minerals are according to Kretz (1983).

Table 3: Estimated modal mineral abundances (vol. % calculated out of 500 counted points) of representative UML and carbonatite dykes and their cognate inclusions from the Aillik Bay area

Locality/rock type	Ol (pc/mc)	Phl	Cpx	Amph/Pct	Afsp/Ne	Cal/Dol	opaques	Prv/Spn	Rt/Zcl	Adr	Ap	Srp*	Brt/Fl	Qtz†
Dyke rocks														
Dol carbonatite														
L1	–/–	–	–	–/–	1/–	–/90	2	–/–	4/–	–	3	–	x/–	x
Dol–cal carbonatite														
ST127	3/–	3	–	–/–	–/–	60/23	2	–/–	5/–	–	–	2	–/2	x
ST198C	–/–	3	9	–/–	–/–	55/17	4	–/–	8/–	–	5	–	x/–	–
ST199	–/–	11	18	–/–	–/–	45/15	1	–/–	5/–	–	4	–	x/–	1
ST231A	6/–	20	–	–/–	–/–	36/18	10	–/–	7/–	–	1	1	–/–	x
Aillikite														
L60	23/–	19	4	–/–	–/–	29/x	13	6/–	–/–	1	x	7	–/–	–
ST109	19/2	19	–	–/–	–/–	33/x	13	x/–	–/–	–	6	7	–/–	–
Mela-aillikite														
ST147B	19/–	22	29	–/–	–/–	7/x	14	1/–	1/–	x	x	5	–/–	–
ST210	22/–	22	28	–/–	–/–	10/x	8	–/–	4/–	–	x	6	–/–	–
ST244B	21/–	20	32	–/–	–/–	4/x	18	–/–	2/–	–	x	3	–/–	–
ST251B	25/2	26	18	–/–	–/–	9/x	9	2/–	1/–	–	2	8	–/–	–
Damtjernite														
ST188A	x/–	21	x	–/26	–/8	10/x	9	8/–	x/–	10	7	x	–/–	–
ST206AI	x/–	21	40	–/–	2/–	9/x	10	–/–	8/–	–	1	9	–/–	–
ST211A	x/–	20	30	–/–	–/11	7/x	7	15/8	x/–	–	2	x	–/–	–
ST224B	10/12	16	37	–/–	–/6	2/x	11	–/–	6/–	–	x	–	–/–	–
ST226	x/–	22	41	–/–	6/6	8/x	9	–/–	7/–	–	1	–	–/–	–
Cognate inclusions														
Glimmerite nodules	–	90–95	–	–/–	x/–	x/x	0–2	–/–	–/–	–	2–5	–	–/–	–
Cpx–phl nodules	0–20	30–60	25–50	0–10/–	–/–	x/x	5–10	–/x	–/–	–	0–5	x	–/–	–
Ol–phl nodules	20–70	20–50	0–5	–/–	–/–	x/x	3–10	x/–	–/x	–	0–5	x	–/–	–

*Primary serpentine.
†Quartz is secondary;
pc, phenocryst; mc, macrocryst; x, minor amounts; –, not detected. Symbols for minerals are according to Kretz (1983) except for Afsp (alkali feldspar) and Zcl (zirconolite).

in silica activity during magma evolution or slow cooling. Schorlomite and/or melanite garnet occurs rarely in the groundmass in association with perovskite (Fig. 6e). Felsic segregations (orthoclase, albite, nepheline, analcime, sodalite, calcite, Mg-ankerite) with fairly sharp contacts with the groundmass are a characteristic feature of the damtjernites (Foley, 1984).

Cognate inclusions

A suite of undeformed micaceous inclusions, exclusively hosted by aillikites, comprises (1) glimmerite, (2) clinopyroxene–phlogopite and (3) olivine–phlogopite nodules in order of decreasing abundance (Table 3).

Glimmerite nodules are typically oval and less than 2 cm in diameter (Fig. 5e); rare examples approach 5 cm. Most glimmerites consist of interlocking 20–100 μm phlogopite flakes (Fig. 5f); some contain larger isolated phlogopite 'clasts' (up to 500 μm). Fluorapatite and rare orthoclase fill interstices or form discontinuous bands (Fig. 5e and f) that may open into radiating patches. Tiny spinel and ilmenite grains (<100 μm; also composite) are scattered throughout the fine-grained matrix.

Clinopyroxene–phlogopite nodules (up to 8 cm across; Fig. 5e) are similar in shape to the glimmerites, but have more variable mineralogy and are coarser grained. Large poikilitic phlogopite plates and clinopyroxene prisms dominate (up to 2 mm), whereas lath-like to interstitial Mg-ilmenite, chromite–titanomagnetite and prismatic hydroxy-fluorapatite occur only as minor components (Fig. 5 g). Mica plates occasionally enclose carbonated subhedral olivine. A subtle grain-size layering was observed in larger nodules. Interstitial calcic

Table 4: Representative olivine compositions from the Aillik Bay area ultramafic lamprophyres and their cognate inclusions

Rock type:	ultramafic lamprophyres											cognate inclusions									
	aillikite				mela-aillikite			damtjernite				cpx−phl nodule				ol−phl nodule					
Mineral:	Ol	Ol	Ol	Ol	Ol	Ol	Ol	Ol	Ol	Ol	Ol	Ol	Ol	Ol	Ol	Ol	Ol	Ol	Ol	Ol	Ol
Sample no.:	L72	L72	L72	L72	ST244B	ST244B	ST244B	L7	L7	L47	L47	L6py	L6py	L6py	L6py	ST162IIdu	ST162IIdu	ST162IIdu	ST162IIdu	L49du	L49du
	pc2	pc2	pc2	pc2	mpc2	mpc2	mpc2	pc1	pc1	mpc1	mpc1	xx1	xx1	xx2	xx2	xx4	xx4	xx4	xx4	xx2	xx2
	core1	core2	rim1	rim2	core	rim1	rim2	core	rim	core	rim	core	rim	core	rim	core1	core2	rim1	rim2	core	rim
SiO_2	39·88	40·15	39·09	39·40	40·23	39·83	39·82	39·95	39·50	39·13	39·10	39·71	38·35	39·54	39·68	39·68	39·40	39·60	39·24	38·49	39·07
TiO_2	0·03	0·01	0·02	0·07	0·07	0·00	0·03	0·04	0·06	0·06	0·05	0·03	0·02	0·00	0·09	0·00	0·00	0·00	0·00	0·01	0·01
Al_2O_3	0·05	0·06	0·02	0·00	0·06	0·03	0·03	0·04	0·00	0·01	0·00	0·01	0·02	0·01	0·01	0·03	0·00	0·00	0·03	0·00	0·00
Cr_2O_3	0·05	0·07	0·10	0·01	0·05	0·10	0·02	0·05	0·00	0·06	0·07	0·00	0·00	0·02	0·00	0·07	0·07	0·09	0·03	0·00	0·01
FeO	10·15	10·61	16·32	13·71	12·05	14·25	14·47	14·89	15·81	16·38	17·80	14·05	18·12	13·33	16·03	14·93	14·42	16·40	16·61	19·03	18·86
MnO	0·17	0·14	0·15	0·22	0·09	0·15	0·24	0·11	0·18	0·18	0·25	0·55	0·39	0·70	0·34	0·23	0·16	0·42	0·35	0·25	0·22
NiO	0·45	0·38	0·27	0·12	0·43	0·21	0·14	0·44	0·19	0·43	0·28	0·03	0·02	0·00	0·08	0·42	0·37	0·26	0·19	0·22	0·27
MgO	48·75	48·19	44·12	45·55	48·45	46·52	46·85	44·83	43·83	43·89	42·34	45·87	41·77	45·86	43·89	45·50	45·90	44·47	43·86	41·82	41·83
CaO	0·12	0·12	0·11	0·17	0·15	0·25	0·36	0·18	0·44	0·16	0·20	0·07	0·31	0·06	0·33	0·14	0·13	0·16	0·11	0·02	0·03
Na_2O	0·02	0·06	0·01	0·00	0·03	0·00	0·03	0·00	0·02	0·01	0·01	0·00	0·01	0·01	0·02	0·00	0·02	0·01	0·00	0·00	0·00
K_2O	0·00	0·00	0·01	0·02	0·02	0·01	0·03	0·01	0·00	0·01	0·01	0·01	0·02	0·01	0·01	0·01	0·00	0·00	0·00	0·00	0·02
Total	99·66	99·80	100·22	99·27	101·63	101·34	102·02	100·53	100·03	100·31	100·12	100·33	99·03	99·54	100·47	101·01	100·47	101·40	100·41	99·84	100·32
No. oxygens	4	4	4	4	4	4	4	4	4	4	4	4	4	4	4	4	4	4	4	4	4
Si	0·982	0·990	0·984	0·991	0·978	0·981	0·974	0·999	0·996	0·986	0·995	0·989	0·987	0·990	0·997	0·986	0·980	0·986	0·988	0·985	0·996
Ti	0·001	0·000	0·000	0·001	0·001	0·000	0·001	0·001	0·001	0·001	0·001	0·001	0·000	0·000	0·002	0·000	0·000	0·000	0·000	0·000	0·000
Al	0·001	0·002	0·001	0·000	0·002	0·001	0·001	0·001	0·000	0·000	0·000	0·000	0·001	0·000	0·000	0·001	0·000	0·000	0·001	0·000	0·000
Cr	0·001	0·001	0·002	0·000	0·001	0·002	0·000	0·001	0·000	0·001	0·001	0·000	0·000	0·000	0·000	0·001	0·001	0·002	0·000	0·000	0·000
Fe^{3+}*	0·033	0·019	0·029	0·016	0·041	0·035	0·052	0·000	0·006	0·025	0·007	0·021	0·025	0·020	0·002	0·027	0·039	0·026	0·022	0·029	0·008
Fe^{2+}*	0·176	0·200	0·315	0·272	0·204	0·259	0·244	0·311	0·327	0·320	0·371	0·272	0·365	0·260	0·335	0·283	0·261	0·315	0·327	0·379	0·394
Mn	0·003	0·003	0·003	0·005	0·002	0·003	0·005	0·002	0·004	0·004	0·005	0·012	0·009	0·015	0·007	0·005	0·003	0·009	0·007	0·006	0·005
Ni	0·009	0·008	0·006	0·002	0·008	0·004	0·003	0·009	0·004	0·009	0·006	0·001	0·000	0·000	0·002	0·008	0·007	0·005	0·004	0·005	0·006
Mg	1·790	1·771	1·656	1·707	1·756	1·708	1·709	1·671	1·648	1·649	1·606	1·703	1·603	1·712	1·645	1·685	1·703	1·651	1·647	1·596	1·590
Ca	0·003	0·003	0·003	0·005	0·004	0·007	0·010	0·005	0·012	0·004	0·006	0·002	0·009	0·001	0·009	0·004	0·003	0·004	0·003	0·000	0·001
Na	0·001	0·003	0·000	0·000	0·002	0·000	0·002	0·000	0·001	0·001	0·000	0·000	0·001	0·001	0·001	0·000	0·001	0·000	0·000	0·000	0·000
K	0·000	0·000	0·000	0·001	0·001	0·000	0·001	0·000	0·000	0·000	0·000	0·000	0·001	0·000	0·000	0·000	0·000	0·000	0·000	0·000	0·001
Total cations	3·000	3·000	3·000	3·000	3·000	3·000	3·000	3·000	2·999	3·000	3·000	3·000	3·000	3·000	3·000	3·000	2·999	2·999	3·000	3·000	3·000
Mg-no.	91·1	89·9	84·0	86·3	89·6	86·9	87·5	84·3	83·4	83·8	81·2	86·2	81·5	86·8	83·1	85·6	86·7	84·0	83·4	80·8	80·1

Mg-number = 100[Mg/(Mg + Fe^{2+})] in atomic units; pc, phenocryst; mpc, microphenocryst; xx, crystal; Ol, olivine.
*Calculated assuming stoichiometry.

Table 5: Representative mica compositions of UML, carbonatite and their cognate inclusions from the Aillik Bay area

Rock type:	ultramafic lamprophyres and carbonatites																	cognate inclusions							
	aillikite					mela-aillikite					damtjernite				dol–cal carbonatite			glimmerite		cpx–phl nodule			ol–phl nodule		
Mineral:	Phl	Phl	Phl	TFP	TFP	Phl	Phl	Bt	Bt	Bt	Phl	Phl	Bt	Bt	Phl	Phl	TFP	Phl	Phl	Phl	Phl	Phl	Phl	Phl	Phl
Sample no.:	L66					ST244B					ST206AI				ST199			L74gI		ST122			ST162III		
	pc2 core1	pc2 core2	pc2 rim1	pc2 rim2	pc2 rim3	mpc1 core1	mpc1 core2	mpc1 rim1	mpc1 rim2	mpc1 rim3	pc4 core1	pc4 core2	pc4 rim1	pc4 rim2	pc5 core	pc5 rim1	pc5 rim2	xx2 core	xx2 rim	xx1 core1	xx1 core2	xx1 rim	xx2 core1	xx2 core2	xx2 rim
SiO_2	41·13	37·43	39·67	40·74	40·56	38·31	38·44	36·38	37·51	37·72	37·31	37·10	34·63	35·16	35·79	38·52	41·46	41·43	41·31	38·49	38·13	38·46	38·85	38·76	39·03
TiO_2	0·92	4·54	0·72	0·06	0·04	2·72	3·03	5·46	5·34	5·38	5·18	3·80	4·55	4·16	2·56	1·44	0·09	0·62	0·58	3·12	3·00	2·71	2·53	2·48	2·46
Al_2O_3	9·43	15·30	12·85	1·84	1·88	13·29	13·40	8·49	8·01	8·14	14·27	14·13	9·56	11·28	17·91	14·19	1·90	9·57	10·40	14·33	14·83	14·36	13·74	13·60	13·75
Cr_2O_3	0·01	0·02	0·07	0·08	0·02	0·03	0·01	0·03	0·08	0·06	0·05	0·04	0·09	0·04	0·02	0·04	0·06	0·00	0·01	0·06	0·00	0·05	0·66	0·64	0·63
FeO	9·05	6·99	5·80	14·77	14·09	10·25	10·05	28·41	28·84	28·19	7·76	11·29	34·97	26·51	6·25	6·23	12·72	6·92	5·89	9·46	9·68	9·81	6·27	6·24	6·11
MnO	0·04	0·04	0·09	0·24	0·16	0·13	0·05	0·35	0·29	0·37	0·03	0·22	0·73	0·44	0·02	0·20	0·32	0·08	0·07	0·06	0·10	0·10	0·02	0·00	0·00
MgO	24·55	20·93	24·87	26·59	26·59	21·05	20·76	7·44	7·78	7·62	20·44	18·68	3·28	8·79	21·50	24·24	27·31	24·41	25·20	20·46	20·35	20·75	23·06	22·90	22·91
CaO	0·00	0·02	0·15	0·20	0·20	0·03	0·05	0·20	0·14	0·15	0·02	0·00	0·07	0·67	0·21	0·21	0·46	0·02	0·03	0·09	0·04	0·10	0·14	0·05	0·16
BaO	0·02	0·42	0·47	0·06	0·07	0·00	0·08	0·04	0·08	0·00	0·55	0·50	0·18	0·40	1·42	0·62	0·09	0·04	0·10	0·67	0·84	0·60	0·29	0·42	0·32
Na_2O	0·37	0·40	0·33	0·08	0·14	0·86	0·89	0·42	0·52	0·50	0·48	0·49	0·11	0·17	0·46	0·43	0·28	0·05	0·08	1·02	1·09	1·05	0·99	0·94	0·75
K_2O	10·13	9·58	9·62	10·21	10·15	8·79	9·03	8·41	8·81	8·96	9·30	9·17	8·85	8·73	9·22	9·41	9·71	10·18	10·34	8·69	8·69	8·60	8·67	8·96	8·87
H_2O (calc)	3·55	3·92	3·96	3·79	3·79	3·88	3·92	3·64	3·61	3·68	3·77	3·74	3·61	3·65	3·93	3·86	3·26	3·08	3·06	3·98	3·98	3·90	3·95	3·80	3·82
F	1·26	0·51	0·49	0·56	0·57	0·51	0·44	0·26	0·31	0·20	0·77	0·71	0·03	0·26	0·46	0·66	1·74	2·25	2·34	0·29	0·28	0·46	0·51	0·80	0·78
Cl	0·00	0·00	0·00	0·00	0·00	0·00	0·00	0·00	0·01	0·01	0·01	0·01	0·01	0·01	0·00	0·00	0·01	0·00	0·01	0·02	0·01	0·02	0·01	0·01	0·02
O = F	−0·53	−0·21	−0·21	−0·24	−0·24	−0·22	−0·19	−0·11	−0·13	−0·08	−0·32	−0·30	−0·01	−0·11	−0·19	−0·28	−0·73	−0·95	−0·99	−0·12	−0·12	−0·19	−0·21	−0·33	−0·33
Total	99·92	99·87	98·87	98·97	98·03	99·64	99·96	99·42	101·19	100·89	99·63	99·57	100·64	100·16	99·55	99·78	98·66	97·69	98·42	100·62	100·89	100·77	99·46	99·27	99·28
No. oxygens	22	22	22	22	22	22	22	22	22	22	22	22	22	22	22	22	22	22	22	22	22	22	22	22	22
Si	5·912	5·399	5·730	5·988	6·006	5·570	5·574	5·745	5·816	5·856	5·404	5·471	5·626	5·523	5·197	5·541	6·055	6·055	5·978	5·554	5·502	5·547	5·575	5·587	5·614
^{IV}Al	1·598	2·601	2·188	0·318	0·328	2·277	2·290	1·580	1·464	1·489	2·436	2·456	1·830	2·088	2·803	2·406	0·327	1·648	1·774	2·437	2·498	2·441	2·324	2·311	2·331
$^{IV}Fe^{3+}$	0·490	0·000	0·082	1·694	1·666	0·152	0·136	0·674	0·721	0·655	0·159	0·073	0·544	0·389	0·000	0·053	1·618	0·297	0·249	0·009	0·000	0·013	0·101	0·102	0·055
[T]	8·0	8·0	8·0	8·0	8·0	8·0	8·0	8·0	8·0	8·0	8·0	8·0	8·0	8·0	8·0	8·0	8·0	8·0	8·0	8·0	8·0	8·0	8·0	8·0	8·0
Ti	0·099	0·493	0·078	0·006	0·005	0·297	0·331	0·649	0·623	0·628	0·564	0·422	0·556	0·492	0·280	0·156	0·010	0·068	0·063	0·339	0·326	0·294	0·273	0·269	0·266
^{VI}Al	0·000	0·000	0·000	0·000	0·000	0·000	0·000	0·000	0·000	0·000	0·000	0·000	0·000	0·000	0·262	0·000	0·000	0·000	0·000	0·000	0·024	0·000	0·000	0·000	0·000
Cr	0·001	0·002	0·008	0·009	0·003	0·003	0·001	0·004	0·010	0·007	0·006	0·004	0·011	0·004	0·002	0·004	0·006	0·000	0·001	0·007	0·000	0·006	0·075	0·073	0·072
Mg	5·261	4·501	5·356	5·826	5·870	4·563	4·488	1·752	1·798	1·764	4·414	4·107	0·794	2·058	4·654	5·198	5·946	5·318	5·436	4·401	4·377	4·461	4·933	4·921	4·913
Ca	0·000	0·003	0·023	0·031	0·031	0·005	0·007	0·034	0·023	0·026	0·003	0·000	0·012	0·113	0·032	0·033	0·071	0·003	0·005	0·014	0·006	0·015	0·021	0·008	0·024

Rock type:	ultramafic lamprophyres and carbonatites																	cognate inclusions							
	aillikite					mela-aillikite					damtjernite				dol–cal carbonatite			glimmerite		cpx–phl nodule			ol–phl nodule		
Mineral:	Phl	Phl	Phl	TFP	TFP	Phl	Phl	Bt	Bt	Bt	Phl	Phl	Bt	Bt	Phl	Phl	TFP	Phl	Phl	Phl	Phl	Phl	Phl	Phl	Phl
Sample no.:	L66					ST244B					ST206AI				ST199			L74gl		ST122			ST162III		
	pc2 core1	pc2 core2	pc2 rim1	pc2 rim2	pc2 rim3	mpc1 core1	mpc1 core2	mpc1 rim1	mpc1 rim2	mpc1 rim3	pc4 core1	pc4 core2	pc4 rim1	pc4 rim2	pc5 core	pc5 rim1	pc5 rim2	xx2 core	xx2 rim	xx1 core1	xx1 core2	xx1 rim	xx2 core1	xx2 core2	xx2 rim
Mn	0·005	0·005	0·011	0·030	0·021	0·016	0·006	0·046	0·038	0·049	0·004	0·027	0·100	0·058	0·002	0·025	0·039	0·010	0·008	0·007	0·012	0·012	0·002	0·000	0·000
Fe^{2+}	0·597	0·843	0·619	0·122	0·079	1·094	1·083	3·078	3·019	3·005	0·781	1·319	4·207	3·094	0·759	0·697	0·000	0·549	0·464	1·133	1·168	1·171	0·651	0·650	0·680
[M]	6·0	5·8	6·1	6·0	6·0	6·0	5·9	5·6	5·5	5·5	5·8	5·9	5·7	5·8	6·0	6·1	6·1	5·9	6·0	5·9	5·9	6·0	6·0	5·9	6·0
Ba	0·001	0·024	0·026	0·003	0·004	0·000	0·005	0·002	0·005	0·000	0·031	0·029	0·011	0·025	0·081	0·035	0·005	0·002	0·006	0·038	0·047	0·034	0·016	0·024	0·018
Na	0·103	0·111	0·093	0·022	0·040	0·242	0·251	0·129	0·157	0·151	0·135	0·141	0·034	0·052	0·128	0·121	0·078	0·013	0·021	0·285	0·304	0·292	0·274	0·264	0·209
K	1·858	1·763	1·773	1·914	1·917	1·631	1·671	1·694	1·743	1·775	1·719	1·725	1·834	1·749	1·708	1·727	1·809	1·898	1·909	1·600	1·600	1·582	1·587	1·648	1·628
[A]	2·0	1·9	1·9	1·9	2·0	1·9	1·9	1·8	1·9	1·9	1·9	1·9	1·9	1·8	1·9	1·9	1·9	1·9	1·9	1·9	2·0	1·9	1·9	1·9	1·9
Total cations	15·9	15·7	16·0	16·0	16·0	15·9	15·8	15·4	15·4	15·4	15·7	15·8	15·6	15·6	15·9	16·0	16·0	15·9	15·9	15·8	15·9	15·9	15·8	15·9	15·8
F	0·576	0·230	0·223	0·261	0·268	0·237	0·202	0·130	0·152	0·098	0·352	0·331	0·016	0·132	0·213	0·302	0·809	1·047	1·077	0·133	0·127	0·211	0·231	0·363	0·357
Cl	0·000	0·000	0·000	0·000	0·000	0·000	0·000	0·000	0·003	0·002	0·002	0·003	0·002	0·003	0·000	0·000	0·002	0·000	0·001	0·006	0·002	0·004	0·002	0·002	0·005
OH	3·424	3·770	3·777	3·739	3·732	3·763	3·798	3·870	3·845	3·901	3·646	3·666	3·983	3·865	3·787	3·698	3·190	2·953	2·922	3·861	3·870	3·785	3·768	3·635	3·639
Total	4·0	4·0	4·0	4·0	4·0	4·0	4·0	4·0	4·0	4·0	4·0	4·0	4·0	4·0	4·0	4·0	4·0	4·0	4·0	4·0	4·0	4·0	4·0	4·0	4·0
Mg-no.	89·8	84·2	89·6	98·0	98·7	80·7	80·6	36·3	37·3	37·0	85·0	75·7	15·9	40·0	86·0	88·2	100·0	90·6	92·1	79·5	78·9	79·2	88·3	88·3	87·8

Mg-number = 100[Mg/(Mg + Fe^{2+})] in atomic units; analyses recalculated on the basis of eight tetrahedral cations and 22 O equivalents; Phl, phlogopite; TFP, tetraferriphlogopite; Bt, biotite; pc, phenocryst; mpc, microphenocryst; xx, crystal. [T] tetrahedral site; [M] octahedral site; [A] interlayer.

Table 6: Representative clinopyroxene compositions from Aillik Bay area ultramafic lamprophyres, carbonatites and their cognate inclusions

Rock type:	ultramafic lamprophyres and carbonatites													cognate inclusions					
	aillikite		mela-aillikite				damtjernite				dol–cal carbonatite			cpx–phl nodule			ol–phl nodule		
Mineral:	Di	Di	Di	Di	Di	Di	Di	Di	Di	Aeg	Di	Di	Di	Di	Di	Di	Di	Di	Di
Sample no.:	L66	L66	ST244B	ST244B	ST244B	ST244B	ST224B	ST224B	ST246A	ST246A	ST199	ST199	ST199	L74py	L74py	L74py	ST162III	ST162III	ST162III
	mpc2	mpc2	mpc1	mpc1	mpc1	mpc1	gm1	gm1	mpc6	mpc6	pc12	pc12	pc12	xx1	xx1	xx1	xx4	xx4	xx4
	core	rim	core1	core2	rim1	rim2	core	rim	core	rim	core1	core2	rim	core	rim1	rim2	core1	core2	rim
SiO_2	51·47	53·44	48·83	48·09	44·35	43·06	49·26	45·92	50·20	49·60	47·93	46·10	48·71	50·55	49·95	46·68	53·55	53·78	53·48
TiO_2	0·87	0·46	2·78	3·05	4·96	5·41	2·94	5·03	2·40	2·98	2·43	3·17	2·30	2·07	2·21	2·42	0·49	0·36	0·46
Al_2O_3	1·63	0·20	2·98	3·29	5·85	6·77	3·02	5·03	2·28	1·31	4·45	5·95	4·05	1·69	2·41	5·37	1·05	0·83	0·97
Cr_2O_3	0·00	0·00	0·05	0·01	0·00	0·00	0·00	0·00	0·02	0·04	0·03	0·07	0·06	0·00	0·02	0·07	0·56	0·32	0·48
FeO	4·51	2·97	5·98	6·03	7·40	7·29	6·12	7·26	6·75	22·29	8·01	8·13	7·48	4·89	4·75	5·62	4·08	4·07	3·90
MnO	0·11	0·20	0·16	0·11	0·08	0·06	0·11	0·11	0·12	0·54	0·09	0·11	0·13	0·08	0·04	0·08	0·05	0·10	0·12
NiO	0·00	0·00	0·00	0·00	0·00	0·01	0·00	0·00	0·00	0·04	n.a.	n.a.	n.a.	0·00	0·03	0·00	n.a.	n.a.	n.a.
MgO	15·79	16·63	14·71	14·62	12·94	12·39	15·14	13·39	14·74	3·47	12·77	12·04	12·61	15·32	15·31	13·68	16·62	16·76	16·68
CaO	24·91	25·16	23·99	23·79	23·90	23·53	23·93	23·31	23·10	12·34	23·41	23·53	23·47	23·26	23·14	23·35	22·89	22·61	22·98
Na_2O	0·22	0·23	0·33	0·32	0·43	0·43	0·30	0·65	0·81	6·82	0·88	0·69	0·88	0·32	0·38	0·29	0·81	0·77	0·76
K_2O	0·01	0·00	0·00	0·00	0·03	0·00	0·00	0·00	0·02	0·04	0·00	0·00	0·00	0·00	0·02	0·00	0·01	0·02	0·00
Total	99·52	99·29	99·82	99·32	99·93	98·95	100·83	100·70	100·44	99·47	100·00	99·79	99·68	98·18	98·26	97·56	100·11	99·62	99·83
No. oxygens	6	6	6	6	6	6	6	6	6	6	6	6	6	6	6	6	6	6	6
Si	1·896	1·963	1·810	1·792	1·658	1·628	1·807	1·701	1·846	1·904	1·7813	1·7242	1·8162	1·896	1·870	1·768	1·948	1·965	1·951
Ti	0·024	0·013	0·078	0·086	0·139	0·154	0·081	0·140	0·066	0·086	0·0679	0·0892	0·0645	0·058	0·062	0·069	0·013	0·010	0·013
Al	0·071	0·009	0·130	0·145	0·258	0·302	0·131	0·220	0·099	0·059	0·1949	0·2623	0·1780	0·075	0·106	0·240	0·045	0·036	0·042
Cr	0·000	0·000	0·002	0·000	0·000	0·000	0·000	0·000	0·001	0·001	0·0010	0·0019	0·0016	0·000	0·001	0·002	0·016	0·009	0·014
Fe^{3+}*	0·105	0·055	0·116	0·123	0·180	0·165	0·115	0·146	0·134	0·469	0·1688	0·1591	0·1228	0·039	0·058	0·106	0·073	0·061	0·072
Fe^{2+}*	0·034	0·036	0·069	0·065	0·052	0·066	0·073	0·079	0·073	0·246	0·0801	0·0952	0·1105	0·115	0·091	0·072	0·051	0·064	0·047
Mn	0·003	0·006	0·005	0·004	0·003	0·002	0·004	0·003	0·004	0·017	0·0029	0·0036	0·0040	0·003	0·001	0·003	0·001	0·003	0·004
Ni	0·000	0·000	0·000	0·000	0·000	0·000	0·000	0·000	0·000	0·001	n.a.	n.a.	n.a.	0·000	0·001	0·000	n.a.	n.a.	n.a.
Mg	0·867	0·911	0·813	0·812	0·721	0·699	0·828	0·739	0·808	0·199	0·7075	0·6713	0·7009	0·857	0·854	0·772	0·901	0·913	0·907
Ca	0·983	0·990	0·953	0·950	0·957	0·953	0·941	0·925	0·910	0·507	0·9322	0·9430	0·9377	0·935	0·928	0·947	0·892	0·885	0·898
Na	0·016	0·016	0·024	0·023	0·031	0·031	0·022	0·047	0·058	0·508	0·0633	0·0502	0·0638	0·023	0·027	0·021	0·057	0·054	0·054
K	0·001	0·000	0·000	0·000	0·001	0·000	0·000	0·000	0·001	0·002	0·0000	0·0000	0·0000	0·000	0·001	0·000	0·001	0·001	0·000
Total cations	4·0	4·0	4·0	4·0	4·0	4·0	4·0	4·0	4·0	4·0	4·0	4·0	4·0	4·0	4·0	4·0	4·0	4·0	4·0
Al/Ti	2·9	0·7	1·7	1·7	1·8	2·0	1·6	1·6	1·5	0·7	2·9	2·9	2·8	1·3	1·7	3·5	3·4	3·6	3·3
Mg-no.	96·2	96·2	92·1	92·6	93·3	91·4	91·9	90·3	91·7	44·6	89·8	87·6	86·4	88·2	90·4	91·5	94·7	93·5	95·1

Mg-number = 100[Mg/(Mg + Fe^{2+})] in atomic units; Di, diopside; Aeg, aegirine; pc, phenocryst; mpc, microphenocryst; gm, groundmass; xx, crystal; n.a., not analyzed.
*Calculated assuming stoichiometry.

Table 7: Representative spinel compositions from Aillik Bay area ultramafic lamprophyres and their cognate inclusions

Rock type:	ultramafic lamprophyres														cognate inclusions							
	aillikite							mela-aillikite				damtjernite			glimmerite		cpx–phl nodule			ol–phl nodule		
Mineral:	Cr-Spl	Cr-Spl	Ti-Mag	Ti-Mag	Ti-Mag	Ti-Mag	Ti-Mag	Cr-Spl	Cr-Spl	Ti-Mag	Ti-Mag	Mag	Mag	Mag	Ti-Mag	Ti-Mag	Cr-Spl	Cr-Spl	Ti-Mag	Cr-Spl	Ti-Mag	Ti-Mag
Sample no.:	L60	L60	L60	L60	ST162II	ST162II	ST162II	ST251B	ST251B	ST251B	ST251B	ST211A	ST211A	ST211A	L74gl	L74gl	L74py	L74py	L74py	L6du	L6du	L6du
	mpc4	mpc4	mpc4	mpc4	pc1	pc1	pc1	mpc5	mpc5	mpc5	mpc5	mpc5	mpc5	mpc5	xx2	xx2	xx1	xx1	xx1	xx2	xx2	xx2
	core1	core2	rim1	rim2	core	rim1	rim2	core1	core2	rim1	rim2	core	rim1	rim2	core	rim	core1	core2	rim	core	rim1	rim2
SiO_2	0·12	0·12	0·09	0·08	0·10	0·08	0·11	0·12	0·13	0·12	0·10	1·42	0·88	0·18	0·06	0·15	0·00	0·01	0·01	0·00	0·03	0·06
TiO_2	8·88	15·95	20·84	11·10	3·84	12·33	8·78	6·63	6·51	16·52	15·62	3·68	4·63	2·65	8·57	8·44	8·50	8·58	10·16	9·80	16·29	19·95
Al_2O_3	7·35	5·67	4·42	9·05	6·68	7·00	3·19	9·37	8·99	2·82	2·29	0·67	0·23	0·04	0·26	1·00	0·59	0·55	0·50	4·35	4·03	3·48
Cr_2O_3	31·67	14·18	0·24	0·05	0·09	0·02	0·05	32·14	33·50	0·42	0·25	0·04	0·05	0·04	0·02	0·03	15·59	15·19	9·78	12·39	6·92	4·39
V_2O_3	0·17	0·12	0·02	0·02	0·00	0·00	0·00	0·17	0·18	0·15	0·21	0·22	0·20	0·27	0·19	0·21	0·40	0·40	0·42	0·46	0·20	0·21
FeO*	39·34	49·07	62·57	65·34	75·64	64·60	73·11	39·45	38·47	72·69	74·78	84·97	85·81	90·02	80·19	78·16	64·84	65·67	68·24	61·19	58·49	61·14
MnO	0·39	0·90	0·92	1·03	0·67	0·87	1·02	0·35	0·35	0·98	0·93	0·32	0·42	0·67	0·69	0·63	0·62	0·63	0·56	0·40	0·65	0·73
NiO	0·17	0·09	0·04	0·02	0·00	0·06	0·08	0·15	0·16	0·14	0·13	0·00	0·02	0·05	0·00	0·01	0·20	0·18	0·19	0·27	0·26	0·27
MgO	11·76	13·12	7·94	10·92	7·07	10·25	6·87	11·08	10·84	1·55	1·04	0·12	0·03	0·05	4·58	5·12	4·77	4·32	4·90	6·21	6·82	5·34
Total	99·85	99·22	97·08	97·61	94·08	95·20	93·20	99·46	99·13	95·38	95·35	91·44	92·28	93·97	94·56	93·75	95·51	95·53	94·75	95·07	93·68	95·56
No. oxygens	32	32	32	32	32	32	32	32	32	32	32	32	32	32	32	32	32	32	32	32	32	32
Si	0·031	0·032	0·024	0·021	0·029	0·022	0·032	0·030	0·035	0·036	0·031	0·445	0·274	0·056	0·017	0·043	0·000	0·003	0·003	0·000	0·009	0·018
Ti	1·751	3·145	4·366	2·203	0·811	2·529	1·903	1·306	1·291	3·711	3·529	0·866	1·085	0·610	1·899	1·871	1·877	1·901	2·256	2·115	3·564	4·353
Al	2·271	1·752	1·451	2·815	2·212	2·252	1·082	2·893	2·794	0·993	0·811	0·247	0·086	0·016	0·091	0·349	0·204	0·190	0·174	1·471	1·382	1·190
Cr	6·565	2·940	0·052	0·011	0·021	0·003	0·011	6·656	6·985	0·099	0·059	0·011	0·013	0·008	0·004	0·007	3·619	3·538	2·283	2·811	1·592	1·007
V	0·036	0·025	0·005	0·003	0·000	0·000	0·000	0·036	0·039	0·035	0·050	0·054	0·051	0·067	0·045	0·049	0·094	0·095	0·099	0·106	0·047	0·049
Fe^{3+}†	3·563	4·929	5·712	8·724	12·087	8·641	11·037	3·743	3·530	7·380	7·960	13·066	13·133	14·577	12·028	11·766	8·330	8·370	8·927	7·383	5·833	5·013
Fe^{2+}†	5·063	5·830	8·866	5·695	5·694	6·098	6·592	4·899	4·954	10·776	10·827	9·170	9·230	8·457	7·732	7·505	7·589	7·808	7·919	7·299	8·397	9·821
Mn	0·087	0·199	0·217	0·229	0·158	0·201	0·250	0·078	0·077	0·247	0·236	0·083	0·112	0·174	0·173	0·158	0·154	0·156	0·139	0·097	0·159	0·178
Ni	0·036	0·020	0·009	0·005	0·000	0·014	0·018	0·032	0·034	0·034	0·031	0·000	0·004	0·011	0·000	0·002	0·047	0·042	0·044	0·063	0·060	0·062
Mg	4·596	5·128	3·297	4·295	2·961	4·168	2·954	4·326	4·261	0·689	0·466	0·057	0·013	0·024	2·012	2·250	2·087	1·897	2·156	2·656	2·958	2·309
Total cations	24·0	24·0	24·0	24·0	24·0	23·9	23·9	24·0	24·0	24·0	24·0	24·0	24·0	24·0	24·0	24·0	24·0	24·0	24·0	24·0	24·0	24·0
Mg-no.	47·6	46·8	27·1	43·0	34·2	40·6	30·9	46·9	46·2	6·0	4·1	0·6	0·1	0·3	20·6	23·1	21·6	19·5	21·4	26·7	26·0	19·0

Mg-number = 100[Mg/(Mg + Fe^{2+})] in atomic units; Cr-Spl, chromian spinel; Ti-Mag, titanomagnetite; Mag, magnetite; mpc, microphenocryst; pc, phenocrocryst; xx, crystal.
*FeO as total Fe.
†Calculated assuming stoichiometry.

Table 8: Representative garnet compositions from the Aillik Bay area ultramafic lamprophyres

Rock type:	ultramafic lamprophyres																	
	aillikite								damtjernite									
Mineral:	Kim	Kim	Kim	Kim	Kim	Kim	Kim	Kim	Srl	Mlt	Mlt	Mlt	Zr-Srl	Srl	Mlt	Zr-Srl	Zr-Srl	Zr-Srl
Sample no.:	L60	L60	L66	L66	ST162II	ST162II	ST164	ST164	ST140A	ST140A	L70	L70	ST188A	ST188A	ST188A	ST188A	ST188A	ST188A
	gm4	gm4	gm2	gm2	gm1	gm1	gm8	gm8	gm2	gm2	gm4	gm4	gm3	gm3	gm3	gm4	gm4	gm4
	core	rim	core	rim	core1	core2	core	rim	core	rim	core	rim	core	rim1	rim2	core1	core2	rim
SiO_2	24·90	25·71	22·93	23·39	23·48	21·74	24·67	25·51	31·46	33·96	33·22	33·68	30·22	30·90	34·77	28·31	29·01	28·96
TiO_2	9·99	9·81	10·07	9·81	10·15	10·76	9·82	10·78	11·83	5·36	5·50	3·68	13·98	12·48	3·47	15·29	15·25	15·25
ZrO_2	14·98	13·69	16·51	15·92	16·06	17·17	14·83	12·51	0·40	0·15	0·30	0·31	1·11	0·60	0·05	4·93	3·86	2·99
HfO_2	0·31	0·27	0·36	0·27	0·28	0·28	0·25	0·17	0·00	0·00	0·04	0·03	0·12	0·12	0·03	0·16	0·13	0·13
Al_2O_3	2·14	1·47	3·26	2·55	2·58	2·96	2·22	1·53	1·39	2·21	1·89	2·02	0·53	0·63	1·71	0·29	0·29	0·28
Cr_2O_3	n.a.	n.a.	n.a.	n.a.	n.a.	n.a.	n.a.	n.a.	0·00	0·03	n.a.	n.a.	n.a.	n.a.	n.a.	n.a.	n.a.	n.a.
FeO	12·07	12·92	11·98	12·54	12·31	12·25	12·32	13·34	18·27	20·26	18·78	20·42	17·15	18·20	21·58	15·75	16·20	16·81
MnO	0·32	0·34	0·20	0·19	0·17	0·15	0·22	0·26	0·18	0·10	0·13	0·11	0·31	0·22	0·10	0·38	0·36	0·35
MgO	3·32	3·21	2·93	2·85	2·91	2·55	3·21	3·03	1·22	1·06	1·71	1·36	1·18	1·22	0·91	0·99	0·93	0·90
CaO	29·62	29·98	29·85	30·08	30·18	29·99	30·36	30·90	32·75	33·45	33·97	34·27	32·43	32·98	33·34	30·50	30·84	31·26
BaO	n.a.	n.a.	n.a.	n.a.	n.a.	n.a.	n.a.	n.a.	0·04	0·05	n.a.	n.a.	n.a.	n.a.	n.a.	n.a.	n.a.	n.a.
SrO	0·00	0·00	0·00	0·00	0·00	0·00	0·00	0·00	0·00	0·03	0·02	0·00	0·01	0·00	0·00	0·00	0·01	0·00
Na_2O	0·03	0·00	0·00	0·03	0·00	0·04	0·01	0·00	0·22	0·08	0·11	0·07	0·54	0·37	0·16	1·10	1·05	0·91
K_2O	n.a.	n.a.	n.a.	n.a.	n.a.	n.a.	n.a.	n.a.	0·00	0·02	n.a.	n.a.	n.a.	n.a.	n.a.	n.a.	n.a.	n.a.
Total	97·68	97·41	98·10	97·62	98·11	97·89	97·91	98·03	97·75	96·75	95·68	95·96	97·57	97·73	96·12	97·70	97·92	97·83
No. oxygens	12	12	12	12	12	12	12	12	12	12	12	12	12	12	12	12	12	12
Si	2·227	2·296	2·060	2·107	2·106	1·973	2·198	2·253	2·650	2·849	2·805	2·835	2·569	2·612	2·929	2·452	2·494	2·486
Al	0·226	0·154	0·345	0·271	0·273	0·317	0·233	0·160	0·138	0·151	0·188	0·165	0·053	0·063	0·071	0·030	0·029	0·029
Fe^{3+}	0·547	0·549	0·595	0·622	0·621	0·710	0·569	0·587	0·212	0·000	0·007	0·000	0·378	0·325	0·000	0·519	0·477	0·486
[T]	3·0	3·0	3·0	3·0	3·0	3·0	3·0	3·0	3·0	3·0	3·0	3·0	3·0	3·0	3·0	3·0	3·0	3·0
Al	0·000	0·000	0·000	0·000	0·000	0·000	0·000	0·000	0·000	0·068	0·000	0·035	0·000	0·000	0·099	0·000	0·000	0·000
Fe^{3+}	0·356	0·416	0·305	0·323	0·303	0·219	0·349	0·398	0·919	1·422	1·320	1·437	0·829	0·917	1·520	0·622	0·688	0·721
Ti	0·672	0·659	0·681	0·665	0·685	0·735	0·658	0·716	0·750	0·338	0·349	0·233	0·894	0·793	0·220	0·996	0·986	0·985
Fe^{2+}	0·000	0·000	0·000	0·000	0·000	0·000	0·000	0·000	0·156	0·000	0·000	0·000	0·013	0·044	0·000	0·000	0·000	0·000
Zr	0·653	0·596	0·723	0·699	0·703	0·760	0·644	0·539	0·017	0·006	0·012	0·013	0·046	0·025	0·002	0·208	0·162	0·125
Hf	0·008	0·007	0·009	0·007	0·007	0·007	0·006	0·004	0·000	0·000	0·001	0·001	0·003	0·003	0·001	0·004	0·003	0·003
Mg	0·281	0·296	0·266	0·287	0·290	0·261	0·324	0·323	0·109	0·132	0·215	0·171	0·104	0·141	0·115	0·000	0·000	0·000
Na	0·006	0·000	0·000	0·005	0·000	0·007	0·002	0·000	0·036	0·013	0·018	0·011	0·089	0·061	0·026	0·185	0·175	0·151
[Y]	2·0	2·0	2·0	2·0	2·0	2·0	2·0	2·0	2·0	2·0	1·9	1·9	2·0	2·0	2·0	2·0	2·0	2·0
Ca	2·839	2·869	2·873	2·904	2·901	2·916	2·898	2·924	2·956	3·007	3·074	3·091	2·954	2·987	3·010	2·830	2·841	2·875
Mg	0·161	0·131	0·127	0·096	0·099	0·084	0·102	0·076	0·044	0·000	0·000	0·000	0·046	0·013	0·000	0·127	0·119	0·115
Mn	0·000	0·000	0·000	0·000	0·000	0·000	0·000	0·000	0·000	0·000	0·000	0·000	0·000	0·000	0·000	0·000	0·000	0·000
[X]	3·0	3·0	3·0	3·0	3·0	3·0	3·0	3·0	3·0	3·0	3·1	3·1	3·0	3·0	3·0	3·0	3·0	3·0

Garnets recalculated on the basis of 12 oxygens following Munno *et al*. (1980); Kim, kimzeyite; Srl, schorlomite; Mlt, melanite; gm, groundmass. [T], tetrahedral site; [Y], octahedral site; [X], dodecahedral site; n.a., not analyzed.

amphibole occasionally replaces clinopyroxene and phlogopite (Figs 5g and 6f), presumably as a product of melt infiltration. Subhedral titanite occurs in a single nodule (ST250C).

Rare cumulate-textured olivine–phlogopite nodules contain irregular olivine grains (300–800 μm), which are typically enclosed by large phlogopite plates (0·5–1·0 mm; Fig. 5h). Hydroxy-fluorapatite

Table 9: Representative ilmenite compositions from Aillik Bay area ultramafic lamprophyres, carbonatites and their cognate inclusions

Rock type:	ultramafic lamprophyres and carbonatites													cognate inclusions									
	aillikite				mela-aillikite			damtjernite				dol–cal carbonatite		glimmerite			cpx–phl nodule					ol–phl nodule	
Mineral:	Ilm	Ilm	Ilm	Ilm	Ilm	Ilm	Ilm	Ilm	Ilm	Ilm	Ilm	Ilm	Ilm	Ilm	Ilm	Ilm	Ilm	Ilm	Ilm	Ilm	Ilm	Ilm	Ilm
Sample no.:	L54	L54	L65	L65	ST244B	ST244B	ST244B	ST206A	ST206A	ST211A	ST211A	L49cab	L49cab	L74gl	L74gl	L74gl	L74py	L74py	L74py	L54py	L54py	ST250B	ST250B
	mpc2	mpc2	mpc1	mpc1	mpc1	mpc1	mpc1	mpc4	mpc4	mpc6	mpc6	mpc1	mpc1	xx3	xx3	xx3	xx3	xx3	xx3	xx3	xx3	xx3	xx3
	core	rim	core	rim	core1	core2	core3	core	rim	core1	core2	core	rim	core	rim1	rim2	core1	core2	rim	core	rim	core	rim
SiO_2	0·05	0·02	0·03	0·25	0·16	0·24	0·07	0·07	0·07	0·25	0·19	0·13	0·11	0·04	0·01	0·07	0·04	0·02	0·06	0·01	0·03	0·04	3·36
TiO_2	50·08	46·84	50·94	51·38	51·62	50·78	51·74	51·42	51·63	50·42	50·83	50·85	52·41	47·56	44·00	44·49	51·60	51·09	46·72	48·62	45·58	52·08	46·78
Al_2O_3	0·17	0·16	0·34	0·01	0·01	0·04	0·00	0·01	0·01	0·04	0·02	0·02	0·00	0·03	0·12	0·10	0·04	0·04	0·12	0·00	0·08	0·66	0·03
Cr_2O_3	0·23	0·28	0·74	0·51	0·03	0·04	0·01	0·04	0·05	0·02	0·03	0·00	0·03	0·00	0·06	0·02	0·41	0·38	0·17	0·32	0·29	0·97	0·51
V_2O_3	0·15	0·12	0·13	0·00	n.a.	n.a.	n.a.	n.a.	n.a.	n.a.	n.a.	0·14	0·00	0·05	0·01	0·02	0·10	0·05	0·00	0·07	0·01	n.a.	n.a.
FeO*	36·10	46·03	33·17	39·19	46·25	47·04	46·26	43·50	42·13	43·53	44·54	41·96	41·63	43·92	47·29	47·25	32·60	35·11	45·48	38·46	46·71	32·38	41·79
MnO	0·65	2·03	0·66	3·77	1·18	1·17	1·12	3·37	4·42	4·16	4·38	3·97	3·96	2·08	1·82	2·18	0·65	0·75	1·18	0·98	1·86	0·41	1·68
NiO	0·00	0·01	0·05	0·03	0·00	0·03	0·01	0·01	0·03	0·00	0·00	0·00	0·01	0·00	0·00	0·00	0·10	0·06	0·03	0·05	0·02	0·06	0·00
MgO	10·59	1·51	11·66	2·45	1·37	1·18	1·17	0·00	0·03	0·06	0·03	0·25	0·19	3·73	1·48	0·65	12·15	10·59	4·08	8·61	1·20	12·06	2·95
Total	98·02	96·99	97·71	97·58	100·63	100·52	100·38	98·42	98·38	98·48	100·01	97·31	98·34	97·41	94·78	94·77	97·69	98·09	97·85	97·12	95·77	98·65	97·09
No. oxygens	6	6	6	6	6	6	6	6	6	6	6	6	6	6	6	6	6	6	6	6	6	6	6
Si	0·002	0·001	0·001	0·013	0·008	0·012	0·003	0·003	0·004	0·013	0·009	0·007	0·006	0·002	0·001	0·004	0·002	0·001	0·003	0·001	0·002	0·002	0·168
Ti	1·778	1·802	1·800	1·958	1·923	1·895	1·936	1·983	1·991	1·938	1·924	1·978	2·012	1·790	1·728	1·761	1·820	1·815	1·743	1·767	1·779	1·815	1·760
Al	0·010	0·009	0·019	0·001	0·001	0·002	0·000	0·001	0·001	0·003	0·001	0·001	0·000	0·002	0·007	0·006	0·002	0·002	0·007	0·000	0·005	0·036	0·002
Cr	0·009	0·011	0·027	0·020	0·001	0·002	0·000	0·002	0·002	0·001	0·001	0·000	0·001	0·000	0·002	0·001	0·015	0·014	0·007	0·012	0·012	0·035	0·020
V	0·005	0·005	0·005	0·000	n.a.	n.a.	n.a.	n.a.	n.a.	n.a.	n.a.	0·006	0·000	0·002	0·001	0·001	0·004	0·002	0·000	0·003	0·000	n.a.	n.a.
Fe^{3+}†	0·416	0·370	0·347	0·038	0·136	0·182	0·120	0·026	0·007	0·094	0·130	0·024	0·000	0·413	0·533	0·463	0·335	0·350	0·493	0·449	0·422	0·294	0·122
Fe^{2+}†	1·009	1·599	0·956	1·622	1·780	1·770	1·805	1·839	1·800	1·767	1·745	1·792	1·777	1·425	1·533	1·617	0·943	1·038	1·394	1·106	1·606	0·961	1·627
Mn	0·026	0·088	0·026	0·162	0·050	0·049	0·047	0·146	0·192	0·180	0·187	0·174	0·171	0·088	0·081	0·097	0·026	0·030	0·050	0·040	0·082	0·016	0·071
Ni	0·000	0·000	0·002	0·001	0·000	0·001	0·000	0·001	0·001	0·000	0·000	0·000	0·000	0·000	0·000	0·000	0·004	0·002	0·001	0·002	0·001	0·002	0·000
Mg	0·745	0·115	0·817	0·185	0·101	0·087	0·087	0·000	0·002	0·004	0·002	0·019	0·014	0·278	0·115	0·051	0·849	0·746	0·302	0·620	0·093	0·833	0·220
Total cations	4·0	4·0	4·0	4·0	4·0	4·0	4·0	4·0	4·0	4·0	4·0	4·0	4·0	4·0	4·0	4·0	4·0	4·0	4·0	4·0	4·0	4·0	4·0
Mg-no.	42·5	6·7	46·1	10·2	5·4	4·7	4·6	0·0	0·1	0·2	0·1	1·1	0·8	16·3	7·0	3·0	47·4	41·8	17·8	35·9	5·4	46·4	11·9

Mg-number = 100[Mg/(Mg + Fe^{2+})] in atomic units; Ilm, ilmenite; mpc, microphenocryst; xx, crystal; n.a., not analyzed.
*FeO as total Fe.
†Calculated assuming stoichiometry.

Table 10: Representative perovskite compositions from the Aillik Bay area ultramafic lamprophyres

Rock type:	aillikite													mela-aillikite		
Mineral:	Prv	Prv	Prv	Prv	Prv	Prv	Prv	Prv	Prv	Prv	Prv	Prv	Prv	Prv	Prv	Prv
Sample no.:	L2	L2	L2	L2	L2	L2	L6	L6	L6	L6	L51	L51	L51	ST147A	ST147A	ST147A
	mpc8	mpc8	mpc8	mpc1	mpc1	mpc1	gm8	gm8	gm1	gm1	gm1	gm1	gm1	gm1	gm1	gm1
	core	rim1	rim2	core1	core2	rim	core	rim	core	rim	core1	core2	rim	core	rim1	rim2
Nb_2O_5	0·5	0·4	0·4	0·3	0·3	0·2	0·4	0·8	0·4	0·3	0·3	0·3	0·5	0·1	0·2	0·2
SiO_2	0·0	0·0	0·0	0·0	0·0	0·0	0·0	0·0	0·0	0·0	0·0	0·0	0·0	0·0	0·0	0·0
TiO_2	55·4	56·0	55·9	56·3	56·3	56·1	54·6	54·2	54·5	54·8	55·9	55·7	54·5	56·5	56·6	56·5
Al_2O_3	0·2	0·2	0·2	0·3	0·3	0·2	0·1	0·2	0·2	0·2	0·2	0·2	0·2	0·2	0·2	0·2
La_2O_3	0·4	0·3	0·4	0·5	0·3	0·5	0·6	0·6	0·7	0·6	0·5	0·3	0·7	0·4	0·4	0·3
Ce_2O_3	1·1	1·0	0·9	1·4	1·2	1·4	2·1	1·5	2·3	1·8	1·3	0·9	1·6	1·0	1·0	0·9
Pr_2O_3	0·1	0·0	0·2	0·2	0·1	0·3	0·4	0·2	0·4	0·2	0·1	0·2	0·2	n.a.	n.a.	n.a.
Nd_2O_3	0·7	0·5	0·5	0·7	0·7	0·8	1·1	0·6	1·2	0·9	0·6	0·4	0·7	n.a.	n.a.	n.a.
Sm_2O_3	0·1	0·1	0·1	0·1	0·1	0·1	0·2	0·1	0·2	0·1	0·1	0·1	0·1	n.a.	n.a.	n.a.
Y_2O_3	0·0	0·0	0·0	0·0	0·0	0·1	0·1	0·1	0·1	0·1	0·0	0·0	0·0	0·0	0·0	0·0
FeO*	1·2	1·1	1·0	1·0	1·0	0·9	1·2	1·5	1·2	1·2	1·1	1·3	1·3	1·1	1·1	1·1
MgO	0·0	0·0	0·0	0·0	0·0	0·0	0·1	0·0	0·1	0·0	0·1	0·1	0·0	0·0	0·0	0·0
CaO	39·8	39·9	39·7	39·4	39·4	39·3	37·6	39·0	37·1	37·7	39·0	39·2	38·6	39·5	39·4	39·6
SrO	0·2	0·2	0·2	0·2	0·2	0·2	0·2	0·3	0·2	0·2	0·3	0·2	0·2	0·2	0·2	0·3
Na_2O	0·2	0·2	0·3	0·3	0·3	0·4	0·6	0·4	0·6	0·4	0·4	0·4	0·3	0·2	0·2	0·3
Total	99·99	100·03	99·76	100·80	100·24	100·55	99·31	99·34	99·01	98·56	99·75	99·21	98·98	99·37	99·37	99·35

Rock type:	damtjernite																
Mineral:	Prv	Prv	Prv	Prv	Prv	Prv	Prv	Prv	Prv	Prv	Prv	Prv	Prv	Prv	Prv	Prv	Prv
Sample no.:	ST140A	ST140A	ST140A	ST140A	ST140A	ST140A	ST140A	ST140A	ST140A	ST188A	ST188A	ST188A	ST211A	ST211A	ST211A	ST211A
	mpc1	mpc1	mpc1	mpc1	mpc1	mpc2	mpc2	mpc2	mpc2	mpc1	mpc1	mpc1	mpc1	mpc1	mpc1	mpc1
	core1	core2	core3	rim1	rim2	core	rim1	rim2	rim3	core	rim1	rim2	core1	core2	rim1	rim2
Nb_2O_5	0·4	0·4	0·5	0·6	0·7	0·5	0·6	0·6	0·5	0·5	0·6	1·3	0·3	0·3	0·3	0·4
SiO_2	0·0	0·0	0·0	0·0	0·0	0·1	0·0	0·0	0·0	0·0	0·0	0·0	0·0	0·0	0·0	0·0
TiO_2	55·3	55·4	55·7	55·5	55·9	54·9	55·9	55·0	55·2	55·7	55·4	56·3	55·1	55·2	55·4	54·9
Al_2O_3	0·2	0·2	0·2	0·1	0·2	0·2	0·1	0·1	0·1	0·2	0·2	0·1	0·1	0·2	0·2	0·2
La_2O_3	0·6	0·6	0·6	0·5	0·5	0·5	0·4	0·5	0·4	0·8	0·8	0·5	1·0	0·8	0·7	0·9
Ce_2O_3	1·5	1·4	1·3	0·7	0·6	1·1	0·8	0·8	0·8	2·2	1·8	0·6	2·8	2·8	2·4	2·9
Pr_2O_3	0·2	0·1	0·2	0·1	0·1	0·1	0·1	0·1	0·1	n.a.	n.a.	n.a.	n.a.	n.a.	n.a.	n.a.
Nd_2O_3	0·6	0·7	0·6	0·3	0·3	0·5	0·3	0·3	0·4	n.a.	n.a.	n.a.	n.a.	n.a.	n.a.	n.a.
Sm_2O_3	0·1	0·1	0·1	0·1	0·0	0·1	0·1	0·1	0·1	n.a.	n.a.	n.a.	n.a.	n.a.	n.a.	n.a.
Y_2O_3	0·1	0·1	0·1	0·0	0·0	0·0	0·1	0·0	0·0	0·1	0·1	0·1	0·1	0·0	0·1	0·0
FeO*	1·1	1·1	1·0	1·1	1·2	1·5	1·2	1·1	1·2	1·1	1·3	0·8	1·1	1·1	1·1	1·1
MgO	0·0	0·0	0·0	0·0	0·0	0·0	0·0	0·0	0·0	0·0	0·0	0·0	0·0	0·0	0·0	0·0
CaO	38·9	38·6	39·0	39·8	39·9	39·4	40·0	39·4	39·9	37·2	37·7	38·7	36·0	36·1	36·6	36·0
SrO	0·3	0·3	0·3	0·4	0·5	0·4	0·4	0·5	0·4	0·4	0·4	0·7	0·3	0·3	0·3	0·3
Na_2O	0·5	0·5	0·6	0·4	0·3	0·5	0·4	0·4	0·4	0·7	0·7	0·8	0·8	0·8	0·8	0·8
Total	99·86	99·51	100·17	99·61	100·08	99·78	100·35	98·87	99·55	98·72	99·11	99·82	97·59	97·53	97·87	97·43

All analyses by electron microprobe; n.a., not analyzed.
*FeO as total Fe.

Table 11: Representative nepheline, sodalite, alkali feldspar and pectolite compositions of damtjernites from the Aillik Bay area

Mineral:	Ne	Sdl	Sdl	Ne	Ne	Sdl	Ab	Ab	Or	Or	Or	Or	Ab	Pct	Pct	Pct	Pct	Pct	Pct
Sample no.:	ST188B	ST188B	ST188B	ST211C	ST211C	ST211C	ST246A	ST246A	ST246A	ST246A	ST206A	ST206A	ST206A	ST174	ST174	ST188A	ST188A	ST256	ST256
	gm3	gm3	gm3	gm1	gm1	gm1	gm2	gm2	gm2	gm2	seg4	seg4	seg4	gm8	gm8	gm3	gm3	gm1	gm1
	core	rim1	rim2	core	rim1	rim2	core1	core2	core3	core4	core1	core2	core3	core1	core2	core1	core2	core	rim
SiO_2	41·12	37·15	37·07	41·21	42·14	37·58	68·37	68·25	63·69	64·27	64·06	63·23	67·81	52·58	52·78	52·73	52·55	53·17	53·04
TiO_2	0·00	0·00	0·01	0·02	0·03	0·03	0·00	0·00	0·01	0·04	0·02	0·06	0·03	0·20	0·21	0·06	0·08	0·11	0·20
Al_2O_3	34·41	33·35	33·76	33·08	32·95	36·36	19·43	19·50	18·55	18·28	18·26	18·21	19·75	0·02	0·03	0·25	0·34	0·07	0·10
Cr_2O_3	0·00	0·03	0·03	0·06	0·02	0·04	0·04	0·07	0·01	0·03	0·01	0·03	0·05	0·04	0·01	0·06	0·03	0·01	0·00
FeO	1·40	0·11	0·05	1·08	1·36	0·67	0·23	0·29	0·23	0·22	0·11	0·09	0·14	0·52	0·40	0·10	0·21	0·56	1·58
MnO	0·00	0·01	0·00	0·00	0·00	0·00	0·00	0·00	0·00	0·04	0·04	0·00	0·05	0·34	0·32	0·32	0·16	0·30	0·89
MgO	0·03	0·03	0·03	0·04	0·04	0·00	0·01	0·02	0·00	0·01	0·01	0·00	0·02	0·14	0·12	0·08	0·02	0·12	0·13
CaO	0·15	0·04	0·04	0·22	0·10	0·46	0·03	0·04	0·00	0·01	0·07	0·37	0·18	32·45	32·60	32·92	33·21	32·77	29·91
BaO	0·10	0·02	0·00	0·03	0·00	0·00	0·01	0·06	0·10	0·04	0·84	0·93	0·00	0·07	0·14	0·21	0·03	0·00	0·07
Na_2O	15·88	23·07	23·27	16·14	16·28	18·99	12·05	12·00	0·21	0·21	0·29	0·26	11·51	9·33	9·28	9·16	9·09	8·83	9·13
K_2O	7·36	0·06	0·01	6·68	6·71	0·00	0·03	0·05	16·60	16·75	15·87	16·16	0·01	0·00	0·00	0·00	0·00	0·00	0·01
F	0·09	0·00	0·00	0·00	0·01	0·00	n.a.	n.a.	n.a.	n.a.	n.a.	n.a.	n.a.	n.a.	n.a.	n.a.	n.a.	n.a.	n.a.
Cl	0·00	7·40	7·42	0·01	0·01	6·30	n.a.	n.a.	n.a.	n.a.	n.a.	n.a.	n.a.	n.a.	n.a.	n.a.	n.a.	n.a.	n.a.
O = Cl	0·00	−1·67	−1·67	0·00	0·00	−1·42	n.a.	n.a.	n.a.	n.a.	n.a.	n.a.	n.a.	n.a.	n.a.	n.a.	n.a.	n.a.	n.a.
Total	100·54	99·60	100·03	98·56	99·65	99·01	100·20	100·28	99·39	99·90	99·58	99·33	99·54	95·68	95·90	95·88	95·71	95·94	95·06

Ne, nepheline; Sdl, sodalite; Ab, albite; Or, orthoclase; Pct, pectolite; gm, groundmass; seg, segregation; n.a., not analyzed.

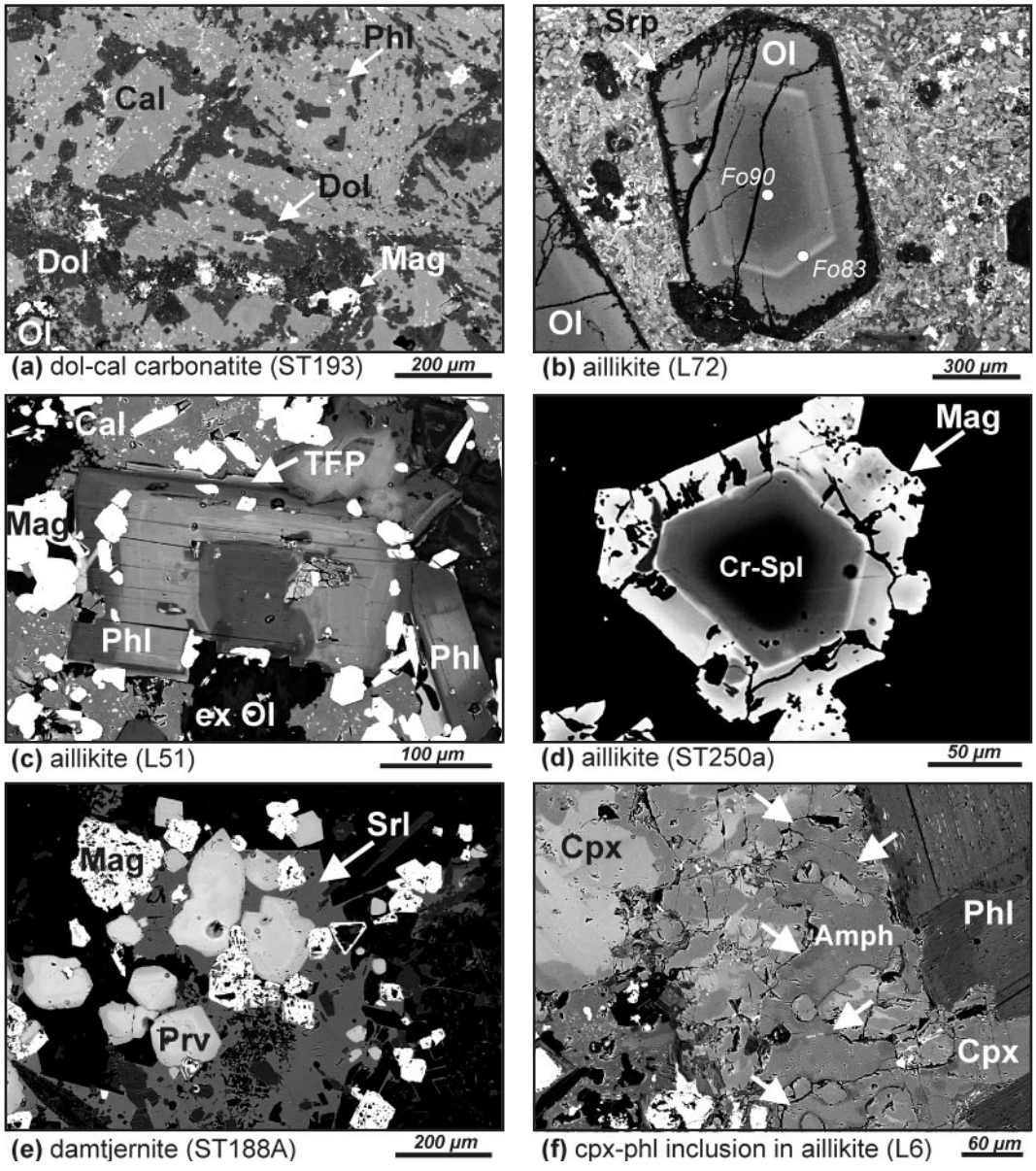

Fig. 6. Backscattered electron images of Aillik Bay area UML, carbonatite and a cognate inclusion. (a) Carbonatite mainly composed of coexisting calcite (Cal, light grey) and ferroan dolomite laths (Dol, dark grey). (b) Euhedral olivine phenocryst set in aillikite matrix. Zonation is normal from a forsterite content of 90 mol % (core) toward 83 mol % (rim), but the repetition of the zoning pattern and incipient serpentinization (Srp) should be noted. (c) Phlogopite microphenocryst in aillikite exhibiting core, inner mantle and broad rim with narrow tetraferriphlogopite overgrowth (TFP, arrow). (d) Zoned euhedral Cr-spinel microphenocryst in aillikite with titanomagnetite overgrowth. (e) Damtjernite groundmass assemblage consisting of euhedral schorlomite garnet (Srl, dark grey, arrow), which poikilitically encloses zoned perovskite (Prv, light grey) and magnetite grains (Mag, white). The atoll-textured magnetite grain should be noted. (f) Calcic amphibole (arrows) infiltrating a cognate inclusion that is mainly composed of zoned clinopyroxene prisms (Cpx) and phlogopite plates (Phl). The cognate inclusion was sampled by aillikite magma.

(200–400 μm), titanomagnetite, ilmenite (200–800 μm) and rare clinopyroxene (<300 μm) occur as intercumulus phases. Perovskite and zirconolite (<100 μm) are rare accessories associated with titanomagnetite surrounding olivine grains.

MINERAL COMPOSITIONS

Olivine

Aillikite/mela-aillikite olivine phenocrysts or microphenocrysts exhibit a fairly large range in forsterite component ($Fo_{91–80}$ mol %; Figs 6b and 7, and Table 4),

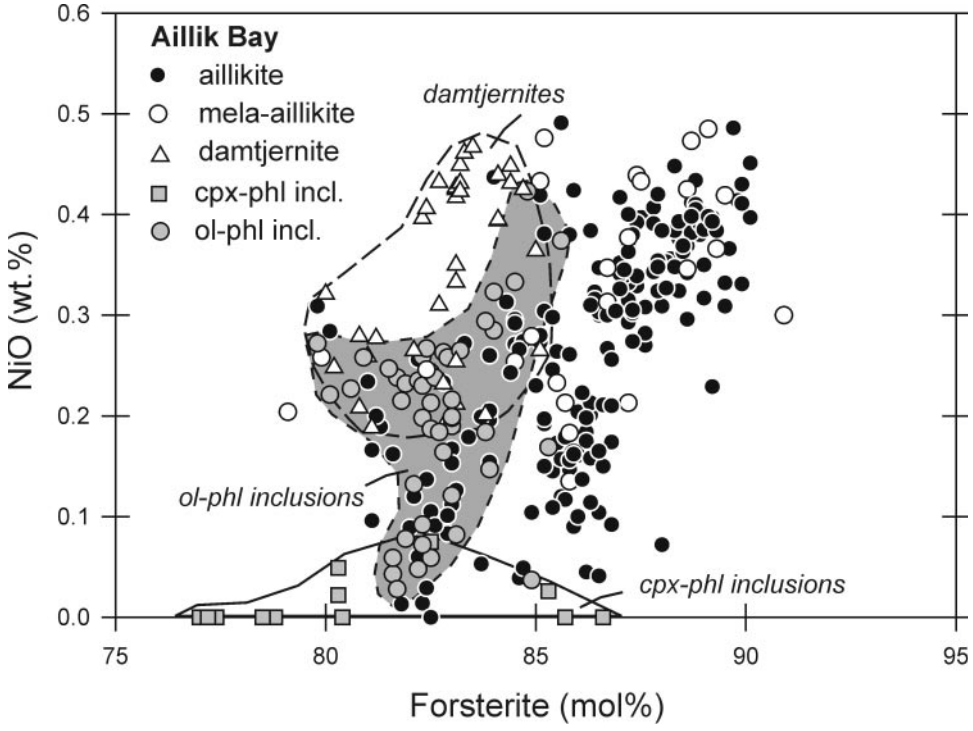

Fig. 7. NiO (wt %) vs forsterite (mol %) variation in olivine phenocrysts or microphenocrysts in ultramafic lamprophyres and their cognate micaceous inclusions from the Aillik Bay area. Outlines and grey-shaded field indicate olivine compositions of distinct rock types.

NiO (0·5–0·05 wt %), CaO and MnO (maxima of 0·9 and 0·4 wt %, respectively). Contrasting Mg/Fe evolutionary trends may indicate that different olivine populations are present. Olivine phenocrysts with normal zoning have core compositions of $Fo_{87–91}$, decreasing to $Fo_{82–85}$ towards the rim; NiO decreases, whereas CaO and MnO typically increase (0·1–0·3 wt %). Repetition of a normal zoning pattern may occur (Fig. 6b). Reverse zoning was often observed, with core compositions of $Fo_{82–84}$ (NiO 0·2–0·3 wt %) steadily increasing towards the rim ($Fo_{87–88}$; NiO 0·4 wt %). A discrete Fe-enriched overgrowth (Fo_{82}; NiO 0·1 wt %) with sharp contact to the inner phenocryst usually occurs on reverse-zoned crystals, and can be strongly CaO enriched (up to 0·9 wt %).

Olivine phenocrysts in damtjernites are normal zoned ($Fo_{80–86·5}$) and contain 0·18–0·5 wt % NiO (Fig. 7). CaO and MnO approach 0·4 wt % at the rims. The most primitive olivine cores in damtjernites are more evolved than their most primitive counterparts from aillikite/mela-aillikite (Fo_{91}) but have similar high NiO concentrations (Fig. 7).

Rare subhedral olivine crystals in clinopyroxene–phlogopite nodules are normally zoned with a fairly evolved composition ($Fo_{77–86·6}$; <0·1 wt % NiO; <0·4 wt % CaO; Fig. 7) and a conspicuously high MnO content (0·3–0·7 wt %). The olivine compositions ($Fo_{80–86}$) in olivine–phlogopite nodules overlap with the low Mg/Fe end of aillikite phenocrysts, but are richer in NiO (up to 0·4 wt %) at a given Fo content (Fig. 7).

In general, olivine phenocryst compositions in UML and associated cognate inclusions from the Aillik Bay area are less primitive (<Fo_{91}) than those found in kimberlites and lamproites, which typically approach Fo_{93} (Mitchell, 1986; Mitchell & Bergman, 1991; Fedortchouk & Canil, 2004; Prelevic *et al.*, 2005).

Phlogopite

Phlogopite phenocrysts from aillikite and dolomite–calcite carbonatite typically have (1) a resorbed core with 15–16 wt % Al_2O_3 and up to 5 wt % TiO_2, (2) a broad inner rim with elevated Al_2O_3 (up to 18 wt %) and lower TiO_2 (about 2 wt %) and (3) a narrow outer rim with Al_2O_3 and TiO_2 falling below 10 and 1 wt %, respectively, at constantly high MgO. This trend may culminate in virtually Al- and Ti-free tetraferriphlogopite rims in the most carbonate-rich samples (Figs 6c and 8a; Table 5). Whereas tetraferriphlogopite is uncommon in kimberlites, the rims reported here are similar to those from orangeites but distinct from titanian tetraferriphlogopites in lamproites. Phlogopite from type

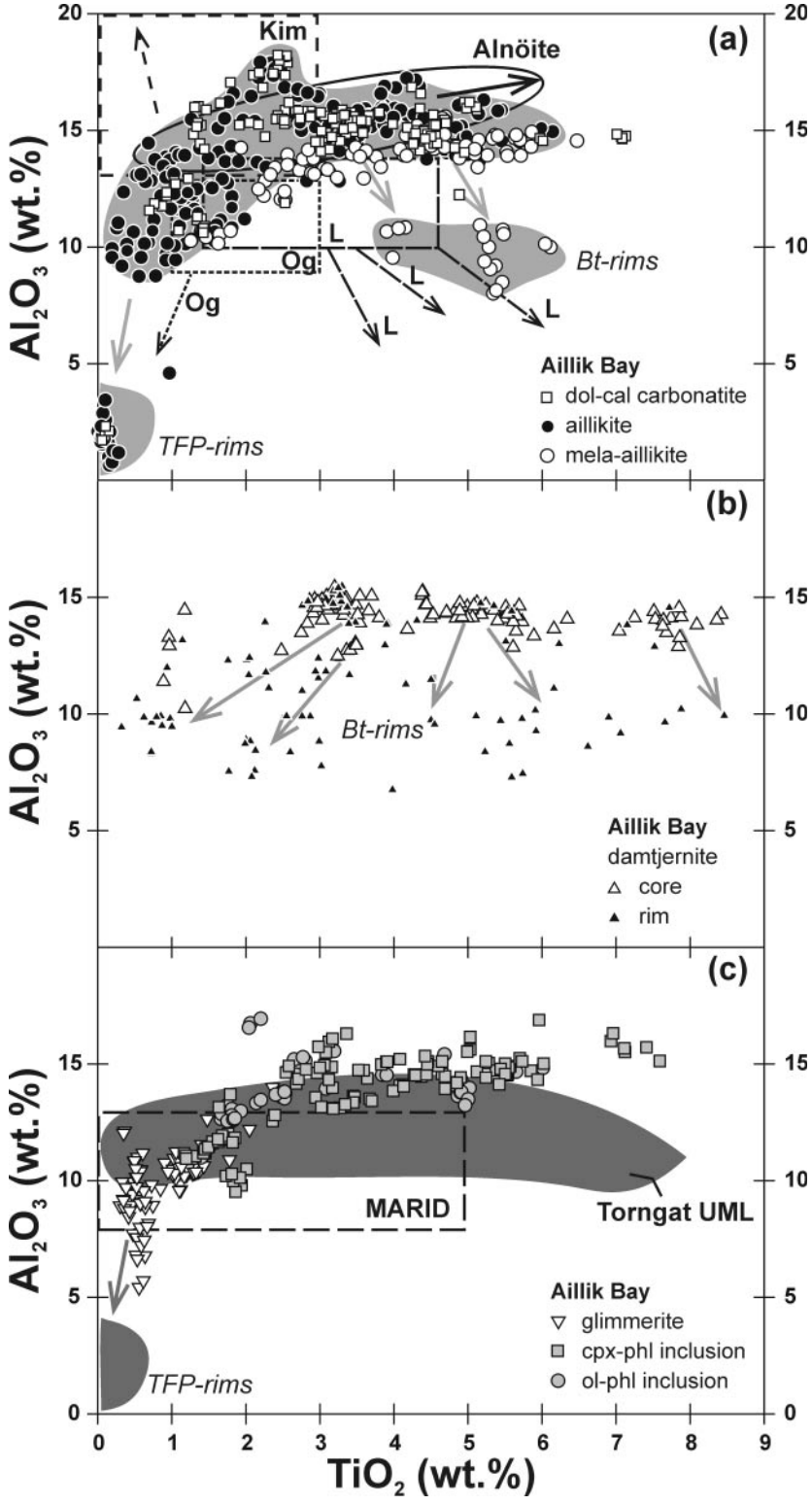

Fig. 8. Al_2O_3 vs TiO_2 (wt %) variation of micas in carbonatites and ultramafic lamprophyres (a, b), and their cognate inclusions (c) from the Aillik Bay area. (a) Pale grey fields and grey arrows indicate Aillik Bay UML mica compositional range and typical zoning trends. Kimberlite (Kim), orangeite (Og), lamproite (L) and alnöite mica compositional fields (black outlines) and evolutionary trends (black arrows) are after Mitchell (1995). (c) MARID (mica–amphibole–rutile–ilmenite–diopside) suite nodules compositional field after Dawson & Smith (1977) and Smith *et al.* (1978). Dark grey field for Torngat UML (aillikite and mela-aillikite) is from Tappe *et al.* (2004). Bt, biotite; TFP, tetraferriphlogopite.

aillikite/mela-aillikite and carbonatite is generally Ba poor with core compositions typically below 1 wt % BaO. Rim compositions only rarely approach 3 wt % BaO. This is in contrast to kimberlite phlogopites, which commonly show a strong Al and Ba enrichment and Ti depletion toward the rim (Fig. 8a). The inner zones of less extremely zoned phlogopite plates (0·5–1·0 mm) from mela-aillikite contain 13–15 wt % Al_2O_3 and 3–5 wt % TiO_2, but a high-Al inner rim composition such as in aillikite is absent. As in aillikites, Al_2O_3 depletion (8–13 wt %) toward the rim is common, but TiO_2 increases rimwards (up to 6 wt %; Fig. 8a), which contrasts with the decreasing TiO_2 trend observed in aillikites. Furthermore, micas from mela-aillikite follow a different Mg/Fe evolutionary trend than aillikite micas, with a strong increase in Fe at the expense of Mg leading to discrete dark brown biotite rims.

Damtjernite phlogopite plates compositionally resemble the less extremely zoned Ba-poor phlogopite plates from mela-aillikites with inner zones containing 13–15 wt % Al_2O_3 and 3–5 wt % TiO_2 (Fig. 8b). A few samples were found to contain micas approaching 8 wt % TiO_2 in the core. In general, these micas lack the high-Al inner rim composition of aillikite micas, but show Al depletion toward the rim (8–13 wt % Al_2O_3; Fig. 8b). We noted both rimward TiO_2 increase (up to 8·5 wt % as in mela-aillikite) and decrease (down to 1 wt % as in aillikite). Micas in damtjernite show a strong Fe increase at the expense of Mg. This culminates in broad dark brown biotite overgrowths (Fig. 5d).

The mica compositional range in the clinopyroxene–phlogopite and olivine–phlogopite nodules (Fig. 8c) is the same as in phenocrysts from aillikites/mela-aillikites and damtjernites with the characteristically high Al_2O_3 (13–15 wt %) and TiO_2 (1–8 wt %), but low BaO concentrations (<1·0 wt %). Fluorine concentrations are as low as in UML micas (<1·3 wt %), but much lower than in glimmerite phlogopite. The phlogopite plates are distinct from primitive mica compositions reported for MARID nodules (typically <12 wt % Al_2O_3, Dawson & Smith, 1977; Smith *et al.*, 1978) and do not show evolution toward either tetraferriphlogopite or biotite.

Glimmerite phlogopites are compositionally unlike any of the phlogopite phenocrysts, plates or groundmass flakes described above (Table 5). They are highly magnesian (Mg-number 70–90), Al_2O_3 and TiO_2 poor (5–12 and 0·3–2·0 wt %, respectively; Fig. 8c), BaO depleted (<0·2 wt %) but enriched in F (1–3 wt %).

Clinopyroxene and amphibole

Phenocrystic clinopyroxene in dolomite–calcite carbonatite and damtjernite, as well as groundmass prisms in damtjernites and mela-aillikites, are diopside-rich, showing Al_2O_3 and TiO_2 enrichment towards the rim (up to 10 and 6 wt %, respectively). However, the average atomic Al/Ti ratio of carbonatite clinopyroxene is ~3, distinctively higher than in clinopyroxene from associated mela-aillikite and damtjernite (~2; Fig. 9a; Table 6). Cr_2O_3 concentrations in all these diopsides are below 0·1 wt %. Aegirine-rich overgrowths (up to 46 mol %) occur around diopside-rich phenocrysts in damtjernite. Some of these phenocrysts contain rare resorbed green Fe-rich salitic clinopyroxene cores that are rich in Al_2O_3 (up to 9 wt %).

Clinopyroxene–phlogopite nodules also contain diopside-rich clinopyroxene enriched in Al_2O_3 and TiO_2 (up to 8 and 4 wt %, respectively), with atomic Al/Ti of ~2·5 similar to the UML clinopyroxenes (Fig. 9b). Slightly FeO- and Na_2O-enriched salitic core compositions (up to 9 and 3 wt %, respectively) may occur with Cr_2O_3 below 0·3 wt %. Olivine–phlogopite nodules carry rare diopside (4 and 2 wt % Al_2O_3 and TiO_2, respectively), which is the most Cr_2O_3-rich composition (0·1–0·6 wt %) of all the clinopyroxenes from the Aillik Bay UML suite. In general, the strong Al and Ti enrichment in clinopyroxene from the Aillik Bay UML and their cognate inclusions contrasts with diopsidic compositions typical for groundmass clinopyroxene in orangeites, lamproites and associated MARID-type inclusions (Mitchell & Bergman, 1991; Mitchell, 1995).

The intercumulus calcic amphibole found in the clinopyroxene–phlogopite nodules (Fig. 6f) is generally MgO and TiO_2 rich (Mg-number 73–90 and 1·9–5·0 wt % TiO_2) and ranges from magnesiohastingsite through pargasite to rare magnesiokatophorite. Fluorine is <0·5 wt % and K_2O does not exceed 1·9 wt %.

Spinel group

Spinel group minerals from Aillik Bay UMLs and related micaceous inclusions generally follow a 'titanomagnetite trend' (trend 2 of Mitchell, 1986) which is characterized by $Fe^{2+}_T/(Fe^{2+}_T + Mg) > 0·7$, increasing Fe and Ti but decreasing Mg, Al and Cr (Fig. 10). The most Mg-rich spinels were found in aillikites but do not exceed 13·5 wt % MgO (Table 7). By comparison, kimberlite spinels are more magnesian (12–20 wt % MgO) and follow a trend of increasing Ti at buffered Fe/Mg of ~0·5 (Fig. 10b; trend 1 of Mitchell, 1986). Aillik Bay UML spinels have Cr/(Cr + Al) ratios <0·85, which is in marked distinction to Cr-rich spinels in lamproites and orangeites (Cr-number >0·85), which follow the 'titanomagnetite trend' (Mitchell & Bergman, 1991; Mitchell, 1995).

Early-stage spinels in aillikites are typically composed of chromite–spinel solid solutions (up to 43 wt % Cr_2O_3, 13 wt % MgO, 12 wt % Al_2O_3). Rims of zoned spinel microphenocrysts and individual grains are of ulvöspinel–magnesian ulvöspinel–magnetite composition

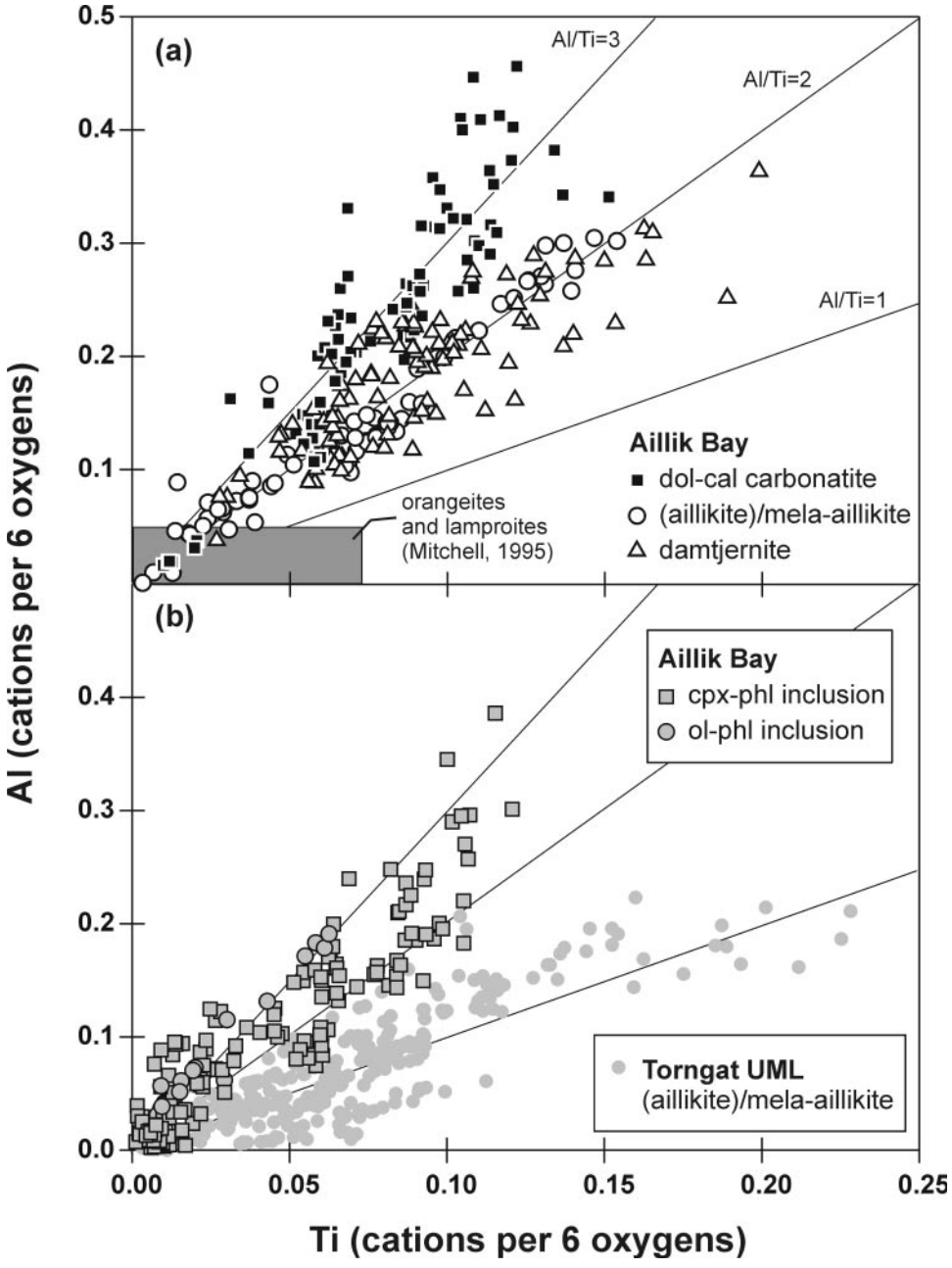

Fig. 9. Al vs Ti (cations per six oxygens) in diopside-rich clinopyroxenes from (a) carbonatites and ultramafic lamprophyres, and (b) their cognate inclusions from the Aillik Bay area. The Al and Ti enrichment of the UML clinopyroxene is in marked distinction to the almost pure diopside compositions characteristic of clinopyroxene in orangeites and lamproites (Mitchell, 1995). Data for Torngat UML are from Tappe *et al.* (2004). Lines indicate fixed Al/Ti ratios (see labels).

(up to 11 wt % MgO). The titanomagnetites are enriched in Al_2O_3 (up to 11 wt %) with low atomic Cr/(Cr + Al) ratios (<0·3). Spinels from mela-aillikites may contain cores of titanian magnesiochromite–chromite solid solution (up to 12 wt % TiO_2, 9 wt % MgO, 25 wt % Cr_2O_3) and of chromite–spinel solid solution, similar to their aillikite analogues. Individual titanomagnetite microphenocrysts or rims around zoned chromite grains contain less MgO and Al_2O_3 (<5 wt %) than in the aillikites (Fig. 10a).

Spinels in damtjernites are dominantly titanomagnetite, which rarely exhibits cores of titanian magnesiochromite–chromite solid solution (up to 14 wt % TiO_2, 9 wt % MgO, 22 wt % Cr_2O_3). Titanomagnetite in damtjernites has the lowest MgO concentration (typically <1 wt %) of all the Aillik Bay UML

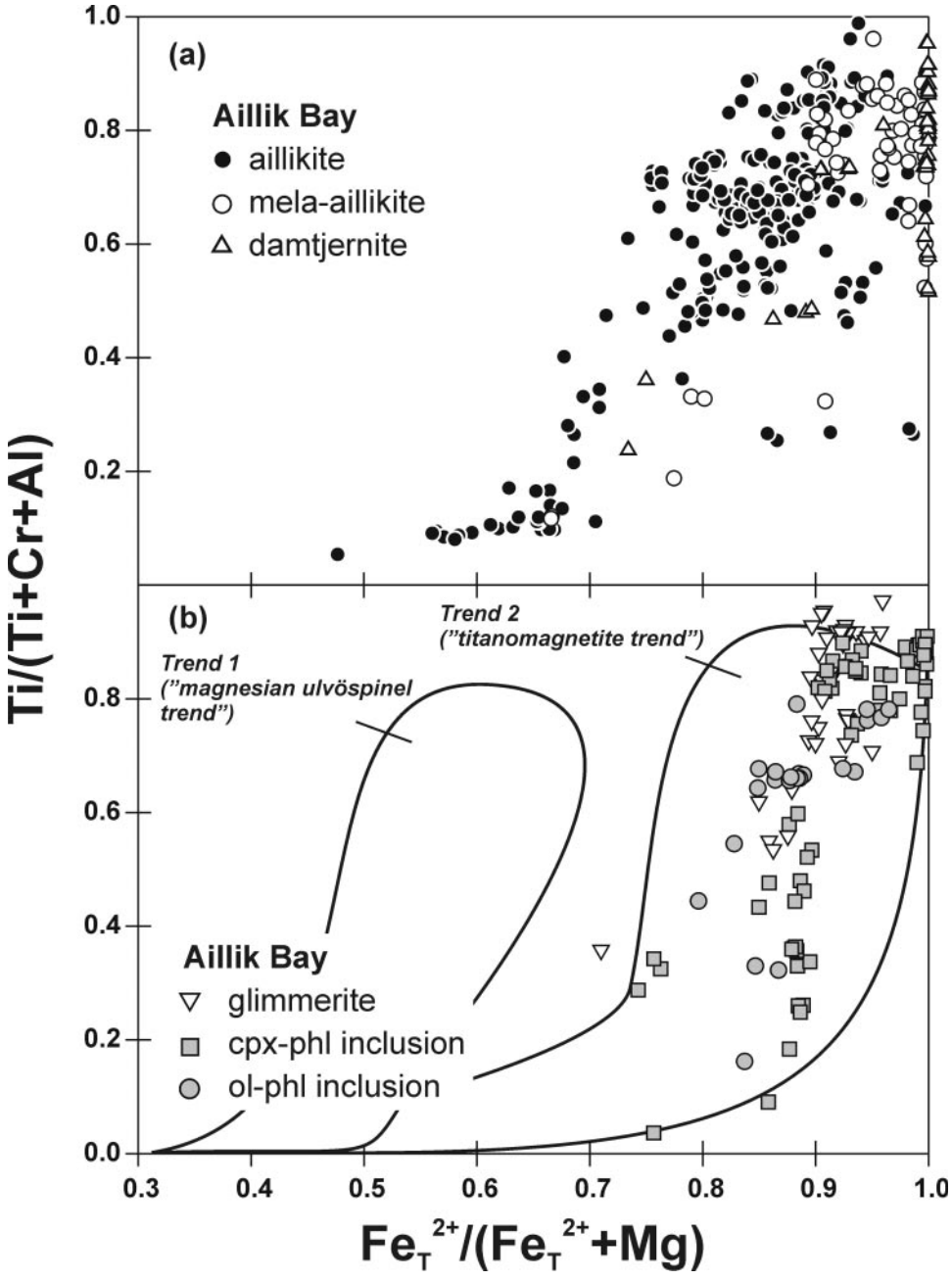

Fig. 10. Atomic Ti/(Ti + Cr + Al) vs $Fe_T^{2+}/(Fe_T^{2+} + Mg)$ for spinels in (a) ultramafic lamprophyres and (b) their cognate inclusions from the Aillik Bay area. Spinels in UML dykes follow magmatic trend 2 ('titanomagnetite trend'), in contrast to kimberlite spinel compositions, which are rich in magnesian ulvöspinel component (magmatic trend 1 of Mitchell, 1986).

spinels (Fig. 10a), and contains similar levels of Al_2O_3 to mela-aillikites, but significantly less Al_2O_3 than the aillikites. Individual grains have rims approaching magnetite end-member composition.

Rare spinels in glimmerites are similar to the most evolved aillikite spinels with MgO and Al_2O_3 typically below 5 wt % following a 'titanomagnetite trend' (Fig. 10b). Composite spinel grains in clinopyroxene–phlogopite nodules may contain cores of chromite (up to 43 wt % Cr_2O_3) and/or Cr-spinel (up to 20 wt % Cr_2O_3) typically mantled by titanomagnetite. Titanomagnetite–magnetite resembles late-stage spinels from pyroxene-rich mela-aillikites in being very close to magnetite end-member composition. They are much more depleted in MgO and Al_2O_3 (typically <2·0 and 3·0 wt %, respectively) than their analogues from

pyroxene-free glimmerites and aillikites (Fig. 10b). Titanomagnetite in olivine–phlogopite nodules resembles evolved aillikite spinels. They contain more MgO than spinels from clinopyroxene-rich nodules and mela-aillikite dykes (up to 7 wt %; Fig. 10b). Cr-spinel with up to 25 wt % Cr_2O_3 rarely occurs as inclusion in olivine.

Carbonate and Ti-rich primary garnet

Fe-rich dolomite crystals in dolomite carbonatite contain between 2 and 9 wt % FeO; only rarely approaching 12 wt % towards the rim. MnO is elevated (0·2–1·2 wt %), whereas SrO and BaO are conspicuously low (<0·2 wt %). Rare interstitial REE-carbonate is probably bastnäsite and contains up to 56 wt % $LREE_2O_3$ (where LREE is light rare earth element). Calcite in mixed dolomite–calcite carbonatite coexists with subordinate laths of Fe-rich dolomite (Fig. 6a) which resembles its counterpart from the dolomite carbonatites (2–12 wt % FeO and 0·2–1·2 wt % MnO). It differs in that both calcite and dolomite contain up to 1·5 wt % SrO. The groundmass of aillikites is dominated by a mosaic of Sr-calcite (up to 2 wt % SrO), whereas dolomite containing up to 10 wt % FeO is rare. Fe-rich dolomite seems to dominate over calcite (<1 wt % SrO) in the generally carbonate-poor groundmass of mela-aillikites. Carbonate in the damtjernite groundmass is Sr-calcite with up to 4·8 wt % SrO.

Small kimzeyitic garnets (Zr-rich andradite) are restricted to aillikites and have a fairly constant TiO_2 content (9–11 wt %), whereas ZrO_2 spans a wide range between 10 and 17 wt % (Table 8). Core compositions are generally richer in Zr than the rims. Schorlomite and/or melanite garnet is rare but characteristic for damtjernites, and observed zoning patterns are typically from Ti-rich core compositions to more Fe-rich rims (1·8–18 wt % TiO_2; 15·7–21·6 wt % FeO). Zirconian schorlomite with up to 5 wt % ZrO_2 in the core was rarely found. The presence of Ti-rich andradites and kimzeyitic garnets reflects the high Ca and Ti but low Al concentration of the UML magma and can therefore be regarded as characteristic for UML–carbonatite associations (Platt & Mitchell, 1979; Rock, 1986; Tappe *et al.*, 2005*a*). These garnets do not occur in kimberlites and lamproites (Mitchell & Bergman, 1991; Mitchell, 1995).

PRESSURE ESTIMATES FOR COGNATE INCLUSIONS

The clinopyroxenes and rare calcic amphibole of the clinopyroxene–phlogopite nodules allow qualitative pressure estimates. The clinopyroxene barometer of Nimis & Ulmer (1998) requires an independent temperature estimate, which we obtained using the clinopyroxene thermometer of Kretz (1982). The uncertainty in temperature is 60 °C (1σ) and results in large errors in pressure estimates (0·3 GPa, 1σ). Nevertheless, the crystallization pressure of clinopyroxenes from several clinopyroxene–phlogopite nodules can be bracketed between 0·8 and 1·5 GPa, corresponding to ~25–45 km depth. Rare clinopyroxene from an olivine–phlogopite nodule gives a similar pressure estimate of 0·9–1·7 GPa.

Calcic amphibole in clinopyroxene–phlogopite nodules yielded the lowest crystallization pressures of 0·4–0·7 GPa (Al-in-hornblende barometer of Hammarstrom & Zen, 1986), corresponding to ~10–20 km depth. This agrees with textural relations indicating late melt/fluid infiltration into the nodule material (Fig. 6f). No pressure estimate can be given for the glimmerite nodules, but the low-Ba mica compositions may be a reflection of comparably high crystallization pressures (Guo & Green, 1990).

MINERALOGICAL CONSTRAINTS ON CRYSTALLIZATION CONDITIONS AND THEIR IMPLICATIONS FOR MANTLE SOURCE CHARACTERISTICS

Oxygen fugacity estimates from olivine–spinel and ilmenite–magnetite pairs

Olivine and Cr-spinel are the earliest phases crystallized from aillikite magma and may be used to constrain the oxygen fugacity conditions during early stages in UML magma evolution. We applied the $FeMg_{-1}$ exchange thermometer of O'Neill & Wall (1987) and the olivine–orthopyroxene–spinel oxybarometer of Ballhaus *et al.* (1991). Ferric iron in spinel was calculated assuming stoichiometry (Ballhaus *et al.*, 1990). Because ultramafic lamprophyres are not saturated in orthopyroxene, the oxybarometer of Ballhaus *et al.* (1991) yields maximum fO_2 values, which can be corrected for the appropriate silica activity of the melt as outlined by Fedortchouk & Canil (2004). The perovskite–titanite reaction (Nicholls *et al.*, 1971) rather than the monticellite–diopside reaction as chosen by Fedortchouk & Canil (2004) for kimberlite was considered as the upper limit of silica activity controlling UML magma evolution at Aillik Bay. This assumption is consistent with the observation that perovskite and diopside-rich clinopyroxene frequently occur in the groundmass of these rocks. Some damtjernites contain perovskite and titanite in reaction relationship, indicating that crystallization occurred along this silica activity buffer. We assumed an equilibration pressure for olivine–spinel pairs of 1 GPa: pressure has only a minor influence on the calculation of the equilibrium olivine–spinel crystallization temperature (20 °C/GPa) and oxygen fugacity (0·03 log-bar units/GPa).

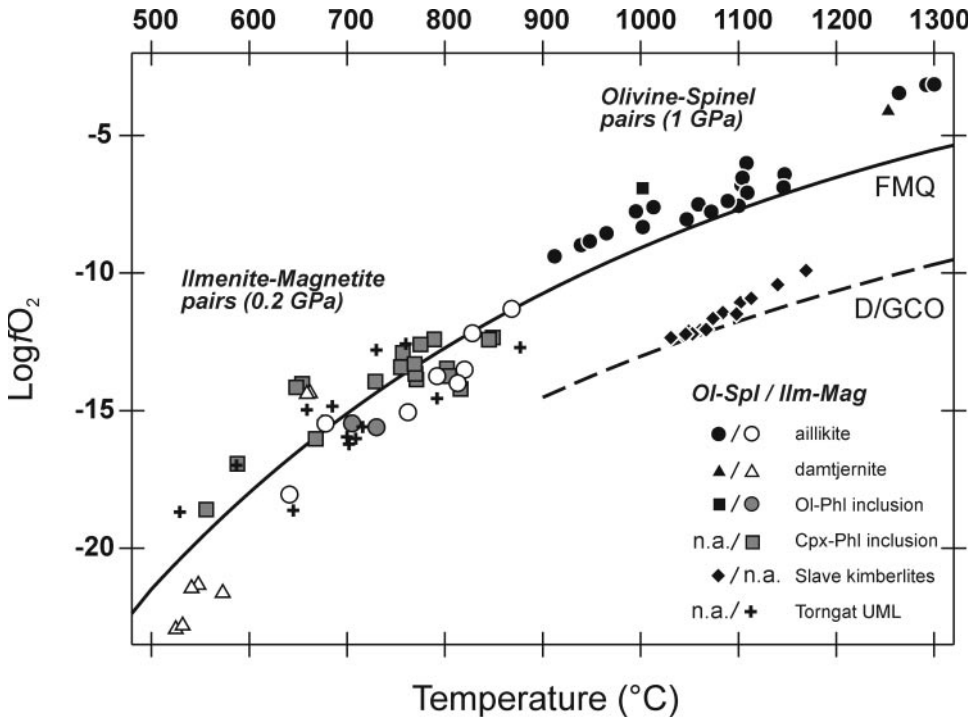

Fig. 11. Log oxygen fugacity vs equilibration temperature (°C) calculated for olivine–spinel and ilmenite–magnetite pairs (note different symbols; n.a., not analyzed) in ultramafic lamprophyres and their cognate inclusions from the Aillik Bay area. The FMQ (fayalite–magnetite–quartz) and D/GCO (diamond/graphite–CO) buffer curves were calculated according to Frost (1991) and Frost & Wood (1997), respectively. Data for Slave craton kimberlites are from Fedortchouk & Canil (2004). Torngat UML ilmenite–magnetite pairs are the first author's unpublished data from the dyke swarm described by Tappe *et al.* (2004). Symbol size is equal to the 2σ error.

The olivine–spinel equilibration temperatures for the aillikite magma range from 912 °C to 1300 °C (Fig. 11). The oxygen fugacity varies from FMQ −0·03 to FMQ +2·43 (log-bar unit deviation from fayalite–magnetite–quartz buffer) with most pairs recording fO_2 slightly above the FMQ buffer. An olivine–spinel pair from a damtjernite (1253 °C; FMQ +1·84), and from an olivine–phlogopite cognate inclusion (1002 °C; FMQ +1·83) fall within the fO_2–T range calculated for aillikites.

The oxygen fugacity during UML groundmass crystallization was estimated from late ilmenite–magnetite pairs (0·2 GPa; QUILF-95 program; Andersen *et al.*, 1993). Results scatter around the FMQ buffer (FMQ −1·81 to FMQ −0·03 for aillikite; FMQ −1·98 to FMQ +1·89 for cognate inclusions; Fig. 11). Lower equilibration temperatures calculated for these ilmenite–magnetite pairs than for olivine–spinel phenocrysts are in keeping with the distinct crystallization stages. Ilmenite–magnetite temperatures for aillikites and micaceous cognate inclusions range from 868 °C to 641 °C, and 849 °C to 556 °C, respectively. Temperatures for damtjernite are at the lower end of this range (662–525 °C) and the few fO_2 values for damtjernites show the greatest negative deviation from FMQ (FMQ −3·35 to FMQ +1·37) presumably reflecting sub-solidus re-equilibration (Fig. 11).

The oxygen fugacity values for UML from Aillik Bay are significantly higher than those for diamondiferous Slave craton kimberlites (Fig. 11; <FMQ −2·0; Fedortchouk & Canil, 2004), which lie close to the D/GCO (diamond/graphite–CO) buffer. Highly reduced crystallization conditions were also calculated for kimberlites from the Kaapvaal craton (Mitchell, 1973). Because the redox state of a primitive mafic magma has the potential to preserve that of its source (Carmichael, 1991), it can be inferred that the UML magma was derived from a fairly oxidized mantle region beneath the stretched North Atlantic craton in contrast to comparatively reduced sources for kimberlites within a stable cratonic mantle.

Hydrogen fluoride fugacity estimates from phlogopite-apatite pairs

Estimates of crystallization temperature and relative hydrogen fluoride (HF) fugacity in the UML magma were obtained from coexisting apatite and phlogopite crystals (Fig. 12). Equilibrium is assumed based on textures and mode of occurrence, e.g. apatite inclusions

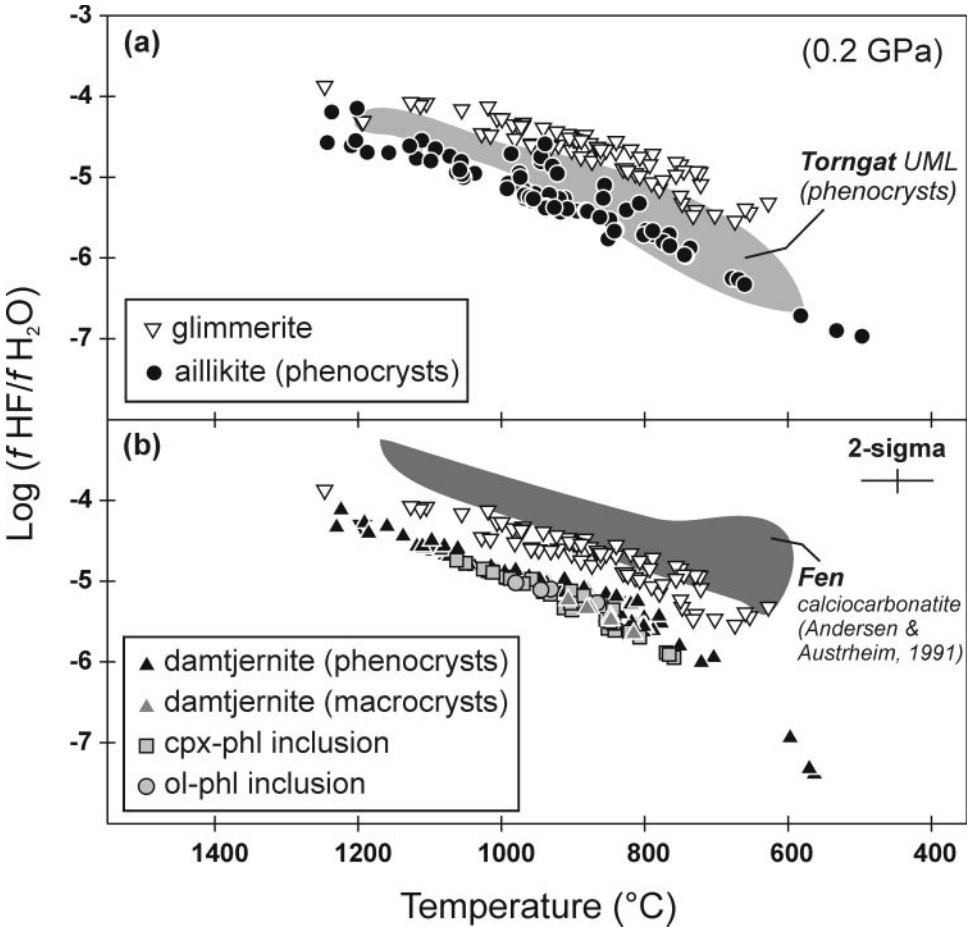

Fig. 12. Relative HF fugacity log(fHF/$f$$H_2O$) vs equilibration temperature (°C) calculated for apatite–phlogopite pairs (0·2 GPa, following Andersen & Austrheim, 1991) from Aillik Bay ultramafic lamprophyres and their cognate inclusions. Field for Torngat UML (aillikites/mela-aillikites) in (a) is from the first author's unpublished data from the dyke swarm described by Tappe *et al.* (2004). Glimmerite data are displayed in both (a) and (b) for easier comparison.

in phlogopite (Fig. 5f and g), and equilibrium pressure was set at a minimum of 0·2 GPa.

The biotite–apatite geothermometer recalibrated by Zhu & Sverjensky (1992) yields rough temperature estimates in the range 1250–500 °C for aillikites and damtjernites from the Aillik Bay area (mean error = ±50 °C at 1σ). The micaceous cognate inclusions from aillikites and macrocrysts from damtjernites fall within this temperature range. High temperatures of the UML phlogopites at low crystallization pressures are also indicated by their high TiO_2 concentrations (Forbes & Flower, 1974; Robert, 1976; Righter & Carmichael, 1996). Apatite inclusions in olivine phenocrysts indicate early crystallization of apatite.

Estimates of the relative HF fugacity, log(fHF/$f$$H_2O$), based on Andersen & Austrheim (1991), using the apatite–phlogopite equilibrium temperature yield values between −4 and −7 ± 0·15 for Aillik Bay UML and associated cognate inclusions (Fig. 12). The correlation between HF fugacity and temperature displays a relatively shallow (slow) cooling trend internally buffered by phlogopite, consistent with mica being the dominant phase.

There is considerable overlap between relative HF fugacities recorded by Aillik Bay aillikite and damtjernite phenocrysts, and cognate clinopyroxene–phlogopite and olivine–phlogopite inclusions also fall within this range. Interestingly, the glimmerite inclusions record higher relative HF fugacities than their aillikite hosts and the remainder of the cognate inclusions at a given equilibration temperature (Fig. 12).

In summary, apatite and phlogopite equilibrated throughout the crystallization sequence of the UML magma (near liquidus to near solidus). Aillik Bay aillikites, damtjernites and cognate clinopyroxene–phlogopite/olivine–phlogopite inclusions experienced a similar evolution in terms of volatile fugacities. However, glimmerite nodules crystallized under higher relative HF

fugacity conditions over a similar wide temperature range. The estimated relative HF fugacity of the Aillik Bay area UML is considerably lower than reported for carbonatites (Fig. 12; Fen complex; Andersen & Austrheim, 1991), but compares well with carbonate-rich UML from the Torngat Mountains (own data) and the Delitzsch complex, Germany (Seifert *et al.*, 2000). The generally F-poor, OH-rich nature of phlogopites in Aillik Bay UML (<1 wt % F) may result from highly oxidizing crystallization conditions (Foley, 1989*b*), which is in marked contrast to the high F content in lamproitic micas (1–7 wt %; Mitchell & Bergman, 1991), which were experimentally shown to be derived from F-rich reduced mantle sources (Foley *et al.*, 1986). Oxidizing crystallization conditions might also be responsible for the elevated Al content of the UML micas (atomic K/Al <1 vs >1 in lamproite micas at similarly strong bulk-rock Al depletion). The pronounced replacement of Mg by Ti leading to octahedral site vacancies is also in keeping with a redox control (Arima & Edgar, 1981; Foley, 1989*b*).

GEOCHEMISTRY AND ISOTOPIC COMPOSITION

Major and compatible trace elements

Extreme SiO_2 undersaturation, Al depletion, strong Ca enrichment and a potassic character is the hallmark of all members of the Aillik Bay UML suite (Fig. 13; Table 12 and Electronic Appendix 3). The aillikites contain 17–29·4 wt % SiO_2 and 15–20·4 wt % MgO (Fig. 14). Mg-number ranges between 60 and 77, and Al_2O_3 concentrations are below 3·5 wt %. CaO is high but variable (13–24·7 wt %) and TiO_2 is elevated (2·5–3·8 wt %) compared with kimberlites (Fig. 13). Moderately high K_2O concentrations (1·3–2·4 wt %) but extreme Na_2O depletion (<0·7 wt %) are characteristic for aillikites. P_2O_5 (0·9–3·2) and CO_2 (10·1–20·8 wt %) concentrations are higher in aillikites than in mela-aillikites (P_2O_5 = 0·2–1·3 wt %; CO_2 = 2–9·9 wt %; Figs 13 and 15). The latter have elevated SiO_2 (30·7–36 wt %), TiO_2 (3·7–5·8 wt %), Al_2O_3 (3·7–4·8 wt %) and K_2O (up to 3·1 wt %) but much lower CaO (7·4–12·4 wt %) concentrations. Cr and Ni contents are high in aillikites (210–574 ppm Ni, 322–857 ppm Cr) and even higher in mela-aillikites (572–787 ppm Ni, 705-1150 ppm Cr; Fig. 14).

Damtjernites have higher SiO_2 (29·3–38 wt %), TiO_2 (3·5–6·9 wt %), Al_2O_3 (3·6–9·9 wt %) and Na_2O (0·2–4·3 wt %) than aillikites (Fig. 13), reflecting less primary carbonate and the occurrence of clinopyroxene plus a felsic mineral in the groundmass. MgO varies considerably between 5·5 and 16 wt % (Fig. 14), which translates into a wide Mg-number range (40–67). Damtjernites have Ni and Cr concentrations that range from values typical for mantle-derived primitive magmas to low values close to the detection limit (22–517 ppm Ni; <10–586 ppm Cr; Fig. 14). There is some overlap with the major element composition of mela-aillikites (which lack the felsic groundmass component), but evolved damtjernites approach significantly higher levels of SiO_2, Al_2O_3 and Na_2O (Fig. 13). K_2O and P_2O_5 concentrations can be high (0·9–3·5 and 0·7–3·6 wt %, respectively), as is the amount of CO_2 (0·2–10·9 wt %).

Carbonatites typically contain <18 wt % SiO_2 but may approach 22 wt % SiO_2 (Fig. 13). They classify chemically as magnesiocarbonatite but a few straddle the boundary to ferruginous calciocarbonatite (Gittins & Harmer, 1997). In the Aillik Bay UML suite, they are the rock types with lowest concentrations of TiO_2 and Al_2O_3 (typically <2·6 and 3·3 wt %, respectively). CaO (17–38·4 wt %), MgO (6·3–16·8 wt %), Fe_2O_3 (5·3–11·9) and MnO (up to 0·6 wt %) concentrations are high in both dolomite–calcite carbonatite and dolomite carbonatite. The CO_2 content of the dolomite carbonatite is higher (32·2–39·5 wt %) than in the mafic silicate-bearing calcitic carbonatites (17·3–30·5 wt %; Fig. 13). K_2O and P_2O_5 contents approach 2·5 and 4·5 wt %, respectively. Dolomite carbonatite is Ni and Cr depleted (<60 ppm), but concentrations in dolomite–calcite carbonatite may be up to 300 and 750 ppm, respectively.

Incompatible trace elements

Primitive mantle-normalized incompatible element abundances are displayed in Fig. 16. Aillikites are strongly enriched in Cs, Ba, Th, U, Nb, Ta and LREE with normalized concentrations of up to 600 × primitive mantle. Relative depletions are apparent at Rb, K, Pb, Sr, P, Zr, Hf and the heavy REE (HREE), which can be as low as 3 × primitive mantle (Fig. 16a). REE fractionation is extreme, with La_N/Yb_N between 70 and 136 (Fig. 13) and Sm_N/Yb_N between 18 and 30. The strong relative Zr–Hf depletion in aillikites, quantified by a (Zr + Hf)/(Zr + Hf)* ratio of 0·15–0·41, whereby (Zr + Hf)* is interpolated between neighbouring Nd and Sm, is surpassed only by the carbonatites. Low Zr/Nb ratios (1·2–4) are an expression of the strong incompatible trace element enrichment. Mela-aillikites have lower incompatible element abundances than aillikites but exhibit a similar pattern (Fig. 16a). However, the relative Zr–Hf depletion (0·47–0·87) and LREE/HREE fractionation (La_N/Yb_N = 33–84) are less pronounced.

Damtjernites exhibit similar enrichments in Th, U, low field strength elements (LFSE) and LREE to aillikites. However, marked differences between the two UML variants are apparent in the elevated Nb, Ta, Zr, Hf and HREE concentrations of the damtjernites (Figs 15a and 16b). Interestingly, the intra-HFSE

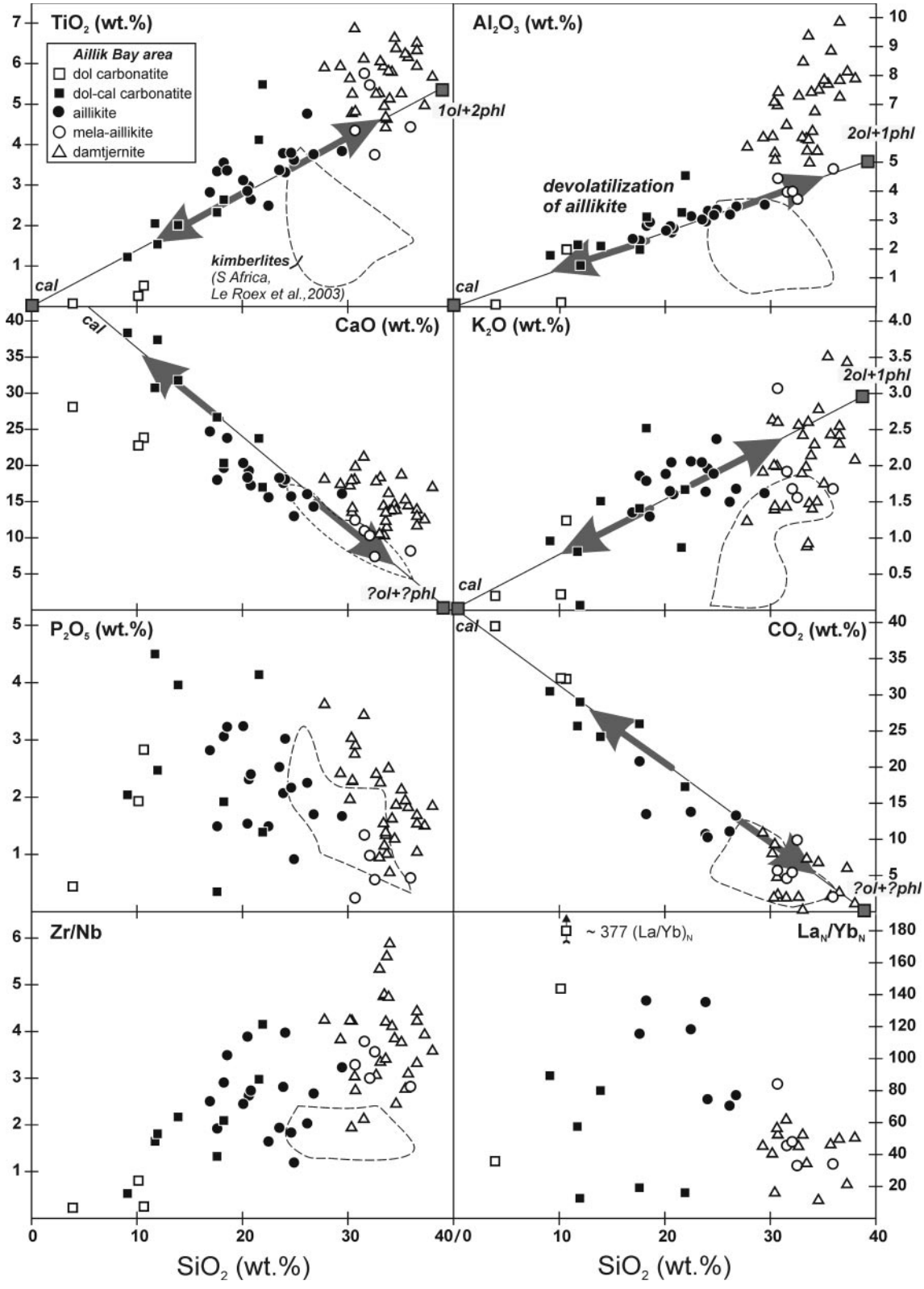

Fig. 13. Major element oxide and trace element ratios vs SiO_2 (wt %) for Aillik Bay UML and carbonatites. Arrows and trend lines illustrate the devolatilization of aillikites leading to carbonatites and mela-aillikites. Dashed outlines indicate the field for hypabyssal kimberlites from Kimberley, South Africa (Le Roex *et al.*, 2003). La_N/Yb_N ratios are chondrite-normalized using values from Sun & McDonough (1989).

Table 12: Major (wt %) and trace element (ppm) concentrations of representative Neoproterozoic Aillik Bay area UML and carbonatites

Rock type:	ultramafic lamprophyres													
	aillikite							mela-aillikite			damtjernite			
Sample no.:	L60	ST109	ST164	ST198A	ST220II	ST225	ST250A	ST147B	ST196	ST244B	ST140	ST170	ST174	ST188A
SiO_2	23·9	18·2	24·1	26·8	26·1	26·4	22·5	31·6	35·9	32·1	31·5	38·0	33·1	30·7
TiO_2	3·8	3·6	3·3	3·8	4·8	3·3	2·5	5·8	4·4	5·5	6·1	5·7	6·1	4·8
Al_2O_3	3·0	2·8	3·3	3·5	3·2	2·5	3·1	4·0	4·8	4·0	6·3	7·9	8·5	7·4
$Fe_2O_3^T$	13·5	16·0	13·2	13·7	15·0	13·2	12·2	17·5	14·7	14·7	13·8	14·3	15·8	14·4
MnO	0·3	0·3	0·2	0·2	0·2	0·2	0·2	0·2	0·2	0·2	0·2	0·2	0·3	0·3
MgO	19·1	15·9	18·6	17·3	16·5	20·9	20·4	16·8	22·2	20·2	9·6	6·8	5·9	6·4
CaO	17·6	19·7	18·1	14·3	16·1	16·4	15·6	11·0	8·2	10·3	21·2	17·0	18·3	19·8
Na_2O	0·3	0·2	0·2	0·7	0·7	0·2	0·2	0·6	0·5	0·6	0·5	1·3	2·2	4·3
K_2O	1·6	1·8	2·0	1·7	1·5	1·4	2·1	1·9	1·7	1·7	1·4	2·1	2·4	2·6
P_2O_5	2·1	3·1	3·0	1·7	2·3	2·0	1·5	1·3	0·6	1·0	3·4	1·8	2·3	2·9
H_2O*	3·2	3·8	2·5	1·7	1·4	2·2	4·7	3·4	3·9	3·0	2·5	2·5	3·6	2·9
CO_2	10·8	13·5	10·3	13·3	11·1	10·1	13·8	4·6	2·0	5·4	1·9	1·1	0·2	2·3
Total	98·9	98·7	98·7	98·6	98·8	98·9	98·7	98·6	99·0	98·6	98·4	98·7	98·6	98·8
Mg-no.	73·8	66·3	73·7	71·4	68·6	75·8	76·9	65·4	75·0	73·1	58·1	48·5	42·4	46·7
LFSE														
Cs	1·56	1·53	1·94	1·23	2·29	n.a.	6·13	1·56	4·97	2·83	n.a.	0·57	1·18	1·38
Rb	55	61	66	49	38	29	75	49	65	58	47	32	56	55
Ba	1860	2777	1540	1028	714	1018	1366	594	622	838	1156	846	1583	1205
Sr	2685	1678	2784	1318	2511	2868	1312	1330	564	1147	1342	1074	3958	3346
HFSE														
Th	24·07	23·99	14·90	13·49	16·99	20·11	15·49	9·18	5·76	14·86	12·47	48·66	38·66	22·99
U	18·17	4·54	11·54	9·16	9·34	7·02	6·01	4·47	1·19	7·12	7·84	7·88	11·71	9·95
Nb	166	203	153	131	177	159	184	130	109	117	343	205	373	316
Ta	12·55	12·74	8·68	7·86	8·57	9·91	10·35	7·47	5·52	7·78	15·98	17·55	20·76	13·95
Pb	13·0	11·9	8·5	5·4	7·5	9·6	10·8	4·2	n.a.	4·6	5·5	22·7	56·6	13·5
Zr	466	591	608	350	359	306	303	491	306	351	729	735	1247	865
Hf	11·45	13·95	14·20	7·90	8·46	7·30	8·62	11·74	8·45	9·06	22·01	19·27	33·26	18·97
Y	41	43	46	35	55	43	27	35	18	28	85	72	95	92
REE														
La	367	390	235	182	272	335	242	116	52	112	312	267	358	354
Ce	744	819	469	391	572	700	476	268	109	240	624	627	750	619
Pr	86·3	95·8	55·1	45·9	65·5	82·3	52·4	32·7	13·1	28·4	56·7	77·0	86·9	67·4
Nd	322	364	215	181	251	319	188	134	53	112	216	309	339	255
Sm	49·8	54·6	36·8	31·3	45·4	47·2	28·1	25·8	10·6	21·2	45·2	56·0	64·6	51·5
Eu	12·54	13·46	10·11	8·45	12·43	12·57	7·14	7·16	3·03	6·00	14·73	15·60	18·98	15·75
Gd	30·82	33·37	26·47	21·52	30·98	30·68	17·37	19·24	8·19	14·91	37·95	38·89	48·38	41·52
Tb	3·14	3·30	3·02	2·43	3·64	3·38	1·91	2·24	1·04	1·83	5·32	4·67	6·18	5·61
Dy	12·29	12·82	12·51	9·80	15·13	13·23	7·70	9·47	4·44	7·50	24·09	20·05	26·71	24·46
Ho	1·59	1·65	1·74	1·30	2·10	1·83	1·11	1·31	0·64	1·12	3·88	2·82	3·97	3·53
Er	3·44	3·63	3·98	2·95	4·84	4·00	2·44	2·91	1·52	2·64	7·33	6·60	8·53	8·17
Tm	0·38	0·39	0·44	0·34	0·54	0·42	0·29	0·33	0·19	0·32	0·78	0·74	0·91	0·94
Yb	1·95	2·05	2·26	1·69	2·77	2·19	1·47	1·82	1·10	1·68	3·63	3·81	4·91	4·85
Lu	0·22	0·23	0·27	0·20	0·30	0·25	0·17	0·22	0·14	0·20	0·41	0·46	0·60	0·58
Transition metals														
Cr	601	520	700	726	606	577	734	705	1150	939	3	b.d.	b.d.	b.d.
Co	67	62	66	73	75	78	63	91	90	88	42	36	31	37
Ni	441	211	483	509	493	719	487	593	749	670	96	43	23	61
Sc	24	28	29	20	18	15	21	23	22	25	31	21	16	10
V	205	267	204	211	242	194	197	293	267	287	305	318	390	328

Table 12: continued

Rock type:	ultramafic lamprophyres						carbonatites						
	damtjernite				olivine-accumulated damtjernite		dolomite carbonatite			dolomite–calcite carbonatite			
Sample no.:	ST206AI	ST226	ST246A	ST256	ST114B	ST224B	L1	ST189	ST203	ST126	ST193A	ST198C	ST199
SiO_2	30·6	36·5	34·6	32·7	30·2	33·5	10·7	3·9	10·1	17·6	9·1	11·7	13·9
TiO_2	6·9	5·9	6·4	5·2	5·6	4·9	0·5	0·1	0·3	2·3	1·2	2·1	2
Al_2O_3	7·0	9·9	7·5	7·3	5·9	5·4	2	0·1	0·2	2	1·8	2·1	2·1
$Fe_2O_3^T$	15·7	14·8	14·5	15·0	15·3	15·8	7·3	6·2	8·6	8·4	5·3	10·4	8·3
MnO	0·2	0·3	0·2	0·3	0·2	0·2	0·5	0·6	0·5	0·3	0·3	0·3	0·3
MgO	7·8	6·3	6·4	7·9	9·8	15·9	11·1	16·8	12·9	10·7	7·2	8·3	8·1
CaO	18·0	13·9	13·8	17·8	17·2	10·3	23·9	28·1	22·8	26·7	38·4	30·8	31·8
Na_2O	1·1	2·1	1·9	2·1	0·9	1·7	0·4	0·7	1·1	0·2	0·2	1·4	1·1
K_2O	2·0	2·3	2·8	2·6	2·6	0·9	1·2	0·2	0·2	1·4	1	0·8	1·5
P_2O_5	2·8	1·7	1·9	2·4	2·0	1·2	2·8	0·4	1·9	0·4	2	4·5	4
H_2O*	1·8	3·0	2·1	3·4	1·1	1·8	0	2·2	0·2	2·7	1·6	0·6	1·5
CO_2	4·8	2·6	6·8	2·0	8·1	7·3	32·2	39·5	32·3	26	30·5	25·7	24·2
Total	98·7	99·3	98·8	98·6	98·9	98·8	92·5	98·7	91	98·8	98·5	98·6	98·7
Mg-no.	49·6	45·7	46·8	51·0	55·9	66·5	75·2	84·3	74·9	71·6	72·8	61·3	65·9
LFSE													
Cs	0·94	22·81	1·37	n.a.	2·95	18·40	n.a.	n.a.	b.d.	1·06	b.d.	2·98	n.a.
Rb	56	63	70	127	85	38	38	14	31	85	22	19	30
Ba	1213	1443	1292	1469	877	635	23578	7130	37275	1680	6958	1528	1835
Sr	1372	1344	1418	3296	2011	932	3355	1870	2015	1005	3060	5555	3427
HFSE													
Th	43·39	32·82	39·21	16·03	9·98	10·02	64	111·04	128·77	16·69	10·84	40·14	13·44
U	10·69	6·74	6·74	9·72	11·45	1·85	38·9	6·4	6·38	1·89	8·42	8·19	20·27
Nb	226	256	218	274	152	94	434	154	94	245	207	269	233
Ta	18·53	18·38	14·74	10·18	7·71	5·15	9·71	0·24	5·2	18·04	2·92	13·06	7·95
Pb	12·1	10·0	12·0	11·6	7·5	n.a.	31·5	46	46·5	9	11·3	12·5	18·2
Zr	686	849	534	838	643	451	110	35	75	325	110	443	506
Hf	19·34	21·50	18·46	19·60	15·80	12·15	1·72	1·79	3·11	13·94	3·28	9·71	9·47
Y	82	79	194	76	42	31	98	90	65	49	45	123	57
REE													
La	308	310	226	278	140	83	3920	1520	1490	215	347	564	376
Ce	684	625	425	500	284	180	6780	3000	2850	431	510	1240	741
Pr	78·5	69·0	47·5	56·6	33·0	21·8	594·2	305·3	369·6	46·4	52·1	147·3	82·3
Nd	318	270	181	219	132	93	1690	1040	1030	167	185	607	314
Sm	60·2	49·8	39·6	42·7	24·9	18·6	139	107	106	23·3	29	100	49·4
Eu	17·43	14·62	11·35	13·50	7·15	5·39	26·72	22·26	20·62	5·28	7·9	27·02	13·78
Gd	46·01	36·97	37·79	34·15	19·16	14·27	59·88	45·86	44·23	13·73	18·9	68·27	32·56
Tb	5·82	4·77	6·23	4·86	2·42	1·83	4·72	4·22	3·39	1·61	2·24	7·71	3·81
Dy	23·96	20·63	36·42	21·52	10·52	7·99	20·7	15·07	13·88	8·08	9·68	32·38	15·67
Ho	3·32	3·02	7·25	3·15	1·55	1·17	3·38	2·7	2·23	1·58	1·44	4·52	2·24
Er	7·73	7·08	20·87	7·37	3·59	2·77	9·92	12·84	6·68	5·88	3·68	10·34	5·26
Tm	0·78	0·87	2·74	0·84	0·44	0·34	1·21	3·07	0·98	1·08	0·48	1·26	0·62
Yb	3·92	4·49	14·43	4·44	2·50	1·73	7·47	30·52	7·43	8·07	2·79	7·04	3·37
Lu	0·42	0·51	1·64	0·52	0·33	0·20	0·98	4·97	1·21	1·35	0·38	0·87	0·42
Transition metals													
Cr	25	58	32	52	465	586	60	b.d.	b.d.	618	139	b.d.	44
Co	44	37	35	38	61	78	17	6	6	58	16	23	21
Ni	85	55	46	93	218	513	40	b.d.	b.d.	204	87	33	74
Sc	25	13	18	18	30	24	48	b.d.	26	25	12	14	14
V	379	346	380	405	369	289	85	30	73	112	168	197	298

*Calculated difference of 'loss on ignition' and CO_2 content.
Mg-number (minimum mg-number with Fe^{2+} as total Fe) = $100[Mg/(Mg + Fe^{2+})]$ in atomic units; n.a., not analyzed; b.d., below detection.

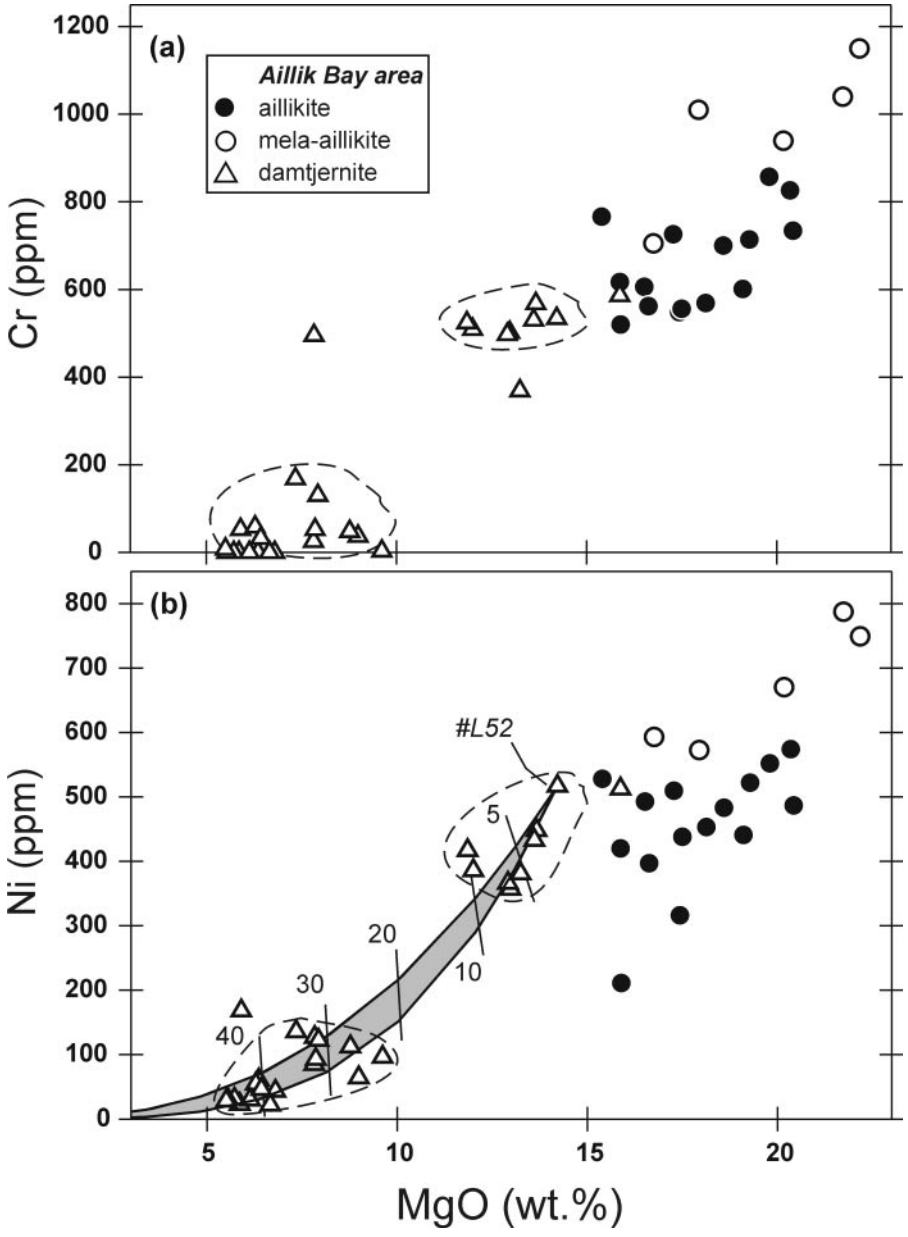

Fig. 14. Cr (a) and Ni (b) contents (ppm) vs MgO (wt %) in ultramafic lamprophyres from the Aillik Bay area. Carbonatites are not shown for clarity. The apparent bimodality of damtjernites is emphasized by the dashed fields. Grey-shaded calculated olivine fractionation curve in (b) starts at the most primitive damtjernite (L52) with D_{MgO} set at 2·6 and a D_{Ni} range between 4·9 and 6·5 following the formulations of Herzberg & O'Hara (2002). Numbers on the tick marks indicate the amount of olivine (wt %) removed.

(high field strength element) fractionation is similar in the two UML types, as exemplified by broadly overlapping Zr/Nb ratios of damtjernites (2–6) and aillikites (1·2–4; Fig. 13). The relative Zr–Hf depletion (0·33–0·55) of damtjernites is often less pronounced than in aillikites (<0·41). The REE are less fractionated in the damtjernites than in aillikites, as indicated by their lower La_N/Yb_N (45–62; Fig. 13) and Sm_N/Yb_N (11–17) ratios.

Incompatible elements in the carbonatites are extremely fractionated with strong Ba, Th and REE enrichment but Rb, K, Zr, Hf and Ti depletion (Fig. 16c). Whereas the patterns of the mixed dolomite–calcite carbonatites (La_N/Yb_N = 13–89) have some resemblance to those of aillikites, those for dolomite carbonatites (La_N/Yb_N = 36–377) are different, with LREE concentrations >1000 × primitive mantle, coupled with strong Zr–Hf depletions (0·01–0·02).

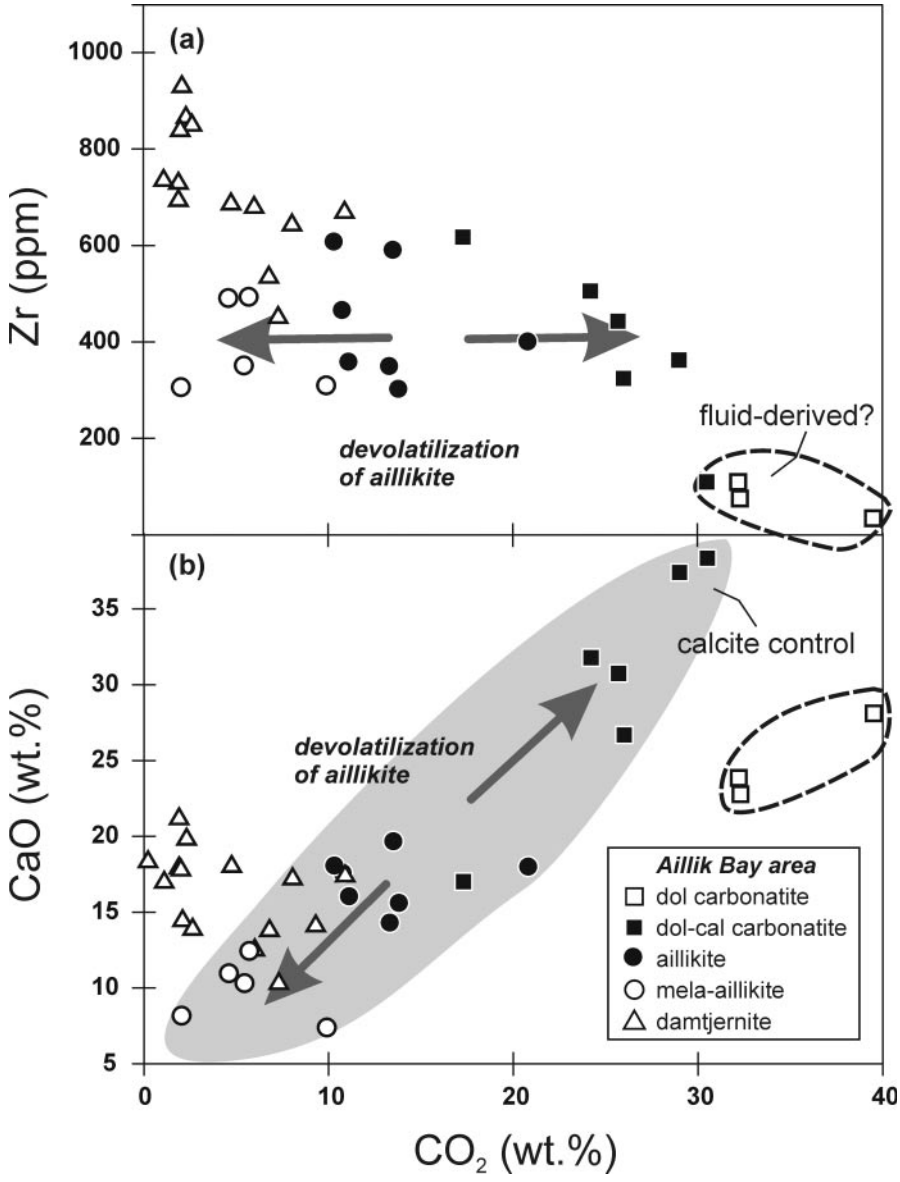

Fig. 15. Zr (a) and CaO (b) contents vs CO_2 (wt %) of ultramafic lamprophyres and carbonatites from the Aillik Bay area. Arrows and trend line illustrate the fractionation relationship between aillikites and carbonatites along a $CaCO_3$ control line leaving a mela-aillikite residue.

Sr–Nd isotope composition

Bulk-rock Sr and Nd isotope compositions are listed in Table 13. Carbonatites, aillikites, mela-aillikites and damtjernites show overlapping compositions forming a horizontal array in Sr–Nd isotope space close to Bulk Earth (Fig. 17). Age-corrected $\varepsilon_{Nd(582)}$ values (+0·1 to +1·9) fall within a narrow range, and $^{87}Sr/^{86}Sr_{(i)}$ ratios vary from 0·70369 to 0·70466. Two samples, the dolomite–calcite carbonatite ST126 and the damtjernite ST256, have a more radiogenic Sr isotope composition (0·70579 and 0·70662, respectively) defining the high $^{87}Sr/^{86}Sr_{(582)}$ end of the horizontal array (Fig. 17). As leached fractions of ST126 and ST256 yielded a similarly radiogenic $^{87}Sr/^{86}Sr_{(582)}$ (0·70568 and 0·70526, respectively) and these samples do not show any other anomalous features compared with the other samples, we consider their Sr isotope composition to be primary. The clinopyroxene–phlogopite nodule ST162I falls within the Sr–Nd compositional range of the UML and carbonatites ($^{87}Sr/^{86}Sr_{(i)} = 0{\cdot}70393$; $\varepsilon_{Nd(i)} = +0{\cdot}25$).

Carbon and oxygen isotope composition of the bulk-rock carbonate fraction

The bulk-rock carbonate fraction of aillikites varies relatively little in $\delta^{13}C_{PDB}$ (–5·7 to −5‰) and $\delta^{18}O_{SMOW}$

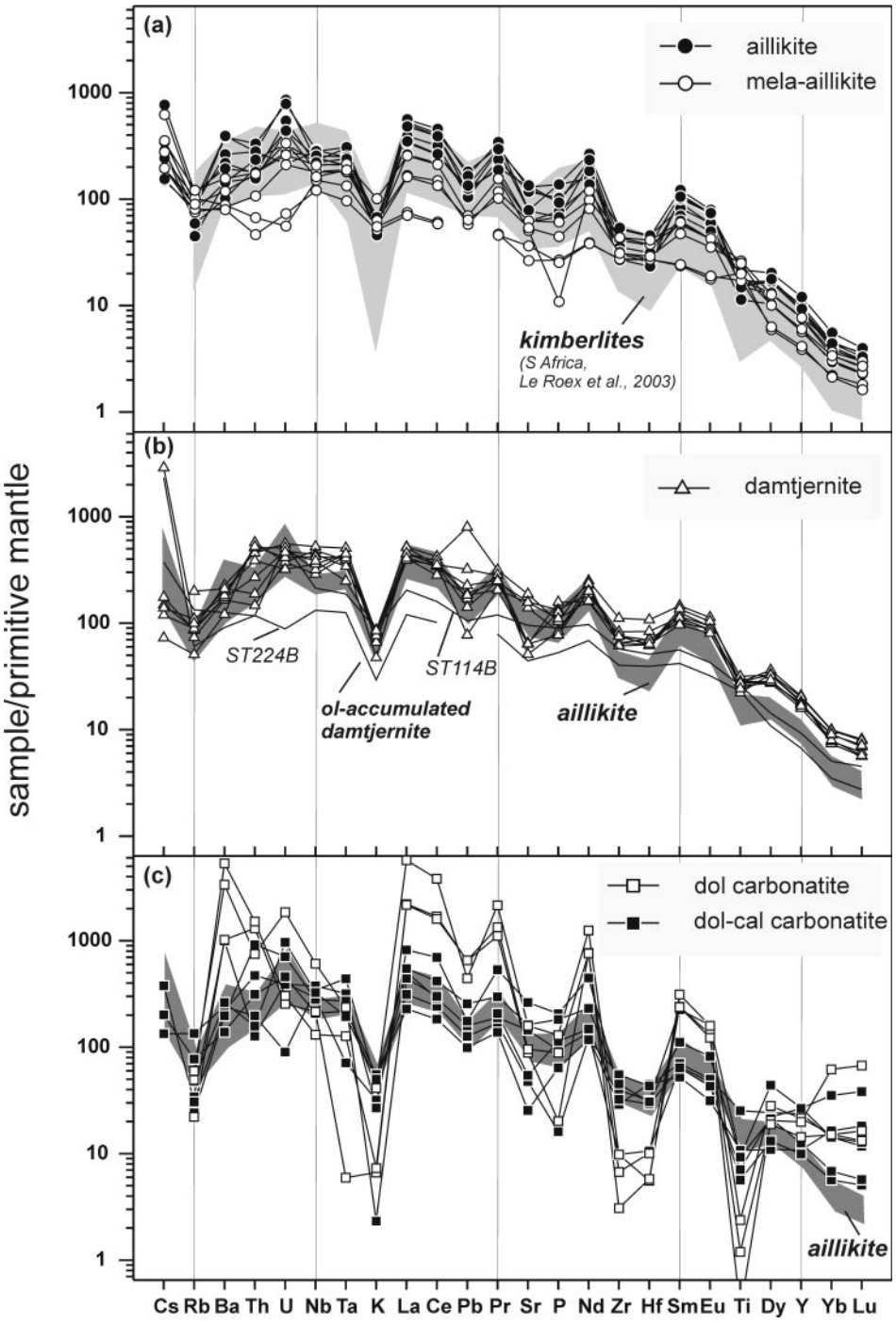

Fig. 16. Primitive mantle-normalized incompatible element diagrams for (a) aillikites/mela-aillikites, (b) damtjernites, and (c) carbonatites from the Aillik Bay area. Grey-shaded area in (a) indicates the trace element patterns of hypabyssal kimberlites from Kimberley, South Africa (Le Roex *et al.*, 2003). Grey-shaded field in (b) and (c) represents the range of aillikite compositions from (a) for easier comparison. Primitive mantle values and element sequence are after Sun & McDonough (1989).

(9·4–11·6‰), with sample ST220II being exceptional in approaching $\delta^{13}C$ of −4‰ (Fig. 18; Table 14). The dolomite–calcite carbonatites have a heavier carbon isotope composition (–3·7 to −3·3‰ $\delta^{13}C$) than the associated aillikites, with only sample ST199 being less ^{13}C enriched (–4·8‰), close to values typical for aillikites. The oxygen isotope composition (9·6–10·8‰ $\delta^{18}O$) is within the range of the aillikites. Only sample

Table 13: Sr–Nd isotope composition of representative Neoproterozoic Aillik Bay area UML, carbonatites and a cognate inclusion

Sample no.	Rb	Sr	$^{87}Sr/^{86}Sr_m$	$^{87}Sr/^{86}Sr_i$*	Sm	Nd	$^{143}Nd/^{144}Nd_m$	$^{143}Nd/^{144}Nd_i$*	$(\varepsilon_{Nd})_i$†	$T^{Nd}_{(DM)}$‡
Aillikite										
L60	55·3	2685	0·704371(7)	0·70389	49·8	322	0·512264(5)	0·51191	0·4	1·1
ST109	61·0	1678	0·704828(7)	0·70398	54·6	364	0·512253(3)	0·51191	0·3	1·0
ST164	66·3	2784	0·704497(7)	0·70394	36·8	215	0·512314(5)	0·51192	0·6	1·1
ST220II	37·9	2511	0·704040(7)	0·70369	45·4	251	0·512313(5)	0·51189	0·1	1·1
ST225	28·8	2868	0·703999(7)	0·70376	47·2	319	0·512279(5)	0·51194	0·9	1·0
ST250A	74·9	1312	0·705223(10)	0·70389	28·1	188	0·512251(6)	0·51191	0·3	1·0
Mela-aillikite										
ST147B	48·6	1330	0·704654(10)	0·70380	25·8	134	0·512335(4)	0·51189	0·1	1·2
ST196	65·5	564	0·705967(7)	0·70325	10·6	53·4	0·512399(5)	0·51194	1·0	1·1
ST244B	57·5	1147	0·705726(7)	0·70455	21·2	112	0·512419(5)	0·51198	1·8	1·0
Cpx–phl nodule										
ST162I	90·2	510	0·708075(7)	0·70393	6·8	29·1	0·512446(5)	0·51190	0·2	1·4
Damtjernite										
ST140	46·6	1342	0·704384(7)	0·70357	45·2	216	0·512446(5)	0·51196	1·4	1·1
ST174	55·7	3958	0·704304(7)	0·70397	64·6	339	0·512372(8)	0·51193	0·8	1·1
ST188A	54·6	3346	0·703984(7)	0·70360	51·5	255	0·512402(4)	0·51194	0·9	1·1
ST206AI	56·4	1372	0·704729(7)	0·70377	60·2	318	0·512402(5)	0·51196	1·5	1·1
ST224B	38·4	932	0·704944(7)	0·70398	18·6	92·8	0·512375(8)	0·51191	0·5	1·2
ST226	62·9	1344	0·705013(10)	0·70392	49·8	270	0·512396(6)	0·51197	1·6	1·0
ST246A	70·2	1418	0·705594(7)	0·70443	39·6	181	0·512454(5)	0·51195	1·1	1·2
ST256	127	3296	0·707524(7)	0·70662	42·7	219	0·512435(5)	0·51198	1·9	1·1
Dol carbonatite										
L1	38·0	3355	0·704472(7)	0·70421	139	1690	0·512109(4)	0·51192	0·6	0·9
ST189	14·1	1870	0·704168(7)	0·70399	107	1040	0·512189(5)	0·51195	1·3	0·9
ST203	31·3	2015	0·705026(7)	0·70466	106	1030	0·512188(5)	0·51195	1·2	0·9
Dol–cal carbonatite										
ST126	85·4	1005	0·707782(7)	0·70579	23·3	167	0·512224(6)	0·51190	0·3	1·0
ST193A	21·8	3060	0·704094(7)	0·70393	29·0	185	0·512282(6)	0·51192	0·6	1·0
ST198C	19·4	5555	0·703967(7)	0·70389	100	607	0·512300(5)	0·51192	0·6	1·1
ST199	30·3	3427	0·704142(7)	0·70394	49·4	314	0·512295(5)	0·51193	0·8	1·0
ST231A	49·2	537	0·706439(7)	0·70429	31·2	159	0·512371(5)	0·51192	0·6	1·2

*Initial isotope ratios calculated for an emplacement age of 582 Ma.
†Initial ε_{Nd} values were calculated using ^{147}Sm decay constant of $6{\cdot}54 \times 10^{-12}$ year^{-1}; $(^{143}Nd/^{144}Nd)_{CHUR} = 0{\cdot}512638$ and $(^{147}Sm/^{144}Nd)_{CHUR} = 0{\cdot}1967$.
‡Depleted Mantle model ages [$T^{Nd}_{(DM)}$] were calculated using ^{147}Sm decay constant of $6{\cdot}54 \times 10^{-12}$ year^{-1}; $(^{143}Nd/^{144}Nd)_{DM} = 0{\cdot}513150$ and $(^{147}Sm/^{144}Nd)_{DM} = 0{\cdot}222$.
Numbers in parentheses are 2σ errors of the mean for individual isotope ratio measurements; elemental abundances are ICP-MS data.

ST231A (13·0‰ $\delta^{18}O$), which visibly experienced carbonate recrystallization, falls outside this narrow range. The dolomite carbonatites have the isotopically heaviest carbon composition, with $\delta^{13}C$ between −2·8 and −2·7‰ ($n = 2$). The oxygen isotope composition (10·8–11·5‰ $\delta^{18}O$) covers the higher end of the aillikite range, slightly elevated in comparison with the calcite-bearing carbonatites. There is no correlation between C and O isotope composition of carbonates from aillikite and carbonatite (Fig. 18), or between stable isotope and Sr–Nd isotope ratios. Damtjernites contain a composite carbonate fraction (groundmass and segregations), which is highly variable in its carbon isotope composition (–7 to −3‰ $\delta^{13}C$) at fairly constant

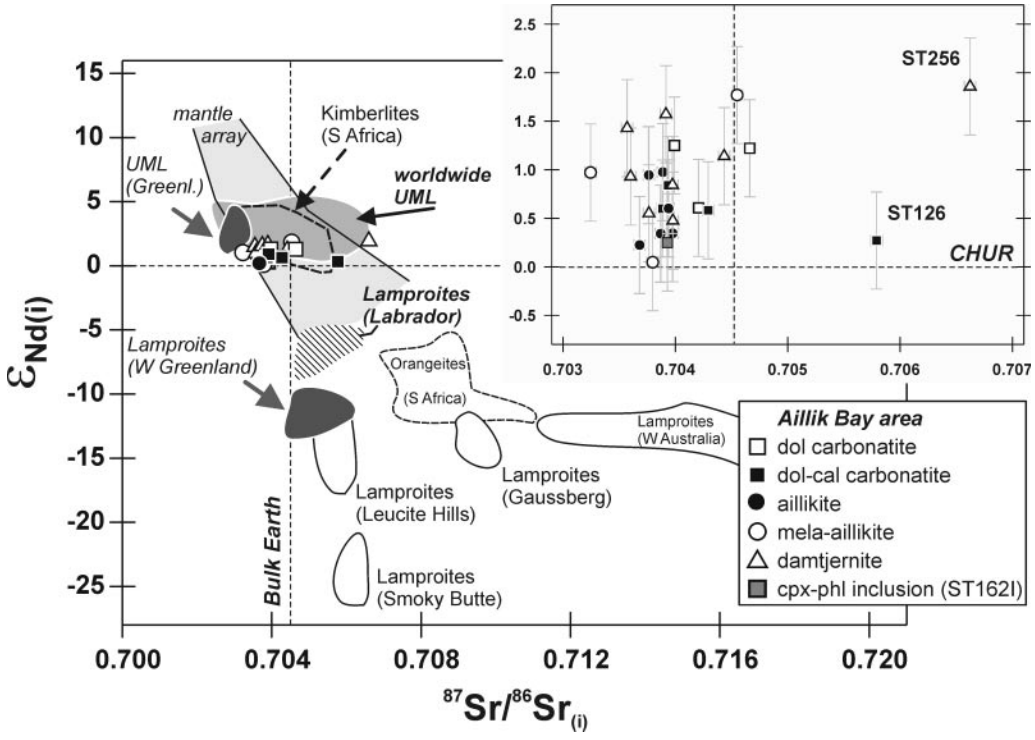

Fig. 17. $\varepsilon_{Nd(582)}$ vs $^{87}Sr/^{86}Sr_{(582)}$ for Aillik Bay area UML, carbonatites and cognate inclusion ST162I. The inset shows an enlarged portion of the Sr–Nd isotope space, with error bars being conservatively estimated using the $2\sigma_m$ error of the measured isotope ratios, a 35 Myr age uncertainty for undated samples, and a 5% (Rb/Sr) and 3% (Sm/Nd) uncertainty for the calculated parent/daughter ratios (ICP-MS data) used for the emplacement age correction of the isotope compositions. Fields for Greenland UML and lamproites (Nelson, 1989), Leucite Hills, Smoky Butte and Western Australia lamproites (Vollmer *et al.*, 1984; Fraser *et al.*, 1985), Gaussberg lamproites (Murphy *et al.*, 2002), South African kimberlites and orangeites (Nowell *et al.*, 2004) and other worldwide UML occurrences (Neal & Davidson, 1989; Beard *et al.*, 1996; Pearce & Leng, 1996; Le Roex & Lanyon, 1998; Andronikov & Foley, 2001; Riley *et al.*, 2003) are shown for comparison. The field for Labrador lamproites is based on the first author's unpublished data (1374 Ma lamproites from the Aillik Bay area; see text).

$\delta^{18}O$ between 9·9 and 11·4‰ (within the range of aillikites).

DISCUSSION

Field relations, age determinations and radiogenic isotope signatures imply that the various UML and carbonatite types as well as their micaceous cognate inclusions are broadly coeval and appear to be related to a common mode of magma production that persisted over a period of 30–35 Myr. To evaluate the petrogenesis of UML in the Aillik Bay area, it is necessary to unravel the effects of low-pressure modification of the primary magma, thus clearing the way for constraining the nature of the magma source, assessing whether all UML types can be related to a common magma type, and considering the geodynamic conditions under which melting occurred.

Modification of the parental UML magma

Role of contamination and fractionation processes

Extensive interaction of the UML magma with continental crustal material can be ruled out by the strong Si and Al undersaturation, high Ce/Pb ratios (>25), positive $\varepsilon_{Nd(582)}$ values and fairly unradiogenic Sr isotope composition ($^{87}Sr/^{86}Sr_{(582)}$ typically <0·7045). The continental crust of the North Atlantic craton is characterized by extremely unradiogenic Nd and radiogenic Sr isotope compositions and therefore cannot have modified the primary UML magma (e.g. Makkovik Province gneisses $\varepsilon_{Nd(582)} \sim -30$; Saglek block gneisses $^{87}Sr/^{86}Sr_{(582)}$ >0·73; Collerson *et al.*, 1989; Kerr & Fryer, 1993). There is no correlation between UML/carbonatite isotope composition and chemical parameters such as Si, Al, K and Pb, which are typically elevated in continental crustal rocks.

Fine-grained microporphyritic aillikites with high Mg-numbers, and high Ni and Cr contents meet the criteria for near-primary mantle-derived magmas (Frey *et al.*, 1978); Mg-number >68 and Ni >320 ppm. Furthermore, they resemble experimentally produced 'higher-degree' melts of synthetic carbonated garnet peridotite in the simple CMAS–CO_2 system close to 5 GPa (Fig. 19; Gudfinnsson & Presnall, 2005). It should be noted that the accumulation of olivine macrocrysts typical of kimberlites (Mitchell, 1986) is seen in only

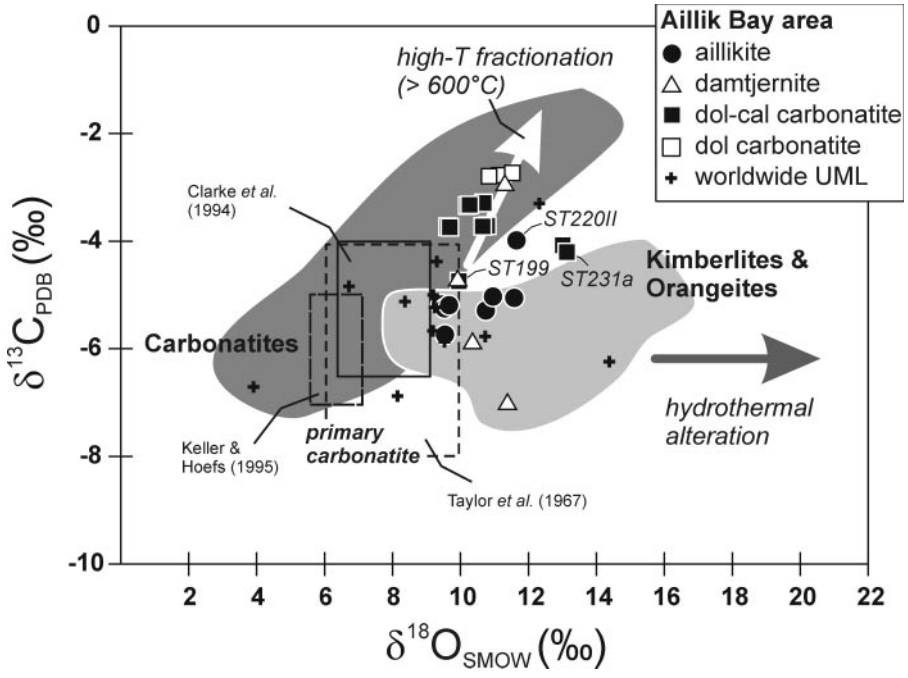

Fig. 18. Carbon and oxygen isotope composition (expressed as ‰ $\delta^{13}C$ and $\delta^{18}O$ relative to PDB and SMOW, respectively) of bulk-rock carbonate fractions from the Aillik Bay area ultramafic lamprophyres and carbonatites. Two main petrogenetic processes (hydrothermal alteration and high-*T* fractionation) that have the potential to change the stable isotope composition are illustrated by arrows (after Deines, 1989). Fields for typical carbonatite (dark grey) and kimberlite (pale grey) compositions are compiled from worldwide occurrences (data sources are available from the first author upon request). Data for worldwide UML are from the same sources as in Fig. 17. Symbol size is larger than the 2σ error.

few aillikite samples (L2, ST225) and is not considered significant.

Our field observation that carbonatites, aillikites and mela-aillikites are intimately related is supported by the strong compositional continuum in Si, Ti, Al, Ca, Mn, P, CO_2, Cr, Ni, Nb and LREE contents. On variation diagrams, they define well-correlated trends from which damtjernites are typically displaced (Figs 13–15). These trends are controlled principally by a relative separation of carbonate and a 2:1 to 1:2 mix of olivine and phlogopite (Figs 13 and 19a). The most likely process is devolatilization of CO_2-rich liquids/fluids from aillikite magma, which caused the compositional shift to either side of these trends with carbonatite and mela-aillikite being close to the separated end-members (see section on devolatilization).

Damtjernites cannot be interpreted unequivocally as near-primary magmas using the criteria of Frey *et al.* (1978), although these are based on melts being in equilibrium with dry peridotite and not with metasomatized source materials. The most primitive olivine-rich members approach 'primary' Mg-number, Ni and Cr contents, but more evolved types are almost olivine-free, resulting in a conspicuous bimodal distribution in terms of MgO, Ni and Cr content (Fig. 14). The cumulate textures formed by large subhedral olivine and rare composite clinopyroxene crystals within the fine-grained groundmass imply that these may represent cognate high-pressure phases. Clinopyroxene crystallization pressure ranges between 0·8 and 1·5 GPa (Nimis & Ulmer, 1998), similar to the estimates for the clinopyroxene-bearing cognate inclusions. An unrealistically high amount (~30–40 wt %) of olivine removal (D_{MgO} = 2·6; D_{Ni} = 4·9–6·5; following Herzberg & O'Hara, 2002), together with minor amounts of Cr-spinel, would be required to relate these two groups of damtjernites (Fig. 14b), which have an identical olivine-free groundmass. On the basis of the large damtjernite sample suite examined (n = 35), we can rule out a continuous fractionation series, leading us to favour a role for a silicate–carbonate unmixing process in their petrogenesis (see section on immiscibility).

Major and selected trace element variation diagrams show no gradation between aillikites and damtjernites (Figs 13 and 14), implying that they experienced different evolutionary histories (Fig. 19). There is no petrologically sound mineral assemblage that could relate the two contrasting rock types by crystal fractionation. Fractional crystallization of olivine and Cr-spinel, however, can account for some of the intra-group variation in aillikites and damtjernites, as illustrated by the distinct Ni and Cr vs MgO trends (Fig. 14).

Table 14: Bulk-rock carbonate C and O isotope composition of Aillik Bay area UML and carbonatites

Sample no.	$\delta^{13}C_{PDB}$ (‰)	$\delta^{18}O_{SMOW}$ (‰)
Aillikite		
L60	−5·7	9·5
ST109	−5·3	10·7
ST164	−5·2	9·4
ST164repl.1	−5·3	9·5
ST164repl.2	−5·2	9·7
ST220II	−4·0	11·6
ST250A	−5·0	11·0
ST250Arepl.1	−5·1	11·6
Damtjernite		
ST188A	−7·0	11·4
ST206AI	−4·7	9·9
ST226	−5·9	10·4
ST246A	−3·0	11·3
Dol carbonatite		
L1	−2·8	11·1
L1repl.1	−2·7	11·5
ST203	−2·8	10·8
Dol–cal carbonatite		
ST126	−3·3	10·2
ST126repl.1	−3·3	10·7
ST126repl.2	−3·3	10·3
ST127	−3·7	9·6
ST127repl.1	−3·7	9·7
ST198C	−3·7	10·8
ST198Crepl.1	−3·7	10·7
ST199	−4·8	10·0
ST199repl.1	−4·7	10·0
ST231A	−4·1	13·0
ST231Arepl.1	−4·2	13·2

repl.1 and repl.2 indicate replicate analyses.

Linking aillikites, mela-aillikites and carbonatites by a devolatilization process

Several lines of evidence indicate that the two distinct types of carbonatite occurring at Aillik Bay do not represent primary magma compositions. The dolomite carbonatite would be the more likely candidate for a primary magma composition (Sweeney, 1994; Harmer & Gittins, 1997; Lee & Wyllie, 1998), but its Fe-rich dolomite is highly evolved in terms of Fe/Mg distribution. Furthermore, the conspicuous lack of mafic silicate phases such as olivine and phlogopite, in combination with the granular texture and the extremely fractionated incompatible element distributions, indicate that the dolomitic carbonatites cannot represent liquids (Wyllie & Tuttle, 1960), but are more probably the product of a carbonate fluid extraction process.

In contrast, the presence of calcite and dolomite laths in the mixed carbonatites indicates that they crystallized from a liquid. Although the analyzed dolomite–calcite carbonatite and aillikite samples were collected from discrete subvertical dykes, lateral gradations between both rock types within single sills (Fig. 3) have been described from Cape Makkovik (Malpas *et al.*, 1986; Foley, 1989*a*). Field relations imply that the carbonatite phase of the flat-lying sheets may represent a separated carbonatite liquid with associated fluid that was moving ahead of the more viscous silicate-rich aillikite magma, opening fissures during dyke or sill emplacement. Additional support for such a devolatilization process comes from the fluidized globular aillikite segregations (Fig. 5a), which clearly demonstrate that a CO_2-rich liquid/fluid was expelled from the aillikite magma. The subordinate phlogopite with 'aillikitic' composition in dolomite–calcite carbonatites is best interpreted as being incorporated from the aillikite parent magma during flowage and disruption (Fig. 8a). However, the Al_2O_3-rich clinopyroxene phenocrysts (Fig. 9a), which do not occur in aillikites, seem to have crystallized from the separated carbonatite liquid, as carbonatites show a high potential to promote the Ca-Tschermaks component in clinopyroxene (Blundy & Dalton, 2000).

Our stable isotope results are consistent with a fractionation relationship between aillikite and carbonatite. Groundmass carbonate from type aillikite is isotopically the most 'primitive', straddling the compositional fields for primary mantle-derived carbonatite (Taylor *et al.*, 1967; Clarke *et al.*, 1994) in a conventional $\delta^{13}C_{PDB}$–$\delta^{18}O_{SMOW}$ diagram (Fig. 18). The carbonatites contain isotopically heavier carbon than the aillikites with an increase in $\delta^{13}C$ from aillikite through dolomite–calcite carbonatite to dolomite carbonatite of the order of ~3‰, so that they fall outside the fields for primary carbonatite (e.g. Keller & Hoefs, 1995). Post-magmatic processes have been shown to have only little effect on the C isotopic composition, but may produce major changes in O isotopes (Deines, 1989; Santos & Clayton, 1995), which is not seen in the Aillik Bay samples (except for carbonatite ST231A).

The identical 'mantle-like' Sr–Nd isotope composition of aillikites and carbonatites (Fig. 17) suggests that their distinct carbon isotope composition (Fig. 18) does not reflect derivation from different sources, and also that hydrothermal alteration did not play a major role, as most of the Sr resides in the carbonates. Rayleigh fractionation of a common parent magma best explains the strong ^{13}C enrichment seen from aillikites towards dolomitic carbonatites. This may be caused by release of a CO_2-rich liquid/fluid (enriched in ^{13}C; Mattey *et al.*, 1990; Chacko *et al.*, 1991; Deines, 2004) by diffusive

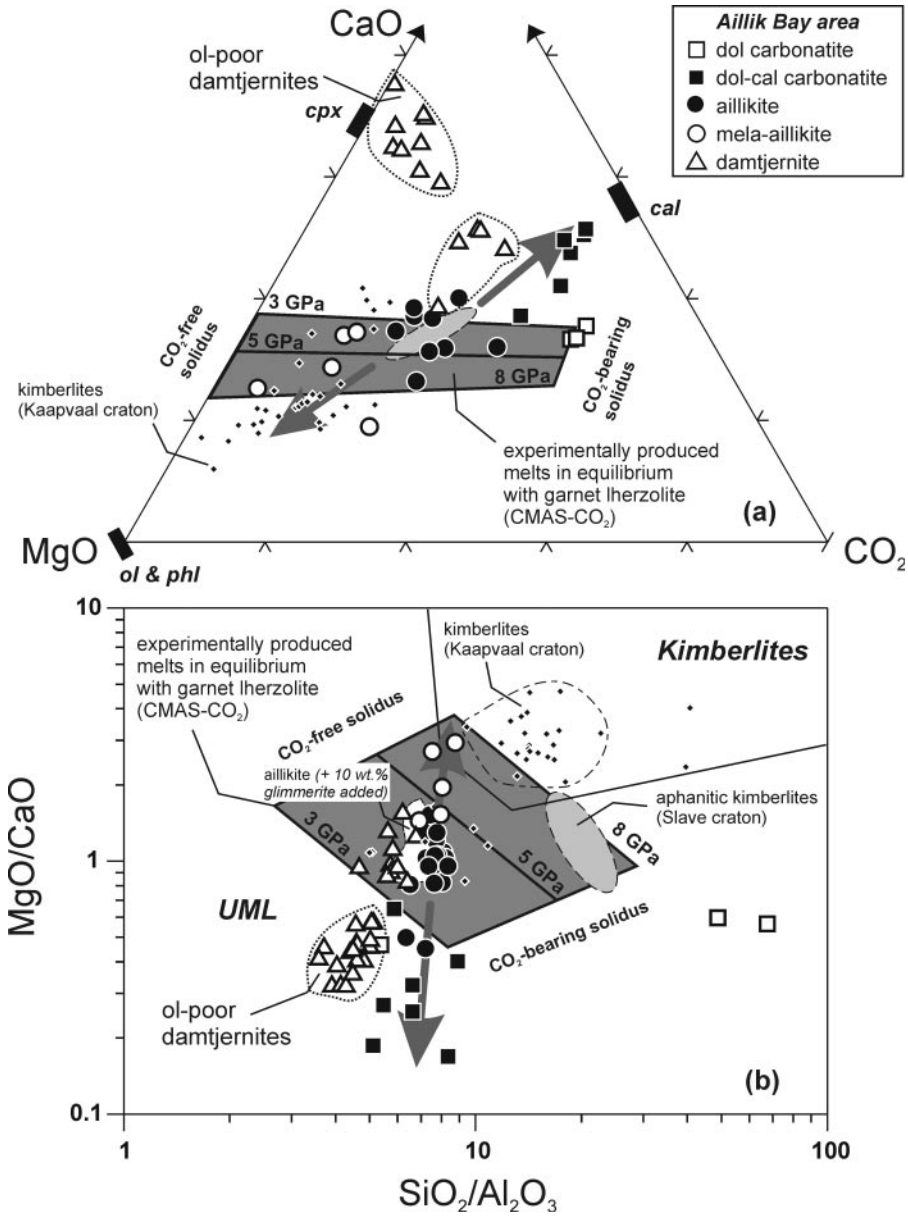

Fig. 19. Aillik Bay area UML and carbonatites in (a) CaO–MgO–CO_2 wt % space, and (b) in the MgO/CaO vs SiO_2/Al_2O_3 'UML–kimberlite discrimination diagram' of Rock (1991). Shaded fields of experimentally determined melt compositions after Gudfinnsson & Presnall (2005). Arrows indicate evolutionary paths from aillikite towards mela-aillikite and dolomite–calcite carbonatite caused by devolatilization. Compositional range (black bars) of calcite (cal), olivine (ol), phlogopite (phl) and diopside-rich clinopyroxene (cpx) is shown in (a). Small filled diamonds represent hypabyssal kimberlites from Kimberley, Kaapvaal craton (South Africa, Le Roex *et al.*, 2003) and the light grey ellipse indicates compositions of aphanitic hypabyssal kimberlites from the Jericho pipe, Slave craton, Canada (Price *et al.*, 2000). The white field in the centre of (b) shows aillikite compositions corrected for 10 wt % glimmerite loss as proxy for a 'proto-aillikite' composition.

separation from carbonate-rich aillikite magma as a result of near-surface decompression at high temperature (>600 °C). This liquid plus associated fluid moved ahead of the crystal- and inclusion-laden aillikite magma and opened cracks for UML dyke emplacement. It eventually crystallized to form ^{13}C-enriched dolomite–calcite carbonatite and rare dolomite carbonatite preferentially at UML dyke terminations. Co-precipitation of calcite and dolomite has been experimentally demonstrated to occur from 880 °C down to 650 °C at 0·2 GPa in the CMS–CO_2–H_2O system (Otto & Wyllie, 1993) with an expanded dolomite stability field at low temperatures.

Quantifying this Rayleigh fractionation process [the fractionation factor at 1200° C was calculated using equation (4) of Deines (2004)], a typical aillikite sample (e.g. ST164) would have to release <70 vol. % of its

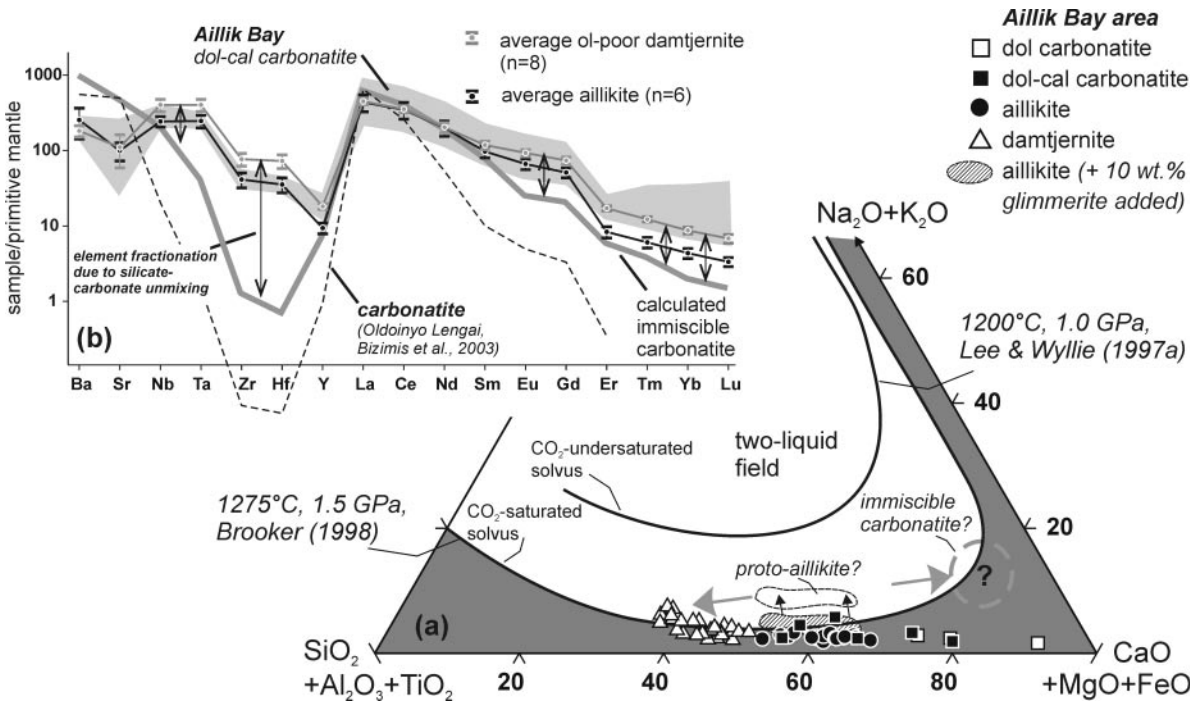

Fig. 20. Illustration of a likely role for liquid immiscibility in the genesis of damtjernites. (a) Aillik Bay UML and carbonatite compositions in a multicomponent system projected from CO_2. The small diagonally shaded field represents 'proto-aillikite' compositions corrected for 10 wt % 'glimmerite' loss during magma ascent. These high-pressure aillikite equivalents may thus fall into a CO_2-saturated two-liquid field (black arrows) at uppermost mantle conditions (see solvus of Brooker, 1998) and exsolve damtjernite and calciocarbonatite liquids (grey arrows). (b) Expected trace element distribution between average damtjernite and its hypothetical conjugate carbonatite liquid using partition coefficients from Veksler *et al.* (1998), except for Eu, Gd, Yb, Lu (Hamilton *et al.*, 1989) and Ce (Jones *et al.*, 1995). The transitional composition of average aillikite demonstrates the potential of proto-aillikite magma for representing the parental magma that underwent silicate–carbonate immiscibility. Primitive mantle composition is after Sun & McDonough (1989).

carbonate fraction to cause an increase in $\delta^{13}C$ by >2‰, approaching observed values for the carbonatites. This amount of separated CO_2-rich liquid plus fluid would leave a residual magma (carrying early olivine and phlogopite phenocrysts) that on further cooling crystallizes a groundmass assemblage resembling mela-aillikite (Fig. 5b and Fig. 5c), which contains abundant clinopyroxene, biotite, and Mg- and Mn-depleted spinels/ilmenites (Figs 8a, 9a and 10a), but <10 vol. % carbonate. This model is consistent with the occurrence of composite aillikite/carbonatite and aillikite/mela-aillikite dykes, further implying that this fractionation process operated at shallow intrusion levels.

A role for liquid immiscibility in the genesis of damtjernites?

Fractional crystallization and partial melting cannot relate the distinct mineral assemblage and chemical composition of contemporaneous and isotopically indistinguishable aillikites and damtjernites, leading us to invoke an unmixing process. Although immiscible silicate–carbonate liquids have been reported from natural mantle-derived xenoliths (Amundsen, 1987; Kogarko *et al.*, 1995; Chalot-Prat & Arnold, 1999; van Achterbergh *et al.*, 2004), they have been experimentally produced predominantly at crustal pressures. (Freestone & Hamilton, 1980; Kjarsgaard & Hamilton, 1989; Kjarsgaard *et al.*, 1989; Lee & Wyllie, 1997*a*, Lee & Wyllie, 1997*b*). One of the major findings of these experiments was that primitive CO_2-bearing mantle-derived alkaline magmas do not intersect the miscibility gap and that only their evolved derivatives approach the silicate limb of the solvus.

Aillikite and damtjernite are unlikely to represent conjugate liquids given their rather small compositional differences (Fig. 13). It is more reasonable to consider an intermediate role for aillikite magma as the carbonated silicate parent that underwent immiscibility, but aillikite compositions do not fall in any published experimentally determined silicate–carbonate miscibility gaps (Fig. 20a), which mainly deal with nephelinitic systems (e.g. Lee & Wyllie, 1997*a*). However, fairly large miscibility gaps have been found in a CO_2-saturated SNAC–CO_2 system between ~1225–1325 °C at 1·5–2·5 GPa (Fig. 20a; Brooker, 1998; Brooker & Kjarsgaard, in preparation). Although damtjernites fall along the 1275 °C/1·5 GPa immiscibility solvus, aillikite compositions seen at the

surface are too alkali poor to enter the miscibility gap. However, it is reasonable to assume that a 'transitional' magma type such as aillikite has reacted with uppermost mantle wall-rocks (Moore & Wood, 1998), thereby losing alkalis; thus, the high-pressure equivalents may lie in the miscibility gap (Fig. 20a). The glimmerite nodules, which are present in every aillikite dyke examined, may provide a link to a more alkaline proto-aillikite magma that was able to exsolve a damtjernite liquid and a conjugate calciocarbonatite liquid.

Although sövitic carbonatites have not been found during our recent field work, two calciocarbonatite dykes were reported by Hawkins (1977) and Foley (1982) from Aillik Bay. Their apparent scarcity is probably due to the fact that access to the radial dyke swarm is limited to its southern periphery and the centre of a hypothetical complex, where sövites may be more common, is covered by the sea (Fig. 2). Examples for UML–carbonatite complexes with such a central sövitic core are the Fen (Andersen, 1988; Andersen & Austrheim, 1991; Dahlgren, 1994) and Alnö complexes (Kresten, 1980; Vuorinen & Skelton, 2004) in Scandinavia, and the Callander complex in Ontario (Ferguson & Currie, 1971).

Proto-aillikite magma may have started to line the conduits with glimmerite material causing a loss of alkalis, Si, Al and Mg thereby lowering Mg/Ca but elevating Si/Al in the melt (Figs 19b and 20a). These subtle but critical compositional modifications (see Lee & Wyllie, 1997*a*) may have prevented the derivative magma from approaching the miscibility gap (Fig. 20a), allowing its direct ascent to the surface as glimmerite-laden aillikite. However, proto-aillikite magma that moved through previously reaction-lined conduits did not lose appreciable alkalis, so that it could not escape the unmixing process described above (Fig. 21a). Unmixing can explain the observation that phlogopite phenocrysts in aillikite and damtjernite have similar core compositions derived from common magmas, but later follow contrasting evolutionary paths (Fig. 8a and b). Moreover, the high NiO content (up to 0·5 wt %; Fig. 7) of early damtjernite olivines ($<Fo_{86}$) indicates that immiscible damtjernite separation from proto-aillikite magma occurred when the latter was already slightly evolved but still alkali-rich, because olivines crystallized from strongly alkaline melts have exceptionally high D_{Ni} (Foley & Jenner, 2004).

Trace element modelling is also consistent with the proposed relation between damtjernite and aillikite by liquid immiscibility. Using partitioning data determined for nephelinitic systems at pressures of up to 1 GPa (Hamilton *et al.*, 1989; Jones *et al.*, 1995; Veksler *et al.*, 1998), we have calculated the budget of crucial trace elements for a hypothetical carbonatite magma conjugate to damtjernite (Fig. 20b). These trace element distributions resemble those of immiscible carbonatites (e.g. Oldoinyo Lengai; Bizimis *et al.*, 2003), and the trace element abundances of aillikites are indeed transitional between the damtjernite and carbonatite conjugate pairs. This demonstrates that a proto-aillikite magma could have been the parental liquid to damtjernite, and that trace element partitioning between immiscible carbonate–silicate liquids can fully account for the observed differences in the large ion lithophile element (LILE), HFSE and HREE budget of rock types (Figs 16b and 20b).

Petrogenetic significance of cognate inclusions in aillikites

The mineralogy of clinopyroxene–phlogopite and olivine–phlogopite inclusions in aillikites resembles both aillikites (e.g. Mg-ilmenite, Cr-spinel) and damtjernites (e.g. Ti-Al-rich clinopyroxene, titanite), but also shows individual peculiarities (e.g. high Mn-olivine, zirconolite). These inclusions may be genetically related, representing different components in a continuum of compositions. The constituent minerals seem to have crystallized from a highly alkaline, carbonated silicate melt (isotopically similar to aillikite and damtjernite) at uppermost mantle to lower crustal depths (25–45 km). The presence of a CO_2-rich phase is witnessed by the common replacement of olivine by carbonate. A cumulate origin is also indicated by the banded structure of larger nodules. It is likely that this material lines the conduits of the alkaline intrusions beneath Aillik Bay (Fig. 21a) and was disrupted by later batches of carbonate-rich aillikite magma. The parental magma to these nodules presumably never reached the surface, but clearly shows UML affinity. This multistage model, which is broadly similar to the suggested origin for phlogopite clinopyroxenite nodules in the high-K lavas of western Italy (Giannetti & Luhr, 1990), is consistent with the 35 Myr time span (~590–555 Ma) of Aillik Bay area UML magmatism.

Glimmerites are probably the product of a similar wall-rock coating process, but there are strong indications that they are genetically related to carbonate-rich proto-aillikite. Whereas clinopyroxene–phlogopite and olivine–phlogopite nodules are in equilibrium with their host aillikite magma regarding volatile fugacities (see also similar mica compositions; Fig. 8), the distinctively higher relative HF fugacity of phlogopite–apatite pairs in glimmerites (Fig. 12), combined with the observation that glimmerite phlogopite coexists with pure orthoclase, suggests that glimmerites crystallized in CO_2-rich, but H_2O-poor conditions.

Mantle source characteristics and melting processes

Identification of the parental UML magma

Amongst the UML rock types from Aillik Bay, aillikite is considered to be closest to a primary magma

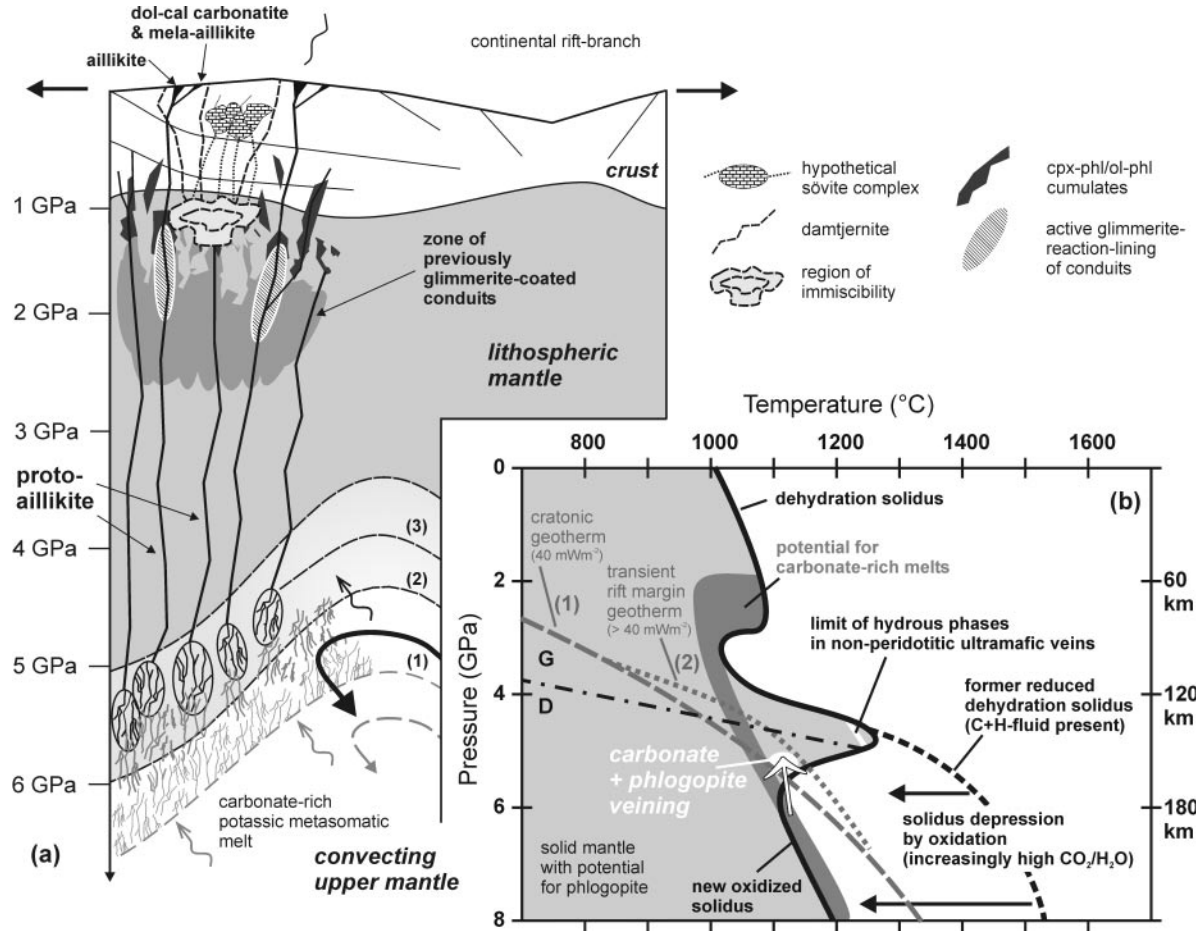

Fig. 21. Petrogenetic model for the Aillik Bay UML and carbonatites formed between ~590 and 555 Ma in response to lithospheric extension and thinning. (a) The dashed lines labelled (1)–(2)–(3) in the geological cross-section denote time-steps of progressive conversion of lithospheric mantle by hotter upwelling convective mantle. Metasomatic carbonate–phlogopite-dominated veins formed at the base of the cold lithosphere and were successively remelted together with the surrounding garnet peridotite during progressive convective mantle upwelling. The resultant parental proto-aillikite magma was partly modified by low-pressure processes at uppermost mantle to crustal depths giving rise to the variety of UML and carbonatite types of the Aillik Bay intrusive suite. (b) Pressure–temperature diagram illustrating carbonate–phlogopite vein formation and remelting as a result of solidus depression and a changing geotherm (from 1 to 2) during incipient lithosphere replacement by convective mantle material (modified after Foley *et al.*, 2002). See text for further explanation. Solidi of pyrolitic mantle for reduced H_2O-undersaturated (dehydration solidus, C + H-fluid present) and oxidized CO_2-bearing conditions are taken from Green & Falloon (1998). Geotherms are from Pollack & Chapman (1977), and graphite (G)–diamond (D) stability curve is from Kennedy & Kennedy (1976). Upper thermal stability limit of hydrous phases (i.e. phlogopite, white line) in non-peridotitic ultramafic vein assemblages after Foley *et al.* (1999).

composition. In contrast, damtjernites have many non-primary features, so we do not consider them during subsequent discussions on mantle processes. Aillikite is the only rock type carrying centimetre-sized cognate inclusions (Fig. 5e) testifying to rapid magma ascent, although mantle peridotite xenoliths have not been found.

Compositional modification by crystallization of glimmerite presumably at uppermost mantle levels caused only small deviations from primary compositions (Fig. 19b). Recalculation of aillikite sample ST164 to correct for a loss of up to 10 wt % glimmerite material (95 : 5 ; phlogopite:apatite) would lower SiO_2 (1·5 wt %), K_2O (0·8), Al_2O_3 (0·5) and MgO (0·5) but elevate CaO (1·5) and FeO (0·6) relative to the hypothetical proto-aillikite magma.

Constraints on the mineralogy and location of the source region

The high MgO and CO_2 content, as well as the potassic nature of aillikite, has to be explained in terms of partial melting of a carbonate-rich peridotitic source with an essential contribution from a K-bearing phase. Partial melting can be expected to have occurred under pressures greater than 5 GPa, but presumably not much greater than 7 GPa, as indicated by the rare occurrence of diamonds in aillikites from the North Atlantic region

and by the equilibration pressures of entrained lithospheric mantle peridotite xenoliths (Larsen & Rønsbo, 1993; Mitchell *et al.*, 1999; Digonnet *et al.*, 2000; Bizzarro & Stevenson, 2003; Griffin *et al.*, 2004). High-pressure melting experiments by Dalton & Presnall (1998) and Gudfinnsson & Presnall (2005), conducted on synthetic carbonated peridotite material (CMAS–CO_2 system), are the only studies available that may be applicable to the genesis of aillikite, although important components such as alkalis, H_2O, FeO and TiO_2 are lacking. Indeed, those workers have produced near-solidus carbonate-rich liquids between 3 and 8 GPa that resemble primary carbonatites, and carbonate-rich ultramafic magmas such as aillikite and kimberlite at slightly higher degrees of melting. The most primitive aillikites from Aillik Bay resemble those melts that segregated significantly above the carbonate-bearing solidus close to 5 GPa in the Gudfinnsson & Presnall (2005) experiments (Fig. 19). However, it must be stressed that the co-occurrence of aillikite and carbonatite at Aillik Bay cannot be interpreted in terms of a melting continuum; instead they are related by a low-pressure fractionation process (Fig. 19).

The high MgO and Ni content of aillikite requires a major contribution from an olivine-rich peridotitic mantle. Furthermore, the strong LREE/HREE fractionation of aillikites at very low HREE concentration levels can be explained only in terms of melting in the presence of residual garnet. The abundant carbonate in aillikite is isotopically consistent with mantle derivation ($\delta^{13}C \sim -5$, Deines, 2002) and bulk-rock CO_2 correlates positively with CaO (Fig. 15b), but not with MgO, an observation also made for many kimberlites (Bailey, 1984). This implies that the mantle carbonate that contributed to the aillikite magma was $CaCO_3$ rather than dolomite or magnesite, although peridotite melting at >5 GPa must have occurred in the magnesite stability field (Brey *et al.*, 1983). Given that the most primitive aillikites have MgO/CaO ratios between 1 and 1·3 (Fig. 19b), much lower than in experimentally produced near-solidus melts of magnesite-bearing peridotite (up to 25; Brey *et al.*, 1983), calcite is the most likely source of the carbonate at the P–T conditions of cratonic mantle lithosphere (Biellmann *et al.*, 1993), but only as part of a non-peridotitic vein assemblage at 4–7 GPa.

Aillikite magma clearly segregated from a mantle source that contained an early melting hydrous K-bearing phase. Phlogopite and K-richterite are known from metasomatized mantle assemblages (Dawson & Smith, 1977; Waters, 1987; Ionov & Hofmann, 1995; Grégoire *et al.*, 2002, 2003), both being stable to pressures above 7 GPa (Sudo & Tatsumi, 1990; Foley, 1991; Konzett *et al.*, 1997; Konzett & Ulmer, 1999). Phlogopite is considered the most likely K-bearing phase in the melting assemblage because of its potential to produce silica-undersaturated melts with extremely high K/Na ratios. In contrast, K-richterite was demonstrated to melt out close to the solidus of ultramafic assemblages, yielding SiO_2-rich melt compositions that are more akin to lamproites (Foley *et al.*, 1999). The impact of residual source phlogopite on the incompatible element patterns of aillikites (Fig. 16a) is clearly seen at the pronounced troughs at K and Rb, but not for Cs owing to a D_{Cs} (0·6) that is an order of magnitude lower than D_{Rb} (5·2; Foley *et al.*, 1996). Ba is strongly scattered and less meaningful for evaluating the role of phlogopite in the presence of mantle carbonate. Because K is a stoichiometric component in phlogopite, its content in the melt will be near-constant as long as phlogopite is residual, varying mainly as a function of the proportion to which phlogopite enters the melt. The K content of a melt in equilibrium with mantle phlogopite that melts to an extent of ~20–50% (Greenough, 1988) is ~1·6–5 wt %. The average K content of aillikite (1·8 ± 0·3 wt %) is at the lower end of this range, which is consistent with lower K-saturation levels in undersaturated melts produced under CO_2-rich conditions (Rogers *et al.*, 1992). Alternatively, proto-aillikite might have lost up to 1 wt % K_2O by wall-rock coating with glimmerite material.

Apatite is an essential constituent of the source region given the high P_2O_5 concentrations in aillikite (2·2 ± 0·7 wt %; Fig. 13). The imprint of residual apatite on the incompatible element patterns may be seen at the Sr–P trough and probably at the U spike (Fig. 16a) given its potential for fractionating Th (D_{Th} ~0·12) from U (D_U ~0·001; Klemme & Dalpe, 2003).

Although the comparably high TiO_2 (3·4 ± 0·5 wt %) concentrations of aillikite can be explained by melting Ti-rich phlogopite, it is more likely that an early melting Ti-rich oxide phase, probably ilmenite, controlled the HFSE budget during melting given the extremely high Nb–Ta abundances (181 ± 28 ppm Nb). Melting experiments on non-peridotitic ultramafic vein assemblages showed that ilmenite melts out quickly, whereas rutile persists, as does apatite, to higher temperatures (Foley *et al.*, 1999). This observation makes ilmenite the more likely titanate that was present in the aillikite magma source region. Interestingly, the relative Zr–Hf depletion in aillikites is decoupled from Ti and Nb–Ta (Fig. 16a) and, therefore, unlikely to be the effect of a residual titanate. The relatively low but variable Zr–Hf concentrations in aillikite are not caused by mantle source carbonate, which is typically depleted in Zr and Hf (Ionov, 1998; Moine *et al.*, 2004), as there is no negative correlation between absolute Zr–Hf abundances and aillikite/carbonatite CO_2 content (Fig. 15a). A residual Ti-free oxide phase such as baddeleyite, which was found as mantle xenocrysts in the Ile Bizard alnöite (Heaman & LeCheminant, 2001) and has been synthesized as part of

a carbonate-bearing metasomatic vein assemblage under upper mantle conditions by Meen *et al.* (1989), can account for the observed Zr–Hf troughs in the aillikite trace element spectra (Fig. 16a). The likely presence of residual baddeleyite in the melting assemblage, buffering Zr and Hf in the melt, is not expected to have significantly affected the melt REE distribution given its relatively low REE concentrations (Reischmann *et al.*, 1995) and baddeleyite/carbonatite melt LREE to middle REE (MREE) partition coefficients close to unity (Klemme & Meyer, 2003).

An important constraint on the location of the mantle source region comes from the thermal stability of the required source mineralogy. We have pointed out that phlogopite and carbonate are essential in the melting assemblage and both phases are not stable at the temperatures of convecting upper mantle (~1480 °C; McKenzie & Bickle, 1988). They are stable at the *P–T* conditions of the cold mantle lithosphere (Wendlandt & Eggler, 1980; Mengel & Green, 1989; Sweeney *et al.*, 1993; Dalton & Wood, 1995; Ulmer & Sweeney, 2002) and this restricts aillikite generation to lithospheric portions of the cratonic mantle (<1400 °C; McKenzie *et al.*, 2005). It does not, however, rule out a contribution from the convecting asthenospheric upper mantle in the form of metasomatizing agents (Fig. 21a). We favour a veined lithospheric mantle source over pervasively metasomatized peridotite for the genesis of aillikite, as it can account for the occurrence of minerals that are not in equilibrium with peridotite.

Isotopic constraints on the age and style of mantle metasomatism

The Nd isotope composition of aillikites, close to present-day Bulk Earth (Fig. 17), does not advocate a long-term enrichment of the UML mantle source in incompatible trace elements. LREE enrichment must have occurred shortly prior to melting, without subsequent aging to produce negative ε_{Nd} values. Calculated Nd model ages of 1·0–1·1 Ga (based on Sm/Nd in aillikites) indicate the maximum LREE extraction age from a depleted mantle reservoir, because the Sm/Nd of a melt is generally lower than that of its source. Thus, it seems likely that the enrichment event did not precede Late Neoproterozoic UML magmatism by more than ~400 Myr (probably much less), which is at least 300 Myr after the Mesoproterozoic lamproite magmatism had occurred in this region (~1374 Ma; Tappe *et al.*, in preparation).

The Sr–Nd data from Aillik Bay UML samples define a horizontal array (Fig. 17), which may be explained by enhanced radiogenic Sr in-growth in the source region because of the extremely high Rb/Sr ratios of phlogopite concentrated in veins, whereas there is no phase present that could cause such a rapid change of the Nd isotope composition. If representative Rb and Sr concentrations for mantle phlogopites (45–300 and 14–175 ppm, respectively; Grégoire *et al.*, 2003) are considered, then only ~50–200 Myr would be needed to alter an initial asthenospheric $^{87}Sr/^{86}Sr$ ratio of 0·7029 (Zindler & Hart, 1986) to the maximum values measured for the Aillik Bay UML (0·7066). Such a 'phlogopite signature' can, therefore, be produced within only a few tens of million years prior to magmatism and has been reported from other UML and olivine melilitite occurrences (Rogers *et al.*, 1992; Andronikov & Foley, 2001; Riley *et al.*, 2003). The fact that carbonatites follow the Nd–Hf mantle array led Bizimis *et al.* (2003) to conclude that their carbonated mantle source regions underwent rapid remelting given the potential of mantle carbonate to produce radiogenic Hf while leaving Nd isotopes unaffected. Taken together, this reinforces our argument that the metasomatic carbonate–phlogopite assemblage that gave rise to the production of Late Neoproterozoic UML magmas was short-lived and presumably formed a vein network at the base of the cratonic lithosphere (Fig. 21).

PETROGENESIS OF PARENTAL AILLIK BAY UML MAGMA AS PART OF THE NORTH ATLANTIC ALKALINE PROVINCE

A number of rifting episodes affected the cratonic North Atlantic region during Middle to Late Proterozoic times and eventually led to the opening of the Iapetus Ocean and the break-up of the supercontinent Rodinia. Associated alkaline and carbonatitic igneous activity occurred from the St. Lawrence Valley Rift system (Gittins *et al.*, 1967, 1975; Doig & Barton, 1968; Ferguson & Currie, 1971) to Scandinavia (Griffin & Taylor, 1975; Brueckner & Rex, 1980; Kresten, 1980; Dahlgren, 1994; Meert *et al.*, 1998; O'Brien *et al.*, 2005), with the Aillik Bay UML suite forming an integral part of this North Atlantic alkaline province (Doig, 1970). Deep melting events at around 1400–1200 Ma produced lamproites, and can be placed within intact long-term enriched subcontinental lithospheric mantle (strongly negative ε_{Nd} and highly unradiogenic Pb; Nelson, 1989; Tappe *et al.*, in preparation), whereas the widespread Late Neoproterozoic UML magmas (~600–550 Ma), such as those from Aillik Bay, show an imprint from juvenile asthenosphere-derived material (positive ε_{Nd} coupled to incompatible trace element enrichment). This indicates that progressive continental stretching resulted in an incipient protrusion of hotter asthenosphere to shallow levels beneath the fractured continental margins (Fig. 21a). As a result of this lithospheric

thinning, the cratonic geotherm was displaced to higher temperatures more similar to that of rift margins (Thompson & Gibson, 1994). Additionally, a depression of the former cratonic lithosphere solidus by volatile fluxing and oxidation (Foley, 1988; Taylor & Green, 1988) within the rifted mantle triggered small-degree melting under CO_2-bearing conditions (Fig. 21b). The depth interval of initial CO_2-present melting in the upwelling asthenosphere is considered to have been in excess of 5 GPa given the potential presence of diamonds in the overlying cratonic lithosphere. The small melt fraction produced had carbonatite-like characteristics (Wyllie, 1980; Dalton & Presnall, 1998) and during ascent quickly encountered the cold base of the cratonic lithosphere where the melts solidified because of their low heat capacity (Spera, 1984, 1987; McKenzie, 1989; Meen *et al.*, 1989) producing carbonate-phlogopite dominated veins with minor apatite, ilmenite and baddeleyite. Such veining is to be expected at the transition from the porous to a channelized flow regime, which may roughly coincide with the asthenosphere–lithosphere boundary (McKenzie, 1985; Foley, 1988, 1992). Continued lithospheric extension further moved the asthenosphere–lithosphere boundary upwards and outwards (indicated as steps 1–2–3 in Fig. 21a), so that a newly adjusted geotherm (from geotherm 1 to 2 in Fig. 21b) allowed remelting of the vein assemblage. These potassic silicate–carbonate vein melts infiltrated the garnet peridotite wall-rock, which caused its extensive volatile-fluxed melting and resulted in a hybrid carbonate-rich UML magma type (proto-aillikite). Whereas the high incompatible trace element contents and, in turn, Sr–Nd isotope compositions of aillikites are dominated by the vein melt, the high MgO and compatible trace element concentrations are controlled by melting in the surrounding peridotite.

A multi-stage veined mantle melting model for UML magma production beneath an incipiently rifted cratonic area (Fig. 21) not only accounts for the composition of aillikites, but also explains the relatively large magma volumes (compared with kimberlite clusters; see Tappe *et al.*, 2004) and the long time span of continuous UML magmatism in the Aillik Bay area (~35 Myr) and elsewhere along the borders of the Labrador Sea (Heaman, 2005; Tappe *et al.*, 2005*b*). However, primary carbonate-rich UML magmas (proto-aillikite) seem to reach upper crustal levels only rarely, although they may be abundant early components of extension-related continental magmatism.

ACKNOWLEDGMENTS

We are indebted to Dejan Prelevic, Bruce Ryan, Mike Villeneuve and Zoran Jovanovic for helpful discussions that ensued during this study. Randy Edmunds, Lori Dyson and Mike Bishop are thanked for logistical support in the wilderness of Labrador; and Ralf Tappert and Michelle Goryniuk for their hospitality in Edmonton. Stacey Hagen, Judy Schultz and Kendra Siemens ably assisted the geochronology work. Burkhard Schulz-Dobrick is thanked for keeping the electron microprobe facility in Mainz in excellent running condition. Thoughtful comments by Lotte Larsen, Roger Mitchell, Teal Riley, Sally Gibson and Marjorie Wilson on this manuscript are gratefully acknowledged. This project is funded by the German Research Foundation (DFG grant Fo181/15) and NSERC operating grants to G.A.J. and L.M.H. This publication is Geological Survey of Canada Contribution 2005682.

SUPPLEMENTARY DATA

Supplementary data for this paper are available at *Journal of Petrology* online.

REFERENCES

Al-Aasm, I. S., Taylor, B. E. & South, B. (1990). Stable isotope analysis of multiple carbonate samples using selective acid extraction. *Chemical Geology* **80**, 119–125.

Alibert, C. & Albarède, F. (1988). Relationships between mineralogical, chemical, and isotopic properties of some North American kimberlites. *Journal of Geophysical Research* **93**, 7643–7671.

Amundsen, H. E. F. (1987). Evidence for liquid immiscibility in the upper mantle. *Nature* **327**, 692–695.

Andersen, D. J., Lindsley, D. H. & Davidson, P. M. (1993). QUILF: a Pascal program to assess equilibria among Fe–Mg–Mn–Ti oxides, pyroxenes, olivine, and quartz. *Computers and Geosciences* **19**, 1333–1350.

Andersen, T. (1988). Evolution of peralkaline calcite carbonatite magma in the Fen Complex, Southeast Norway. *Lithos* **22**, 99–112.

Andersen, T. & Austrheim, H. (1991). Temperature–HF fugacity trends during crystallization of calcite carbonatite magma in the Fen Complex, Norway. *Mineralogical Magazine* **55**, 81–94.

Andronikov, A. V. & Foley, S. F. (2001). Trace element and Nd–Sr isotopic composition of ultramafic lamprophyres from the East Antarctic Beaver Lake area. *Chemical Geology* **175**, 291–305.

Arima, M. & Edgar, A. D. (1981). Substitution mechanisms and solubility of titanium in phlogopites from rocks of probable mantle origin. *Contributions to Mineralogy and Petrology* **77**, 288–295.

Bailey, D. K. (1984). Kimberlite: 'the mantle sample' formed by ultrametasomatism. In: Kornprobst, J. (ed.) *Kimberlites: Kimberlites and Related Rocks*. Amsterdam: Elsevier, pp. 323–333.

Ballhaus, C., Berry, R. F. & Green, D. H. (1990). Oxygen fugacity controls in the Earth's upper mantle. *Nature* **348**, 437–440.

Ballhaus, C., Berry, R. F. & Green, D. H. (1991). High pressure experimental calibration of the olivine–orthopyroxene–spinel oxygen geobarometer: implications for the oxidation state of the upper mantle. *Contributions to Mineralogy and Petrology* **107**, 27–40.

Beard, A. D., Downes, H., Vetrin, V. R., Kempton, P. D. & Maluski, H. (1996). Petrogenesis of Devonian lamprophyre and carbonatite minor intrusions, Kandalaksha Gulf (Kola Peninsula, Russia). *Lithos* **39**, 93–119.

Biellmann, C., Guyot, F., Gillet, P. & Reynard, B. (1993). High-pressure stability of carbonates: quenching of calcite-II, high-pressure polymorph of $CaCO_3$. *European Journal of Mineralogy* **5**, 503–510.

Birkett, T. C., McCandless, T. E. & Hood, C. T. (2004). Petrology of the Renard igneous bodies: host rocks for diamond in the northern Otish Mountains region, Quebec. *Lithos* **76**, 475–490.

Bizimis, M., Salters, V. J. M. & Dawson, J. B. (2003). The brevity of carbonatite sources in the mantle: evidence from Hf isotopes. *Contributions to Mineralogy and Petrology* **145**, 281–300.

Bizzarro, M. & Stevenson, R. (2003). Major element composition of the lithospheric mantle under the North Atlantic craton: evidence from peridotite xenoliths of the Sarfartoq area, southwestern Greenland. *Contributions to Mineralogy and Petrology* **146**, 223–240.

Blundy, J. & Dalton, J. A. (2000). Experimental comparison of trace element partitioning between clinopyroxene and melt in carbonate and silicate systems, and implications for mantle metasomatism. *Contributions to Mineralogy and Petrology* **139**, 356–371.

Bond, G. C., Nickeson, P. A. & Kominz, M. A. (1984). Breakup of a supercontinent between 625 Ma and 555 Ma: new evidence and implications for continental histories. *Earth and Planetary Science Letters* **70**, 325–345.

Brey, G. P., Brice, W. R., Ellis, D. J., Green, D. H., Harris, K. L. & Ryabchikov, I. D. (1983). Pyroxene–carbonate reactions in the upper mantle. *Earth and Planetary Science Letters* **62**, 63–74.

Brooker, R. A. (1998). The effect of CO_2 saturation on immiscibility between silicate and carbonate liquids: an experimental study. *Journal of Petrology* **39**, 1905–1915.

Brueckner, H. K. & Rex, D. C. (1980). K–Ar and Rb–Sr geochronology and Sr isotopic study of the Alnö alkaline complex, northeastern Sweden. *Lithos* **13**, 111–119.

Carmichael, I. S. E. (1991). The redox states of basic and silicic magmas: a reflection of their source regions? *Contributions to Mineralogy and Petrology* **106**, 129–141.

Cawood, P. A., McCausland, P. J. A. & Dunning, G. R. (2001). Opening Iapetus: constraints from the Laurentian margin in Newfoundland. *Geological Society of America Bulletin* **113**, 443–453.

Chacko, T., Mayeda, T. K., Clayton, R. N. & Goldsmith, J. R. (1991). Oxygen and carbon isotope fractionations between CO_2 and calcite. *Geochimica et Cosmochimica Acta* **55**, 2867–2882.

Chalmers, J. A. & Laursen, K. H. (1995). Labrador Sea: the extent of continental and oceanic crust and the timing of the onset of sea-floor spreading. *Marine and Petroleum Geology* **12**, 205–217.

Chalmers, J. A. & Pulvertaft, T. C. R. (2001). Development of the continental margins of the Labrador Sea: a review. In: Wilson, R. C. L., Whitmarsh, R. B., Taylor, B. & Froitzheim, N. (eds) *Non-volcanic Rifting of Continental Margins: a Comparison of Evidence from Land and Sea. Geological Society, London, Special Publications* **187**, 77–105.

Chalot-Prat, F. & Arnold, M. (1999). Immiscibility between calciocarbonatitic and silicate melts and related wall rock reactions in the upper mantle: a natural case study from Romanian mantle xenoliths. *Lithos* **46**, 627–659.

Chian, D., Louden, K. E., Keen, C. E. & Reid, I. (1995). Evolution of nonvolcanic rifted margins: new results from the conjugate margins of the Labrador Sea. *Geology* **23**, 589–592.

Clarke, L. B., Le Bas, M. J. & Spiro, B. (1994). Rare earth, trace element and stable isotope fractionation of carbonatites at Kruidfontein, Transvaal, South Africa. In: Meyer, H. O. A. & Leonardos, O. H. (eds) *Kimberlites, Related Rocks and Mantle Xenoliths*. Rio de Janeiro: Companhia de Pesquisa de Recursos Minerais, pp. 236–251.

Collerson, K. D., McCulloch, M. T. & Nutman, A. P. (1989). Sr and Nd isotope systematics of polymetamorphic Archean gneisses from southern West Greenland and northern Labrador. *Canadian Journal of Earth Sciences* **26**, 446–466.

Connelly, J. N., van Gool, J. A. M. & Mengel, F. C. (2000). Temporal evolution of a deeply eroded orogen: the Nagssugtoqidian Orogen, West Greenland. *Canadian Journal of Earth Sciences* **37**, 1121–1142.

Culshaw, N. G., Ketchum, J. & Barr, S. (2000*a*). Structural evolution of the Makkovik Province, Labrador, Canada: tectonic processes during 200 Myr at a Paleoproterozoic active margin. *Tectonics* **19**, 961–977.

Culshaw, N. G., Brown, T., Reynolds, P. H. & Ketchum, J. W. F. (2000*b*). Kanairiktok shear zone: the boundary between the Paleoproterozoic Makkovik Province and the Archean Nain Province, Labrador, Canada. *Canadian Journal of Earth Sciences* **37**, 1245–1257.

Dahlgren, S. (1994). Late Proterozoic and Carboniferous ultramafic magmatism of carbonatitic affinity in Southern Norway. *Lithos* **31**, 141–154.

Dalton, J. A. & Presnall, D. C. (1998). The continuum of primary carbonatitic–kimberlitic melt compositions in equilibrium with lherzolite: data from the system $CaO–MgO–Al_2O_3–SiO_2–CO_2$ at 6 GPa. *Journal of Petrology* **39**, 1953–1964.

Dalton, J. A. & Wood, B. J. (1995). The stability of carbonate under upper-mantle conditions as a function of temperature and oxygen fugacity. *European Journal of Mineralogy* **7**, 883–891.

Dawson, J. B. (1971). Advances in kimberlite geology. *Earth-Science Reviews* **7**, 187–214.

Dawson, J. B. & Smith, J. V. (1977). The MARID (mica–amphibole–rutile–ilmenite–diopside) suite of xenoliths in kimberlite. *Geochimica et Cosmochimica Acta* **41**, 309–323.

Deines, P. (1989). Stable isotope variations in carbonatites. In: Bell, K. (ed.) *Carbonatites: Genesis and Evolution*. London: Unwin Hyman, pp. 301–359.

Deines, P. (2002). The carbon isotope geochemistry of mantle xenoliths. *Earth-Science Reviews* **58**, 247–278.

Deines, P. (2004). Carbon isotope effects in carbonate systems. *Geochimica et Cosmochimica Acta* **68**, 2659–2679.

Digonnet, S., Goulet, N., Bourne, J., Stevenson, R. & Archibald, D. (2000). Petrology of the Abloviak aillikite dykes, New Québec: evidence for a Cambrian diamondiferous alkaline province in northeastern North America. *Canadian Journal of Earth Sciences* **37**, 517–533.

Doig, R. (1970). An alkaline rock province linking Europe and North America. *Canadian Journal of Earth Sciences* **7**, 22–28.

Doig, R. & Barton, J. M., Jr (1968). Ages of carbonatites and other alkaline rocks in Quebec. *Canadian Journal of Earth Sciences* **5**, 1401–1407.

Fedortchouk, Y. & Canil, D. (2004). Intensive variables in kimberlite magmas, Lac de Gras, Canada and implications for diamond survival. *Journal of Petrology* **45**, 1725–1745.

Ferguson, J. & Currie, K. L. (1971). Evidence of liquid immiscibility in alkaline ultrabasic dikes at Callander Bay, Ontario. *Journal of Petrology* **12**, 561–585.

Foley, S. F. (1982). Mineralogy, geochemistry, petrogenesis and structural relationships of the Aillik Bay alkaline intrusive suite, Labrador, Canada. M.Sc. thesis, Memorial University of Newfoundland, St. John's, 210 pp.

Foley, S. F. (1984). Liquid immiscibility and melt segregation in alkaline lamprophyres from Labrador. *Lithos* **17**, 127–137.

Foley, S. F. (1988). The genesis of continental basic alkaline magmas: an interpretation in terms of redox melting. *Journal of Petrology, Special Lithosphere Issue*, 139–161.

Foley, S. F. (1989*a*). Emplacement features of lamprophyre and carbonatitic lamprophyre dykes at Aillik Bay, Labrador. *Geological Magazine* **126**, 29–42.

Foley, S. F. (1989*b*). Experimental constraints on phlogopite chemistry in lamproites: 1. The effect of water activity and oxygen fugacity. *European Journal of Mineralogy* **1**, 411–426.

Foley, S. F. (1991). High-pressure stability of the fluor- and hydroxy-endmembers of pargasite and K-richterite. *Geochimica et Cosmochimica Acta* **55**, 2689–2694.

Foley, S. F. (1992). Vein-plus-wall-rock melting mechanism in the lithosphere and the origin of potassic alkaline magmas. *Lithos* **28**, 435–453.

Foley, S. F. & Jenner, G. A. (2004). Trace element partitioning in lamproitic magmas—the Gaussberg olivine leucitite. *Lithos* **75**, 19–38.

Foley, S. F., Taylor, W. R. & Green, D. H. (1986). The role of fluorine and oxygen fugacity in the genesis of the ultrapotassic rocks. *Contributions to Mineralogy and Petrology* **94**, 183–192.

Foley, S. F., Jackson, S. E., Fryer, B. J., Greenough, J. D. & Jenner, G. A. (1996). Trace element partition coefficients for clinopyroxene and phlogopite in an alkaline lamprophyre from Newfoundland by LAM-ICP-MS. *Geochimica et Cosmochimica Acta* **60**, 629–638.

Foley, S. F., Musselwhite, D. S. & van der Laan, S. R. (1999). Melt compositions from ultramafic vein assemblages in the lithospheric mantle: a comparison of cratonic and non-cratonic settings. In: Gurney, J. J., Gurney, J. L., Pascoe, M. D. & Richardson, S. H. (eds) *Proceedings of the 7th International Kimberlite Conference*. Cape Town: Red Roof Design, pp. 238–246.

Foley, S. F., Andronikov, A. V. & Melzer, S. (2002). Petrology of ultramafic lamprophyres from the Beaver Lake area of Eastern Antarctica and their relation to the breakup of Gondwanaland. *Mineralogy and Petrology* **74**, 361–384.

Forbes, W. C. & Flower, M. F. J. (1974). Phase relations of titan-phlogopite $K_2Mg_4TiAl_2Si_6O_{20}(OH)_2$: a refractory phase in the upper mantle? *Earth and Planetary Science Letters* **22**, 60–66.

Fraser, K. J., Hawkesworth, C. J., Erlank, A. J., Mitchell, R. H. & Scott-Smith, B. H. (1985). Sr, Nd and Pb isotope and minor element geochemistry of lamproites and kimberlites. *Earth and Planetary Science Letters* **76**, 57–70.

Freestone, I. C. & Hamilton, D. L. (1980). The role of liquid immiscibility in the genesis of carbonatites: an experimental study. *Contributions to Mineralogy and Petrology* **73**, 105–117.

Frey, F. A., Green, D. H. & Roy, S. D. (1978). Integrated models of basalt petrogenesis: a study of quartz tholeiites to olivine melilitites from south eastern Australia utilizing geochemical and experimental petrological data. *Journal of Petrology* **19**, 463–513.

Frost, B. R. (1991). Introduction to oxygen fugacity and its petrologic importance. In: Lindsley, D. H. (ed.) *Oxide Minerals: Petrologic and Magnetic Significance. Mineralogical Society of America, Reviews in Mineralogy* **25**, 1–9.

Frost, D. J. & Wood, B. J. (1997). Experimental measurements of the fugacity of CO_2 and graphite/diamond stability from 35 to 77 kbar at 925 to 1650 °C. *Geochimica et Cosmochimica Acta* **61**, 1565–1574.

Giannetti, B. & Luhr, J. F. (1990). Phlogopite-clinopyroxenite nodules from high-K magmas, Roccamonfina Volcano, Italy: evidence for a low-pressure metasomatic origin. *Earth and Planetary Science Letters* **101**, 404–424.

Gittins, J. & Harmer, R. E. (1997). What is ferrocarbonatite? a revised classification. *Journal of African Earth Sciences* **25**, 159–168.

Gittins, J., Macintyre, R. M. & York, D. (1967). The ages of carbonatite complexes in eastern Canada. *Canadian Journal of Earth Sciences* **4**, 651–655.

Gittins, J., Hewins, R. H. & Laurin, A. F. (1975). Kimberlitic–carbonatitic dikes of the Saguenay River valley, Quebec, Canada. *Physics and Chemistry of the Earth* **9**, 137–148.

Gower, C. F., Erdmer, P. & Wardle, R. J. (1986). The Double Mer Formation and the Lake Melville rift system, eastern Labrador. *Canadian Journal of Earth Sciences* **23**, 359–368.

Green, D. H. & Falloon, T. J. (1998). Pyrolite: a Ringwood concept and its current expression. In: Jackson, I. (ed.) *The Earth's Mantle*. Cambridge: Cambridge University Press, pp. 311–378.

Greenough, J. D. (1988). Minor phases in the Earth's mantle: evidence from trace- and minor-element patterns in primitive alkaline magmas. *Chemical Geology* **69**, 177–192.

Grégoire, M., Bell, D. R. & Le Roex, A. P. (2002). Trace element geochemistry of phlogopite-rich mafic mantle xenoliths: their classification and their relationship to phlogopite-bearing peridotites and kimberlites revisited. *Contributions to Mineralogy and Petrology* **142**, 603–625.

Grégoire, M., Bell, D. R. & Le Roex, A. P. (2003). Garnet lherzolites from the Kaapvaal Craton (South Africa): trace element evidence for a metasomatic history. *Journal of Petrology* **44**, 629–657.

Griffin, W. L. & Taylor, P. N. (1975). The Fen damkjernite: petrology of a 'central-complex kimberlite'. *Physics and Chemistry of the Earth* **9**, 163–177.

Griffin, W. L., O'Reilly, S. Y., Doyle, B. J., Pearson, N. J., Coopersmith, H., Kivi, K., Malkovets, V. G. & Pokhilenko, N. P. (2004). Lithosphere mapping beneath the North American plate. *Lithos* **77**, 873–922.

Gudfinnsson, G. H. & Presnall, D. C. (2005). Continuous gradations among primary carbonatitic, kimberlitic, melilititic, basaltic, picritic, and komatiitic melts in equilibrium with garnet lherzolite at 3–8 GPa. *Journal of Petrology* **46**, 1645–1659.

Guo, J. & Green, T. H. (1990). Experimental study of barium partitioning between phlogopite and silicate liquid at upper-mantle pressure and temperature. *Lithos* **24**, 83–95.

Hall, J., Wardle, R. J., Gower, C. F., Kerr, A., Coflin, K., Keen, C. E. & Carroll, P. (1995). Proterozoic orogens of the northeastern Canadian Shield: new information from the Lithoprobe ECSOOT crustal reflection seismic survey. *Canadian Journal of Earth Sciences* **32**, 1119–1131.

Hamilton, D. L., Bedson, P. & Esson, J. (1989). The behaviour of trace elements in the evolution of carbonatites. In: Bell, K. (ed.) *Carbonatites: Genesis and Evolution*. London: Unwin Hyman, pp. 405–427.

Hamilton, R. (1992). Geology and structural setting of ultramafic lamprophyres from Bulljah Pool, central Western Australia. *Journal of the Royal Society of Western Australia* **75**, 51–56.

Hammarstrom, J. M. & Zen, E.-A. (1986). Aluminum in hornblende: an empirical igneous geobarometer. *American Mineralogist* **71**, 1297–1313.

Hansen, K. (1980). Lamprophyres and carbonatitic lamprophyres related to rifting in the Labrador Sea. *Lithos* **13**, 145–152.

Harmer, R. E. & Gittins, J. (1997). The origin of dolomitic carbonatites: field and experimental constraints. *Journal of African Earth Sciences* **25**, 5–28.

Hawkins, D. W. (1977). Emplacement, petrology and geochemistry of ultrabasic to basic intrusives at Aillik Bay, Labrador. M.Sc. thesis, Memorial University of Newfoundland, St. John's, Canada, 236 pp.

Heaman, L. M. (1989). The nature of the subcontinental mantle from Sr–Nd–Pb isotopic studies on kimberlitic perovskite. *Earth and Planetary Science Letters* **92**, 323–334.

Heaman, L. M. (2005). Patterns of kimberlite emplacement: the importance of robust geochronology. *Report–Geological Survey of Denmark and Greenland* **68**, 25.

Heaman, L. M. & Kjarsgaard, B. A. (2000). Timing of eastern North American kimberlite magmatism: continental extension of the Great Meteor hotspot track? *Earth and Planetary Science Letters* **178**, 253–268.

Heaman, L. M. & LeCheminant, A. N. (2001). Anomalous U–Pb systematics in mantle-derived baddeleyite xenocrysts from Ile Bizard: evidence for high temperature radon diffusion? *Chemical Geology* **172**, 77–93.

Heaman, L. M., Kjarsgaard, B. A. & Creaser, R. A. (2004). The temporal evolution of North American kimberlites. *Lithos* **76**, 377–397.

Herzberg, C. & O'Hara, M. J. (2002). Plume-associated ultramafic magmas of Phanerozoic age. *Journal of Petrology* **43**, 1857–1883.

Ionov, D. A. (1998). Trace element composition of mantle-derived carbonates and coexisting phases in peridotite xenoliths from alkali basalts. *Journal of Petrology* **39**, 1931–1941.

Ionov, D. A. & Hofmann, A. W. (1995). Nb–Ta-rich mantle amphiboles and micas: implications for subduction-related metasomatic trace element fractionations. *Earth and Planetary Science Letters* **131**, 341–356.

Janse, A. J. A. & Sheahan, P. A. (1995). Catalogue of world wide diamond and kimberlite occurrences: a selective and annotative approach. *Journal of Geochemical Exploration* **53**, 73–111.

Jones, J. H., Walker, D., Pickett, D. A., Murrell, M. T. & Beattie, P. (1995). Experimental investigations of the partitioning of Nb, Mo, Ba, Ce, Pb, Ra, Th, Pa, and U between immiscible carbonate and silicate liquids. *Geochimica et Cosmochimica Acta* **59**, 1307–1320.

Kamo, S. L., Gower, C. F. & Krogh, T. E. (1989). Birthdate for the Iapetus Ocean? A precise U–Pb zircon and baddeleyite age for the Long Range dikes, Southeast Labrador. *Geology* **17**, 602–605.

Kamo, S. L., Krogh, T. E. & Kumarapeli, P. S. (1995). Age of the Grenville dyke swarm, Ontario–Quebec: implications for the timing of Iapetan rifting. *Canadian Journal of Earth Sciences* **32**, 273–280.

Keen, C. E., Courtney, R. C., Dehler, S. A. & Williamson, M. C. (1994). Decompression melting at rifted margins: comparison of model predictions with the distribution of igneous rocks on the eastern Canadian margin. *Earth and Planetary Science Letters* **121**, 403–416.

Keller, J. & Hoefs, J. (1995). Stable isotope characteristics of recent natrocarbonatite from Oldoinyo Lengai. In: Bell, K. & Keller, J. (eds) *Carbonatite Volcanism: Oldoinyo Lengai and the Petrogenesis of Natrocarbonatites*. Berlin: Springer, pp. 113–123.

Kennedy, C. S. & Kennedy, G. C. (1976). The equilibrium boundary between graphite and diamond. *Journal of Geophysical Research* **81**, 2467–2470.

Kerr, A. & Fryer, B. J. (1993). Nd isotope evidence for crust–mantle interaction in the generation of A-type granitoid suites in Labrador, Canada. *Chemical Geology* **104**, 39–60.

Kerr, A. & Fryer, B. J. (1994). The importance of late- and post-orogenic crustal growth in the early Proterozoic: evidence from Sm–Nd isotopic studies of igneous rocks in the Makkovik Province, Canada. *Earth and Planetary Science Letters* **125**, 71–88.

Kerr, A. & Wardle, R. J. (1997). Definition of an Archean–Proterozoic crustal suture by isotopic studies of basement intersections from offshore wells in the southern Labrador Sea. *Canadian Journal of Earth Sciences* **34**, 209–214.

Kerr, A., Hall, J., Wardle, R. J., Gower, C. F. & Ryan, B. (1997). New reflections on the structure and evolution of the Makkovikian–Ketilidian Orogen in Labrador and southern Greenland. *Tectonics* **16**, 942–965.

Ketchum, J. W. F., Culshaw, N. G. & Barr, S. M. (2002). Anatomy and orogenic history of a Paleoproterozoic accretionary belt: the Makkovik Province, Labrador, Canada. *Canadian Journal of Earth Sciences* **39**, 711–730.

King, A. F. & McMillan, N. J. (1975). A Mid-Mesozoic breccia from the coast of Labrador. *Canadian Journal of Earth Sciences* **12**, 44–51.

Kjarsgaard, B. A. & Hamilton, D. L. (1989). The genesis of carbonatites by immiscibility. In: Bell, K. (ed.) *Carbonatites: Genesis and Evolution*. London Kingdom: Unwin Hyman, pp. 388–404.

Kjarsgaard, B. A., Hamilton, D. L. & Gittins, J. (1989). Carbonatite origin and diversity: discussion and reply. *Nature* **338**, 547–548.

Klemme, S. & Dalpe, C. (2003). Trace-element partitioning between apatite and carbonatite melt. *American Mineralogist* **88**, 639–646.

Klemme, S. & Meyer, H. P. (2003). Trace element partitioning between baddeleyite and carbonatite melt at high pressures and high temperatures. *Chemical Geology* **199**, 233–242.

Kogarko, L. N., Henderson, C. M. B. & Pacheco, H. (1995). Primary Ca-rich carbonatite magma and carbonate–silicate–sulphide liquid immiscibility in the upper mantle. *Contributions to Mineralogy and Petrology* **121**, 267–274.

Konzett, J. & Ulmer, P. (1999). The stability of hydrous potassic phases in lherzolite mantle: an experimental study to 9·5 GPa in simplified and natural bulk compositions. *Journal of Petrology* **40**, 629–652.

Konzett, J., Sweeney, R. J., Thompson, A. B. & Ulmer, P. (1997). Potassium amphibole stability in the upper mantle: an experimental study in a peralkaline KNCMASH system to 8·5 GPa. *Journal of Petrology* **38**, 537–568.

Kresten, P. (1980). The Alnö complex: tectonics of dyke emplacement. *Lithos* **13**, 153–158.

Kretz, R. (1982). Transfer and exchange equilibria in a portion of the pyroxene quadrilateral as deduced from natural and experimental data. *Geochimica et Cosmochimica Acta* **46**, 411–421.

Kretz, R. (1983). Symbols for rock-forming minerals. *American Mineralogist* **68**, 277–279.

Larsen, L. M. & Rex, D. C. (1992). A review of the 2500 Ma span of alkaline–ultramafic, potassic and carbonatitic magmatism in West Greenland. *Lithos* **28**, 367–402.

Larsen, L. M. & Rønsbo, J. (1993). Conditions of origin of kimberlites in West Greenland: new evidence from the Sarfartoq and Sukkertoppen regions. *Report–Geological Survey of Greenland* **159**, 115–120.

Larsen, L. M., Rex, D. C., Watt, W. S. & Guise, P. G. (1999). ^{40}Ar–^{39}Ar dating of alkali basaltic dykes along the southwest coast of Greenland: Cretaceous and Tertiary igneous activity along the eastern margin of the Labrador Sea. *Geology of Greenland Survey Bulletin* **184**, 19–29.

Leat, P. T., Riley, T. R., Storey, B. C., Kelley, S. P. & Millar, I. L. (2000). Middle Jurassic ultramafic lamprophyre dyke within the Ferrar magmatic province, Pensacola Mountains, Antarctica. *Mineralogical Magazine* **64**, 95–111.

Lee, W. J. & Wyllie, P. J. (1997*a*). Liquid immiscibility between nephelinite and carbonatite from 1·0 to 2·5 GPa compared with mantle melt compositions. *Contributions to Mineralogy and Petrology* **127**, 1–16.

Lee, W. J. & Wyllie, P. J. (1997*b*). Liquid immiscibility in the join $NaAlSiO_4$–$NaAlSi_3O_8$–$CaCO_3$ at 1 GPa: implications for crustal carbonatites. *Journal of Petrology* **38**, 1113–1135.

Lee, W. J. & Wyllie, P. J. (1998). Petrogenesis of carbonatite magmas from mantle to crust, constrained by the system CaO–(MgO + FeO*)–(Na_2O + K_2O)–(SiO_2 + Al_2O_3 + TiO_2)–CO_2. *Journal of Petrology* **39**, 495–517.

Leech, G. B., Lowdon, J. A., Stockwell, C. H. & Wanless, R. K. (1962). Age determinations and geological studies. *Reports Geological Survey of Canada* **4**, 116–117.

Le Roex, A. P. & Lanyon, R. (1998). Isotope and trace element geochemistry of Cretaceous Damaraland lamprophyres and

carbonatites, northwestern Namibia: evidence for plume–lithosphere interactions. *Journal of Petrology* **39**, 1117–1146.

Le Roex, A. P., Bell, D. R. & Davis, P. (2003). Petrogenesis of Group I kimberlites from Kimberley, South Africa: evidence from bulk-rock geochemistry. *Journal of Petrology* **44**, 2261–2286.

Ludwig, K. R. (1998). On the treatment of concordant uranium–lead ages. *Geochimica et Cosmochimica Acta* **62**, 665–676.

Malpas, J., Foley, S. F. & King, A. F. (1986). Alkaline mafic and ultramafic lamprophyres from the Aillik Bay area, Labrador. *Canadian Journal of Earth Sciences* **23**, 1902–1918.

Mattey, D. P., Taylor, W. R., Green, D. H. & Pillinger, C. T. (1990). Carbon isotopic fractionation between CO_2 vapour, silicate and carbonate melts: an experimental study to 30 kbar. *Contributions to Mineralogy and Petrology* **104**, 492–505.

McKenzie, D. (1985). The extraction of magma from the crust and mantle. *Earth and Planetary Science Letters* **74**, 81–91.

McKenzie, D. (1989). Some remarks on the movement of small melt fractions in the mantle. *Earth and Planetary Science Letters* **95**, 53–72.

McKenzie, D. & Bickle, M. J. (1988). The volume and composition of melt generated by extension of the lithosphere. *Journal of Petrology* **29**, 625–679.

McKenzie, D., Jackson, J. & Priestley, K. (2005). Thermal structure of oceanic and continental lithosphere. *Earth and Planetary Science Letters* **233**, 337–349.

Meen, J. K., Ayers, J. C. & Fregeau, E. J. (1989). A model of mantle metasomatism by carbonated alkaline melts: trace-element and isotopic compositions of mantle source regions of carbonatite and other continental igneous rocks. In: Bell, K. (ed.) *Carbonatites: Genesis and Evolution*. London: Unwin Hyman, pp. 464–499.

Meert, J. G., Torsvik, T. H., Eide, E. A. & Dahlgren, S. (1998). Tectonic significance of the Fen Province, S. Norway: constraints from geochronology and paleomagnetism. *Journal of Geology* **106**, 553–564.

Mengel, K. & Green, D. H. (1989). Stability of amphibole and phlogopite in metasomatized peridotite under water-saturated and water-undersaturated conditions. In: Ross, J. (ed.) *Kimberlites and Related Rocks*. Sydney, N.S.W.: Geological Society of Australia, pp. 571–581.

Mitchell, R. H. (1973). Composition of olivine, silica activity and oxygen fugacity in kimberlite. *Lithos* **6**, 65–81.

Mitchell, R. H. (1986). *Kimberlites: Mineralogy, Geochemistry and Petrology*. New York: Plenum, 442 pp.

Mitchell, R. H. (1995). *Kimberlites, Orangeites, and Related Rocks*. New York: Plenum, 410 pp.

Mitchell, R. H. & Bergman, S. C. (1991). *Petrology of Lamproites*. New York: Plenum, 447 pp.

Mitchell, R. H., Scott-Smith, B. H. & Larsen, L. M. (1999). Mineralogy of ultramafic dikes from the Sarfartoq, Sisimiut and Maniitsoq areas, West Greenland. In: Gurney, J. J., Gurney, J. L., Pascoe, M. D. & Richardson, S. H. (eds) *Proceedings of the 7th International Kimberlite Conference*. Cape Town: Red Roof Design, pp. 574–583.

Moine, B. N., Grégoire, M., O'Reilly, S. Y., Delpech, G., Sheppard, S. M. F., Lorand, J. P., Renac, C., Giret, A. & Cottin, J. Y. (2004). Carbonatite melt in oceanic upper mantle beneath the Kerguelen Archipelago. *Lithos* **75**, 239–252.

Moore, K. R. & Wood, B. J. (1998). The transition from carbonate to silicate melts in the $CaO–MgO–SiO_2–CO_2$ system. *Journal of Petrology* **39**, 1943–1951.

Munno, R., Rossi, G. & Tadini, C. (1980). Crystal chemistry of kimzeyite from Stromboli, Aeolian Islands, Italy. *American Mineralogist* **65**, 188–191.

Murphy, D. T., Collerson, K. D. & Kamber, B. S. (2002). Lamproites from Gaussberg, Antarctica: possible transition zone melts of Archaean subducted sediments. *Journal of Petrology* **43**, 981–1001.

Murthy, G., Gower, C. F., Tubrett, M. & Paetzold, R. (1992). Paleomagnetism of Eocambrian Long Range dykes and Double Mer Formation from Labrador, Canada. *Canadian Journal of Earth Sciences* **29**, 1224–1234.

Neal, C. R. & Davidson, J. P. (1989). An unmetasomatized source for the Malaitan alnöite (Solomon Islands): petrogenesis involving zone refining, megacryst fractionation, and assimilation of oceanic lithosphere. *Geochimica et Cosmochimica Acta* **53**, 1975–1990.

Nelson, D. R. (1989). Isotopic characteristics and petrogenesis of the lamproites and kimberlites of central West Greenland. *Lithos* **22**, 265–274.

Nicholls, J., Carmichael, I. S. E. & Stormer, J. C., Jr (1971). Silica activity and P_{total} in igneous rocks. *Contributions to Mineralogy and Petrology* **33**, 1–20.

Nimis, P. & Ulmer, P. (1998). Clinopyroxene geobarometry of magmatic rocks: Part 1: an expanded structural geobarometer for anhydrous and hydrous, basic and ultrabasic systems. *Contributions to Mineralogy and Petrology* **133**, 122–135.

Nixon, P. H., Mitchell, R. H. & Rogers, N. W. (1980). Petrogenesis of alnöitic rocks from Malaita, Solomon Islands, Melanesia. *Mineralogical Magazine* **43**, 587–596.

Nowell, G. M., Pearson, D. G., Bell, D. R., Carlson, R. W., Smith, C. B., Kempton, P. D. & Noble, S. R. (2004). Hf isotope systematics of kimberlites and their megacrysts: new constraints on their source regions. *Journal of Petrology* **45**, 1583–1612.

O'Brien, H. E., Peltonen, P. & Vartiainen, H. (2005). Kimberlites, carbonatites, and alkaline rocks. In: Lehtinen, M., Nurmi, P. A. & Rämö, O. T. (eds) *Precambrian Geology of Finland—Key to the Evolution of the Fennoscandian Shield*. Amsterdam: Elsevier, pp. 605–644.

O'Neill, H. S. C. & Wall, V. J. (1987). The olivine–orthopyroxene–spinel oxygen geobarometer, the nickel precipitation curve, and the oxygen fugacity of the Earth's upper mantle. *Journal of Petrology* **28**, 1169–1191.

Otto, J. W. & Wyllie, P. J. (1993). Relationships between silicate melts and carbonate-precipitating melts in $CaO–MgO–SiO_2–CO_2–H_2O$ at 2 kbar. *Mineralogy and Petrology* **48**, 343–365.

Pearce, N. J. G. & Leng, M. J. (1996). The origin of carbonatites and related rocks from the Igaliko dyke swarm, Gardar Province, South Greenland: field, geochemical and C–O–Sr–Nd isotope evidence. *Lithos* **39**, 21–40.

Platt, R. G. & Mitchell, R. H. (1979). The Marathon Dikes. I: Zirconium-rich titanian garnets and manganoan magnesian ulvöspinel–magnetite spinels. *American Mineralogist* **64**, 546–550.

Pollack, H. N. & Chapman, D. S. (1977). On the regional variation of heat flow, geotherms, and lithospheric thickness. *Tectonophysics* **38**, 279–296.

Prelevic, D., Foley, S. F., Romer, R. L., Cvetkovic, V. & Downes, H. (2005). Tertiary ultrapotassic volcanism in Serbia: constraints on petrogenesis and mantle source characteristics. *Journal of Petrology* **46**, 1443–1487.

Price, S. E., Russell, J. K. & Kopylova, M. G. (2000). Primitive magma from the Jericho Pipe, N.W.T., Canada: constraints on primary kimberlite melt chemistry. *Journal of Petrology* **41**, 789–808.

Puffer, J. H. (2002). A late Neoproterozoic eastern Laurentian superplume: location, size, chemical composition, and environmental impact. *American Journal of Science* **302**, 1–27.

Queen, M., Heaman, L. M., Hanes, J. A., Archibald, D. A. & Farrar, E. (1996). $^{40}Ar/^{39}Ar$ phlogopite and U–Pb perovskite dating of lamprophyre dykes from the eastern Lake Superior region: evidence

for a 1·14 Ga magmatic precursor to Midcontinent Rift volcanism. *Canadian Journal of Earth Sciences* **33**, 958–965.

Raeside, R. P. & Helmstaedt, H. (1982). The Ile Bizard Intrusion, Montreal, Quebec: kimberlite or lamprophyre? *Canadian Journal of Earth Sciences* **19**, 1996–2011.

Reischmann, T., Brügmann, G. E., Jochum, K. P. & Todt, W. A. (1995). Trace element and isotopic composition of baddeleyite. *Mineralogy and Petrology* **53**, 155–164.

Renne, P. R., Swisher, C. C., Deino, A. L., Karner, D. B., Owens, T. L. & DePaolo, D. J. (1998). Intercalibration of standards, absolute ages and uncertainties in ^{40}Ar–^{39}Ar dating. *Chemical Geology* **145**, 117–152.

Righter, K. & Carmichael, I. S. E. (1996). Phase equilibria of phlogopite lamprophyres from western Mexico: biotite–liquid equilibria and *P–T* estimates for biotite-bearing igneous rocks. *Contributions to Mineralogy and Petrology* **123**, 1–21.

Riley, T. R., Leat, P. T., Storey, B. C., Parkinson, I. J. & Millar, I. L. (2003). Ultramafic lamprophyres of the Ferrar large igneous province: evidence for a HIMU mantle component. *Lithos* **66**, 63–76.

Robert, J. L. (1976). Titanium solubility in synthetic phlogopite solid solutions. *Chemical Geology* **17**, 213–227.

Rock, N. M. S. (1986). The nature and origin of ultramafic lamprophyres: alnöites and allied rocks. *Journal of Petrology* **27**, 155–196.

Rock, N. M. S. (1991). *Lamprophyres*. Glasgow: Blackie, 285 pp.

Roddick, J. C. (1983). High precision intercalibration of ^{40}Ar–^{39}Ar standards. *Geochimica et Cosmochimica Acta* **47**, 887–898.

Rogers, N. W., Hawkesworth, C. J. & Palacz, Z. A. (1992). Phlogopite in the generation of olivine melilitites from Namaqualand, South Africa and implications for element fractionation processes in the upper mantle. *Lithos* **28**, 347–365.

Romer, R. L., Schärer, U., Wardle, R. J. & Wilton, D. H. C. (1995). U–Pb age of the Seal Lake Group, Labrador: relationship to Mesoproterozoic extension-related magmatism of Laurasia. *Canadian Journal of Earth Sciences* **32**, 1401–1410.

Santos, R. V. & Clayton, R. N. (1995). Variations of oxygen and carbon isotopes in carbonatites: a study of Brazilian alkaline complexes. *Geochimica et Cosmochimica Acta* **59**, 1339–1352.

Scaillet, S. (2000). Numerical error analysis in $^{40}Ar/^{39}Ar$ dating. *Chemical Geology* **162**, 269–298.

Scott, B. H. (1981). Kimberlite and lamproite dykes from Holsteinsborg, West Greenland. *Meddelelser om Grønland, Geoscience* **4**, 3–24.

Seifert, W., Kämpf, H. & Wasternack, J. (2000). Compositional variation in apatite, phlogopite and other accessory minerals of the ultramafic Delitzsch Complex, Germany: implication for cooling history of carbonatites. *Lithos* **53**, 81–100.

Sinclair, G. S., Barr, S. M., Culshaw, N. G. & Ketchum, J. W. F. (2002). Geochemistry and age of the Aillik Group and associated plutonic rocks, Makkovik Bay area, Labrador: implications for tectonic development of the Makkovik Province. *Canadian Journal of Earth Sciences* **39**, 731–748.

Smith, J. V., Brennesholtz, R. & Dawson, J. B. (1978). Chemistry of micas from kimberlites and xenoliths: I. Micaceous kimberlites. *Geochimica et Cosmochimica Acta* **42**, 959–972.

Spera, F. J. (1984). Carbon dioxide in petrogenesis III: role of volatiles in the ascent of alkaline magma with special reference to xenolith-bearing mafic lavas. *Contributions to Mineralogy and Petrology* **88**, 217–232.

Spera, F. J. (1987). Dynamics of translithospheric migration of metasomatic fluid and alkaline magma. In: Menzies, M. A. & Hawkesworth, C. J. (eds) *Mantle Metasomatism*. London: Academic Press, pp. 1–20.

Srivastava, S. P. & Roest, W. R. (1999). Extent of oceanic crust in the Labrador Sea. *Marine and Petroleum Geology* **16**, 65–84.

Stacey, J. S. & Kramers, J. D. (1975). Approximation of terrestrial lead isotope evolution by a two-stage model. *Earth and Planetary Science Letters* **26**, 207–221.

Stormer, J. C., Pierson, M. L. & Tacker, R. C. (1993). Variation of F and Cl X-ray intensity due to anisotropic diffusion in apatite during electron microprobe analysis. *American Mineralogist* **78**, 641–648.

Sudo, A. & Tatsumi, Y. (1990). Phlogopite and K-amphibole in the upper mantle: implication for magma genesis in subduction zones. *Geophysical Research Letters* **17**, 29–32.

Sun, S.-S. & McDonough, W. F. (1989). Chemical and isotopic systematics of ocean basalts: implications for mantle composition and processes. In: Saunders, A. D. & Norry, M. J. (eds) *Magmatism in the Ocean Basins. Geological Society, London, Special Publications* **42**, 313–345.

Sweeney, R. J. (1994). Carbonatite melt compositions in the Earth's mantle. *Earth and Planetary Science Letters* **128**, 259–270.

Sweeney, R. J., Thompson, A. B. & Ulmer, P. (1993). Phase relations of a natural MARID composition and implications for MARID genesis, lithospheric melting and mantle metasomatism. *Contributions to Mineralogy and Petrology* **115**, 225–241.

Tappe, S. (2004). Mesozoic mafic alkaline magmatism of southern Scandinavia. *Contributions to Mineralogy and Petrology* **148**, 312–334.

Tappe, S., Jenner, G. A., Foley, S. F., Heaman, L. M., Besserer, D., Kjarsgaard, B. A. & Ryan, A. B. (2004). Torngat ultramafic lamprophyres and their relation to the North Atlantic Alkaline Province. *Lithos* **76**, 491–518.

Tappe, S., Foley, S. F., Jenner, G. A. & Kjarsgaard, B. A. (2005*a*). Integrating ultramafic lamprophyres into the IUGS classification of igneous rocks: rationale and implications. *Journal of Petrology* **46**, 1893–1900.

Tappe, S., Foley, S. F., Kjarsgaard, B. A., Heaman, L. M., Jenner, G. A., Stracke, A. & Romer, R. L. (2005*b*). Ultramafic lamprophyres and carbonatites of Labrador and New Quebec: towards a genetic model for Neoproterozoic rift-related alkaline magmatism in the North Atlantic region. *Report–Geological Survey of Denmark and Greenland* **68**, 115–117.

Taylor, H. P., Frechen, J. & Degens, E. T. (1967). Oxygen and carbon isotope studies of carbonatites from the Laacher See District, west Germany and the Alnö District, Sweden. *Geochimica et Cosmochimica Acta* **31**, 407–430.

Taylor, W. R. & Green, D. H. (1988). Measurement of reduced peridotite–C–O–H solidus and implications for redox melting of the mantle. *Nature* **332**, 349–352.

Thompson, R. N. & Gibson, S. A. (1994). Magmatic expression of lithospheric thinning across continental rifts. *Tectonophysics* **233**, 41–68.

Thy, P., Stecher, O. & Korstgard, J. A. (1987). Mineral chemistry and crystallization sequences in kimberlite and lamproite dikes from the Sisimiut area, central West Greenland. *Lithos* **20**, 391–417.

Torsvik, T. H., Smethurst, M. A., Meert, J. G., Van der Voo, R., McKerrow, W. S., Brasier, M. D., Sturt, B. A. & Walderhaug, H. J. (1996). Continental break-up and collision in the Neoproterozoic and Palaeozoic: a tale of Baltica and Laurentia. *Earth-Science Reviews* **40**, 229–258.

Ulmer, P. & Sweeney, R. J. (2002). Generation and differentiation of Group II kimberlites: constraints from a high-pressure experimental study to 10 GPa. *Geochimica et Cosmochimica Acta* **66**, 2139–2153.

Upton, B. G. J., Emeleus, C. H., Heaman, L. M., Goodenough, K. M. & Finch, A. A. (2003). Magmatism of the mid-Proterozoic Gardar Province, South Greenland: chronology, petrogenesis and geological setting. *Lithos* **68**, 43–65.

van Achterbergh, E., Griffin, B. J., Ryan, C. G., O'Reilly, S. Y., Pearson, N. J., Kivi, K. & Doyle, B. J. (2004). Melt inclusions from

the deep Slave lithosphere: implications for the origin and evolution of mantle-derived carbonatite and kimberlite. *Lithos* **76**, 461–474.

Veksler, I. V., Petibon, C. M., Jenner, G. A., Dorfman, A. M. & Dingwell, D. B. (1998). Trace element partitioning in immiscible silicate–carbonate liquid systems: an initial experimental study using a centrifuge autoclave. *Journal of Petrology* **39**, 2095–2104.

Vollmer, R., Ogden, P., Schilling, J. G., Kingsley, R. H. & Waggoner, D. G. (1984). Nd and Sr isotopes in ultrapotassic volcanic rocks from the Leucite Hills, Wyoming. *Contributions to Mineralogy and Petrology* **87**, 359–368.

Vuorinen, J. H. & Skelton, A. D. L. (2004). Origin of silicate minerals in carbonatites from Alnö Island, Sweden: magmatic crystallization or wall rock assimilation? *Terra Nova* **16**, 210–215.

Wardle, R. J. & Hall, J. (2002). Proterozoic evolution of the northeastern Canadian Shield: Lithoprobe Eastern Canadian Shield Onshore–Offshore Transect (ECSOOT), introduction and summary. *Canadian Journal of Earth Sciences* **39**, 563–567.

Waters, F. G. (1987). A suggested origin of MARID xenoliths in kimberlites by high pressure crystallization of an ultrapotassic rock such as lamproite. *Contributions to Mineralogy and Petrology* **95**, 523–533.

Wendlandt, R. F. & Eggler, D. H. (1980). The origins of potassic magmas: 2. Stability of phlogopite in natural spinel lherzolite and in the system $KAlSiO_4$–MgO–SiO_2–H_2O–CO_2 at high pressures and high temperatures. *American Journal of Science* **280**, 421–458.

Wyllie, P. J. (1980). The origin of kimberlite. *Journal of Geophysical Research* **85**, 6902–6910.

Wyllie, P. J. & Tuttle, O. F. (1960). The system CaO–CO_2–H_2O and the origin of carbonatites. *Journal of Petrology* **1**, 1–46.

Zhu, C. & Sverjensky, D. A. (1992). F–Cl–OH partitioning between biotite and apatite. *Geochimica et Cosmochimica Acta* **56**, 3435–3467.

Zindler, A. & Hart, S. (1986). Chemical geodynamics. *Annual Review of Earth and Planetary Sciences* **14**, 493–571.

APPENDIX A: SAMPLE LIST FOR AILLIK BAY AREA UML AND CARBONATITES

Sample no.	Rock type	Northing*	Easting*	Location	
L2	aillikite	6122191	363469	Cape Makkovik Peninsula	Cape Makkovik
L6	aillikite	6120567	358945	Aillik Peninsula	E shore of Kaipokok Bay
L49	aillikite	6117054	357974	Aillik Peninsula	W shore of Aillik Bay
L51	aillikite	6118364	358562	Aillik Peninsula	W shore of Aillik Bay
L54	aillikite	6118210	359823	Cape Makkovik Peninsula	E shore of Aillik Bay
L60	aillikite	6122218	357310	Kranck Island	E shore of Kaipokok Bay
L61	aillikite	6131452	350216	Main Turnavik Island	northern shore
L62	aillikite	6123110	360251	Aillik Peninsula	Cape Aillik
L65	aillikite	6117091	357948	Aillik Peninsula	SW shore of Aillik Bay
L66	aillikite	6118427	358537	Aillik Peninsula	W shore of Aillik Bay
L72	aillikite	6119226	350955	Black Islands	northern island
L74	aillikite	6121921	361739	Cape Makkovik Peninsula	E shore of Aillik Bay
ST109	aillikite	6118344	359827	Cape Makkovik Peninsula	E shore of Aillik Bay
ST122	aillikite	6120567	358945	Aillik Peninsula	E shore of Kaipokok Bay
ST123	aillikite	6120662	358570	Aillik Peninsula	E shore of Kaipokok Bay
ST162	aillikite	6117091	357948	Aillik Peninsula	SW shore of Aillik Bay
ST164	aillikite	6117215	358419	Aillik Peninsula	SW shore of Aillik Bay
ST198A	aillikite	6125136	356717	Man Islands	southern island
ST220II	aillikite	6124202	349612	West Turnavik Island	western island
ST225	aillikite	6125429	350465	West Turnavik Island	main island
ST228	aillikite	6108886	362613	Ford's Peninsula	E shore of Makkovik Bay
ST250A/C	aillikite	6112669	369425	Cape Strawberry Peninsula	E shore of Makkovik Bay
ST114A	mela-aillikite	6120388	359369	Aillik Peninsula	W shore of Aillik Bay
ST147A/B	mela-aillikite	6120256	356729	Aillik Peninsula	E shore of Kaipokok Bay
ST196	mela-aillikite	6119731	351742	Black Islands	northern island
ST210	mela-aillikite	6128166	352171	Main Turnavik Island	southern shore
ST239A	mela-aillikite	6107253	360141	Perrets Point	E shore of Makkovik Bay
ST244B	mela-aillikite	6106492	362179	Ford's Peninsula	E shore of Makkovik Harbour
ST251B	mela-aillikite	6112987	369784	Cape Strawberry Peninsula	E shore of Makkovik Bay
L5	damtjernite	6128890	351810	Main Turnavik Island	southern shore

Sample no.	Rock type	Northing*	Easting*	Location	
L7	damtjernite	6119970	361818	Cape Makkovik Peninsula	E shore of Aillik Bay
L44	damtjernite	6120101	361289	Cape Makkovik Peninsula	E shore of Aillik Bay
L45	damtjernite	6121468	361879	Cape Makkovik Peninsula	NE shore of Aillik Bay
L46	damtjernite	6122645	359406	Aillik Peninsula	Cape Aillik
L47	damtjernite	6116294	358092	Aillik Peninsula	S shore of Aillik Bay
L52	damtjernite	6119008	358674	Aillik Peninsula	W shore of Aillik Bay
L56	damtjernite	6121359	359395	Aillik Peninsula	W shore of Aillik Bay
L57	damtjernite	6121214	358972	Aillik Peninsula	W shore of Aillik Bay
L63	damtjernite	6123114	360251	Aillik Peninsula	Cape Aillik
L70	damtjernite	6121802	357601	Kranck Island	E shore of Kaipokok Bay
L76	damtjernite	6122397	362423	Cape Makkovik Peninsula	Cape Makkovik
L79	damtjernite	6122398	362424	Cape Makkovik Peninsula	Cape Makkovik
ST114B	damtjernite	6120388	359369	Aillik Peninsula	W shore of Aillik Bay
ST135	damtjernite	6120375	357559	Aillik Peninsula	E shore of Kaipokok Bay
ST140A	damtjernite	6120778	362055	Cape Makkovik Peninsula	NE shore of Aillik Bay
ST142	damtjernite	6121658	361764	Cape Makkovik Peninsula	NE shore of Aillik Bay
ST144	damtjernite	6120262	356870	Aillik Peninsula	E shore of Kaipokok Bay
ST159A	damtjernite	6117108	357764	Aillik Peninsula	SW shore of Aillik Bay
ST170	damtjernite	6124277	346865	Outside Pigeon Island	northern shore
ST174	damtjernite	6123724	346480	Outside Pigeon Island	southern shore
ST179A	damtjernite	6125780	354264	Grapnel Island	eastern shore
ST188A	damtjernite	6120846	352590	Red Islands	eastern island
ST198B	damtjernite	6125136	356717	Man Islands	southern island
ST205B	damtjernite	6124654	356897	Man Islands	southern island
ST206AI	damtjernite	6124728	357065	Man Islands	southern island
ST211A/C	damtjernite	6128219	352168	Main Turnavik Island	southern shore
ST213A	damtjernite	6129995	350069	Main Turnavik Island	southern shore
ST221II	damtjernite	6125820	351664	West Turnavik Island	main island
ST224B	damtjernite	6125106	350550	West Turnavik Island	main island
ST226	damtjernite	6126097	350956	West Turnavik Island	main island
ST230	damtjernite	6109765	363477	Ford's Peninsula	E shore of Makkovik Bay
ST246A	damtjernite	6112741	362755	Cape Makkovik Peninsula	W shore of Makkovik Bay
ST251A	damtjernite	6112987	369784	Cape Strawberry Peninsula	E shore of Makkovik Bay
ST256	damtjernite	6111995	367937	Cape Strawberry Peninsula	E shore of Makkovik Bay
L1	dol carbonatite	6121232	359678	Aillik Peninsula	W shore of Aillik Bay
ST189	dol carbonatite	6120833	352650	Red Islands	eastern island
ST203	dol carbonatite	6124730	356720	Man Islands	southern island
ST126	dol–cal carbonatite	6120646	358339	Aillik Peninsula	E shore of Kaipokok Bay
ST127	dol–cal carbonatite	6120638	358289	Aillik Peninsula	E shore of Kaipokok Bay
ST193A	dol–cal carbonatite	6119467	350946	Black Islands	northern island
ST198C	dol–cal carbonatite	6125136	356717	Man Islands	southern island
ST199	dol–cal carbonatite	6125192	356513	Man Islands	southern island
ST205AII	dol–cal carbonatite	6124654	356897	Man Islands	southern island
ST216	dol–cal carbonatite	6123843	343851	Inside Pigeon Island	eastern shore
ST231A	dol–cal carbonatite	6108158	359529	Big Island	eastern shore

*UTM coordinates (Zone 21 U, NAD83).

APPENDIX B: ANALYTICAL TECHNIQUES

U–Pb perovskite geochronology

Nine ultramafic lamprophyre hand specimens were processed through standard crushing and mineral separation procedures (Wilfley table, methylene iodide, Frantz isodynamic separator) at the University of Alberta, Edmonton, following the techniques described by Heaman & Kjarsgaard (2000). Perovskite recovery was best in the 40–120 μm range. Fresh euhedral crystals devoid of inclusions were individually selected, collected as morphological fractions and dissolved as such in a mix of HF and HNO_3 (usually more than 100 grains per fraction to obtain >50 μg perovskite). Uranium and lead were isolated and concentrated from perovskite using a HBr anion exchange chromatography technique. The isotopic composition of these elements was measured on a VG354 thermal ionization mass spectrometer operating in single Faraday or analogue Daly mode.

All isotopic data reported in Table 1 were corrected for mass discrimination (+0.09%/a.m.u. Pb and +0.16%/a.m.u. U), tracer and blank contribution; uncertainties are reported at 1σ. Furthermore, the presence of initial common lead was corrected using the crustal lead evolution model of Stacey & Kramers (1975). The $^{206}Pb/^{238}U$ perovskite ages were shown to be most robust because they are least sensitive to this initial common lead correction (Heaman, 1989; Heaman & Kjarsgaard, 2000). All perovskite analyses are concordant and thus allow for the calculation of multi-fraction ages using a weighted mean approach (Ludwig, 1998).

$^{40}Ar/^{39}Ar$ mica thermochronology

The clinopyroxene–phlogopite nodule ST162I was processed for $^{40}Ar/^{39}Ar$ analysis of phlogopite plates by standard mineral separation techniques, including hand-picking of inclusion-free unaltered crystals in the size range 0·5–1 mm. The phlogopite crystals were loaded into an aluminum foil packet and arranged radially in an aluminum canister (40 mm × 19 mm), which contained the flux monitor PP-20 hornblende (Hb3gr equivalent) with an apparent age of 1072 Ma (Roddick, 1983). The canister was irradiated for 120 h in position 5c at the research reactor of McMaster University (Hamilton, Ontario) in a fast neutron flux (3×10^{16} neutrons/cm^2).

Laser $^{40}Ar/^{39}Ar$ step-heating analysis of the irradiated sample was carried out at the Geological Survey of Canada, Ottawa. The sample was loaded into a 1·5 mm diameter hole in a copper planchet and stepwise heated under vacuum using a Merchantek MIR10 10 W CO_2 laser equipped with a 2 mm × 2 mm flat-field lens. The released Ar gas was cleaned over getters for 10 min before isotope analysis using a VG3600 gas source mass spectrometer. Error calculation on individual steps follows the numerical error analysis routines outlined by Scaillet (2000), whereas error analysis on grouped data follows the algebraic methods of Renne *et al.* (1998). Neutron flux gradients were evaluated by analyzing the PP-20 flux monitors, which were interspersed among the sample packets throughout the sample canister, and by interpolating a linear fit against calculated J-factor and sample position. The error on the J-factor value reported in Table 2 is conservatively estimated at ±0.6% (2σ).

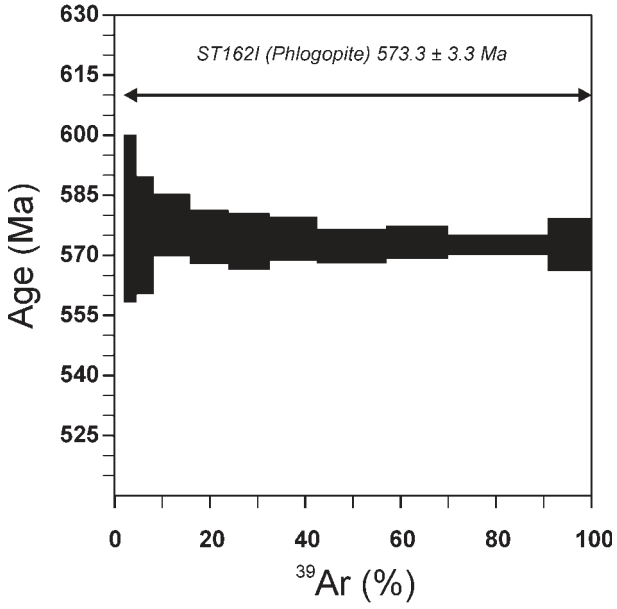

Fig. B1. Ar-release spectrum of phlogopite from clinopyroxene–phlogopite inclusion ST1621.

Blanks were measured before and after the sample analysis and levels varied in the range $^{40}Ar = (1·4–1·5) \times 10^{-6}$ nmol, $^{39}Ar = (1·2–1·4) \times 10^{-9}$ nmol, $^{38}Ar = (0·7–1·2) \times 10^{-9}$ nmol, $^{37}Ar = (0·4–0·5) \times 10^{-9}$ nmol, $^{36}Ar = (4·6–5·7) \times 10^{-9}$ nmol, all at ±20% uncertainty. Nucleogenic interference corrections are $(^{40}Ar/^{39}Ar)_K = 0·025 \pm 0·005$, $(^{38}Ar/^{39}Ar)_K = 0·011 \pm 0·010$, $(^{40}Ar/^{37}Ar)_{Ca} = 0·002 \pm 0·002$, $(^{39}Ar/^{37}Ar)_{Ca} = 0·00068 \pm 0·00004$, $(^{38}Ar/^{37}Ar)_{Ca} = 0·00003 \pm 0·00003$, $(^{36}Ar/^{37}Ar)_{Ca} = 0·00028 \pm 0·00016$. All errors are quoted at the 2σ level of uncertainty (Fig. B1).

Mineral chemistry

Mineral chemistry data were obtained using a JEOL JXA 8900 RL electron microprobe at Mainz University. Operating voltage for most silicates and carbonates was 15 kV with a beam current of 12 nA and 8 nA, respectively. Opaque oxides, perovskite, rutile, titanite and garnet were analysed with an accelerating voltage of 20 kV

and a beam current of 20 nA. The beam diameter varied between 1 and 10 μm depending on the volatile abundance in the mineral of interest. Counting time for common silicates was between 15 and 20 s on the peak, whereas trace element-rich accessories were measured for up to 50 s on the peak. International standards of natural materials were used for calibration and all data were reduced with a CITZAF procedure, except for the carbonates, for which a ZAF correction was applied.

The JEOL JXA 8900 RL electron microprobe at Göttingen University was used for high-precision halogen determination in apatite–phlogopite pairs, to calculate an equilibrium fluorine distribution. Fluorine was calibrated against a natural topaz standard under 15 kV and 15 nA operating conditions with a 10 μm beam spot. Hexagonal apatite cross-sections perpendicular to the crystallographic *c*-axis were avoided because of the variation of F and Cl X-ray intensity owing to anisotropic diffusion preferably along this crystallographic direction (Stormer *et al.*, 1993).

Whole-rock geochemistry

Major and selected trace elements were measured on fused discs by standard X-ray fluorescence (XRF) spectrometry at the University of Greifswald (Tappe, 2004). A wide range of trace elements and REE were analysed by a combination of inductively coupled plasma atomic emission spectrometry (ICP-AES) and ICP-mass spectrometry (ICP-MS) after a fusion digestion and acid dissolution procedure, respectively (Activation Laboratories, Ancaster, Canada). Concentrations for elements determined by both the ICP-MS and XRF technique are comparable within analytical error (e.g. Sr, Ce, Y, Zr, U, Th, Pb). Volatiles were measured by a combination of loss on ignition and direct determination of CO_2 using a C-S analyser.

Sr–Nd isotope composition

Sr–Nd isotope compositions were determined on the same powders as used for the major and trace element contents. We selected a Savillex beaker dissolution after tests on a variety of rock types, dissolved by both Teflon bomb and beaker technique, had confirmed that the isotope composition was identical within analytical error. The bomb dissolution was carried out in microcapsules that were placed together in an external Teflon-lined steel vessel heated in an oven at 160 °C for 7 days. Powders dissolved in Savillex beakers were attacked in a $HF–HNO_3$ mixture on a hotplate for 3 days. After slow evaporation to near dryness, the samples were taken up in 6N HCl and heated again for 1 day, repeating this step up to three times until a clear solution was obtained. Sr and Nd were separated and concentrated using Biorad AG50W cation and Eichrom Ln-Spec anion exchange resin, respectively. Sr and Nd isotope compositions were measured on a VG 54-30 Sector (Ta single filaments) and Finnigan MAT 262 (Re double filaments) thermal ionization mass spectrometer, respectively, both operating in dynamic mode (GFZ Potsdam). During the measurement period, the NBS-987 Sr reference material yielded an average value for $^{87}Sr/^{86}Sr$ of $0{\cdot}710265 \pm 12$ and the La Jolla standard yielded a $^{143}Nd/^{144}Nd$ value of $0{\cdot}511850 \pm 7$ (2σ of 11 measurements). The initial isotopic composition was calculated for an intrusion age of 582 Ma (U–Pb perovskite age of damtjernite ST140A), using the decay constants $1{\cdot}42 \times 10^{-11}$ year^{-1} and $6{\cdot}54 \times 10^{-12}$ year^{-1} for ^{87}Rb and ^{147}Sm, respectively.

Oxygen and carbon isotope composition

The oxygen and carbon isotope composition of bulk-rock carbonate fractions was measured at Göttingen University. Rock powders (<20 μm) were reacted with anhydrous H_3PO_4 under vacuum at 25 °C for ~24 h to liberate the CO_2 of the carbonates. The volume of collected CO_2 gas was close to a 100% of the theoretical yield so that no isotope fractionation during dissolution of dolomite- and calcite-bearing samples is expected to have occurred (Al-Aasm *et al.*, 1990). The purified CO_2 was analysed using a Finnigan MAT-251 gas source mass spectrometer and measured isotope ratios are expressed as $\delta^{13}C$ and $\delta^{18}O$ ‰ relative to PDB (Pee Dee Belemnite) and SMOW (Standard Mean Ocean Water), respectively. Reproducibility was better than 0·1‰ for $\delta^{13}C$ and 0·2‰ for $\delta^{18}O$ as determined by repeated measurements ($n = 5$, 2σ) of an in-house limestone standard.